THÈSE POUR OBTENIR LE GRADE DE DOCTEUR DE L'UNIVERSITÉ DE MONTPELLIER

En Physique

École doctorale Information Structure Système

Unité de recherche Laboratoire Charles Coulomb

En partenariat international avec IHPP PAS Pologne

THz Spectroscopy of Dirac matter

Présentée par Maria SZOLA
Le 23.11.2023

Sous la direction de Frédéric TEPPE
et Thomas SKOTNICKI

Devant le jury composé de

Wojciech KNAP, Prof, dr hab., IHPP PAS	Examinateur
Frédéric TEPPE, Dr., Laboratoire Charles Coulomb	Directeur
Yanko TODOROV, Dr., Ecole Normale Supérieure de Paris	Rappoteur
Tomasz STORY, Prof. dr hab., IP PAS	Rappoteur
Mario NOVAK, Dr., University of Zagreb	Rappoteur
Witold TRZECIAKOWSKI, Prof. dr. hab., IHPP PAS	Examinateur
Sébastien NANOT, Dr., Laboratoire Charles Coulomb	Examinateur

UNIVERSITÉ DE MONTPELLIER

Acknowledgements

I would like to express my greatest gratitude to my Supervisors - Dr. Frederic Teppe and Prof. Wojciech Knap. Their guidance and mentorship helped me to evolve from a student to a scientist.

It was an honor to be a part of two great teams - Laboratoire Charles Coulomb, Montpellier, France and CENTERA Laboratories, Warsaw, Poland. It was a pleasure to share my time between France and Poland, working in one of the leading research groups in my field.

I am thankful to the fellowship of the close colleagues for providing a friendly atmosphere and stimulating environment. Special thanks belong to my friends - Tristan Beranger, Benjamin Benhamou--Bui and Boris Gribakin.

My cordial gratitude belongs to the Embassy of France in Poland and Campus France, which provided me with a wonderful opportunity to pursue my doctorate in the form of a co-tutelle. Conducting research and then writing doctoral thesis in an international context gave me the opportunities impossible to obtain with a conventional doctorate. Enabling research "across boundaries", which is one of the biggest advantage for students and supervisors in the International Dual Degree PhD program.

I would also like to thank the administrative and technical support of CENTERA, L2C and LNCMI.

Additionally I am deeply grateful for my friends Kinga and Daria, who have been a consistent source of support and encouragement. Their friendship has meant the world to me, and I am incredibly appreciative for their presence in my life, especially during the difficult times.

My heartfelt thanks go to my family, especially my Mother and Grandmother for being a constant source of inspiration and support. Their steadfast belief in me and my potential has been a driving force behind my pursuit of excellence in all areas of my life.

I would like to express my deepest gratitude to my partner Jan, who has been an invaluable source of help and inspiration throughout the research and writing process of this thesis. He has been unwavering in his belief in me and has always encouraged me to pursue my dreams, no matter how challenging they may seem.

Thank you, Jan, for everything.

Abstract

This doctoral thesis focuses on the study of bulk (3D) materials with strongly non-parabolic/linear (Dirac) energy band structure and explores the validity of the relativistic models in the description of condensed matter systems. The first three chapters give the general base to the theoretical as well as experimental techniques used during the completion of the studies. The original new results are presented in the three last chapters.

The first chapter provides a comprehensive exploration of topological fundamentals in condensed matter physics, including the concept of topology and various topological classes of materials such as topological insulators, Weyl semimetals, and Dirac semimetals. It emphasizes the characterization of material topology and how it influences electronic properties, while also considering the role of crystalline symmetries in determining topological properties.

The second chapter delves into the behavior of solid-state matter in the presence of an external magnetic field, specifically focusing on optical response, optical transitions in crystalline solids, and Landau level formation. It examines how the Landau level structure affects the optical response, particularly emphasizing absorption and reflection spectra.

In the third chapter, experimental techniques employed in this study are outlined. THz spectroscopy, including magneto-transmission experiments utilizing far-infrared molecular lasers and Fourier-transform infrared spectroscopy with a Michelson interferometer are discussed.

The fourth chapter presents the results of THz magneto-optical spectroscopy analysis of $Hg_{1-x}Cd_xTe$ films under hydrostatic pressure, focusing on samples near critical values of x that undergo a topological phase transition from a semimetal to a semiconductor. Using a simplified Kane model with two free parameters, the study determines the hydrostatic deformation potentials $a_c - a_v$ at 4 K. By measuring negative and positive band gap values, the analysis reveals semi-metallic and semiconductor film behavior, respectively. The study derives the deformation potential $a_c - a_v$ at low temperatures for any x value through linear extrapolation based on values reported for CdTe, eliminating the need for band structure calculations for HgTe/HgCdTe superlattices.

The fifth chapter explores the topological phase transition in $(Cd_{1-x}Zn_x)_3As_2$, a system based on Cd_3As_2 with varying Zn content from 1 to 22%. Magneto-optics investigations demonstrate the expected behavior of a topological quantum phase transition by observing the evolution of the band gap.

The sixth chapter investigates the properties of a new combined Weyl semimetal, $Nb_{1-x}Ta_xAs$. This material exhibits characteristic features of Weyl theory and combines elements from NbAs and TaAs, which are well-known type-I Weyl semimetals. Through magneto-reflectivity and band structure analysis, the chapter confirms the discovery of this breakthrough material, $Nb_{1-x}Ta_xAs$, providing evidence for the validity of Weyl's theory and exhibiting down-dispersing lines similar to those observed in TaP.

As a result of this thesis, important progress has been obtained in the understanding of specific properties of the 3D Dirac matter. The results of chapter 4 were published in an article: M. Szoła, Y. Ivonyak, J. Przybytek, N. Mikhailov, S. Dvoretsky, F. Teppe, and W. Knap, "Hydrostatic deformation potentials of narrow-gap HgCdTe" Phys. Rev. B 106, 195202 (2022). While results of the 5 and 6 chapters are in preparation for publication, in two separate articles: M. Szoła, et al., "Towards the topological phase transition of $(Cd_{1-x}Zn_x)_3As_2$: from Dirac semimetal to trivial semiconductor" (in preparation for publication in Phys. Rev. B), M. Szoła, et al., "Tunable Weyl Cone Distribution and Unusual Down-Dispersing Lines in NbAs and $Nb_{1-x}Ta_xAs$ Investigated by Magneto-Optics" (in preparation for publication in Phys. Rev. B).

Furthermore, apart from the studies mentioned in this thesis, several other studies were conducted during the PhD program. One of these studies, titled "Terahertz cyclotron emission from two-dimensional Dirac fermions" was recently published in the journal Nature Photonics (Gebert, S., Consejo, C., Krishtopenko, S.S., Ruffenach, S., **Szoła, M.,** et al., Nat. Photon. 17, 244–249, 2023). For a comprehensive list of publications, please refer to chapter 8.

Abstract

Cette thèse doctorale se concentre sur l'étude des matériaux volumiques (3D) présentant une structure de bande d'énergie fortement non parabolique/linéaire (Dirac) et explore la validité des modèles relativistes dans la description des systèmes de la matière condensée. Les trois premiers chapitres posent les bases théoriques ainsi que les techniques expérimentales utilisées au cours de ces études. Les résultats originaux sont présentés dans les trois derniers chapitres.

Le premier chapitre propose une exploration complète des fondements topologiques en physique de la matière condensée, y compris le concept de topologie et les différentes classes topologiques de matériaux tels que les isolants topologiques, les semi-métaux de Weyl et les semi-métaux de Dirac. L'accent est mis sur la caractérisation de la topologie des matériaux et son influence sur les propriétés électroniques, tout en considérant le rôle des symétries cristallines dans la détermination des propriétés topologiques.

Le deuxième chapitre examine le comportement de la matière solide en présence d'un champ magnétique externe, en se concentrant spécifiquement sur la réponse optique, les transitions optiques dans les solides cristallins et la formation des niveaux de Landau. Il étudie comment la structure des niveaux de Landau affecte la réponse optique, en mettant particulièrement l'accent sur les spectres d'absorption et de réflexion.

Dans le troisième chapitre, les techniques expérimentales utilisées dans cette étude sont décrites. La spectroscopie THz, y compris les expériences de magnéto-transmission utilisant des lasers moléculaires infrarouges lointains et la spectroscopie infrarouge à transformée de Fourier avec un interféromètre de Michelson, y sont discutées.

Le quatrième chapitre présente les résultats de l'analyse par spectroscopie magnéto-optique THz de films de $Hg_{1-x}Cd_xTe$ sous pression hydrostatique, en se concentrant sur les échantillons proches des valeurs critiques de x qui subissent une transition de phase topologique d'un semi-métal à un semiconducteur. En utilisant un modèle simplifié de Kane avec deux paramètres libres, l'étude détermine les potentiels de déformation hydrostatique $a_c - a_v$ à 4 K. En mesurant des valeurs de bande interdite négatives et positives, l'analyse révèle respectivement un comportement de film semi-métallique et

semi-conducteur. L'étude dérive le potentiel de déformation $a_c - a_v$ à basses températures pour toute valeur de x par extrapolation linéaire basée sur les valeurs rapportées pour CdTe, éliminant ainsi la nécessité de calculer la structure de bande pour les super-réseaux HgTe/HgCdTe.

Le cinquième chapitre explore la transition de phase topologique dans $(Cd_{1-x}Zn_x)_3As_2$, un système basé sur Cd_3As_2 avec une teneur en Zn variable de 1 à 22

%. Les investigations magnéto-optiques démontrent le comportement attendu d'une transition quantique topologique en observant l'évolution de la bande interdite.

Le sixième chapitre étudie les propriétés d'un nouveau semi-métal de Weyl combiné, $Nb_{1-x}Ta_xAs$. Ce matériau présente des caractéristiques spécifiques de la théorie de la physique de Weyl et combine des éléments de NbAs et TaAs, qui sont des semi-métaux de Weyl de type I bien connus. Grâce à l'analyse de la magnéto-réflectivité et de la structure de bande, le chapitre confirme la découverte de ce matériau révolutionnaire, $Nb_{1-x}Ta_xAs$, fournissant des preuves de la validité de la théorie de la physique de Weyl et présentant des lignes de dispersion vers le bas similaires à celles observées dans TaP.

En conséquence de cette thèse, d'importants progrès ont été réalisés dans la compréhension des propriétés spécifiques de la matière de Dirac en 3D. Les résultats du chapitre 4 ont été publiés dans un article : M. Szoła, Y. Ivonyak, J. Przybytek, N. Mikhailov, S. Dvoretsky, F. Teppe et W. Knap, "Potentiels de déformation hydrostatique du HgCdTe à faible bande interdite" Phys. Rev. B 106, 195202 (2022). Tandis que les résultats des chapitres 5 et 6 sont en cours de préparation pour publication dans deux articles distincts : M. Szoła, et al., "Vers la transition de phase topologique de $(Cd_{1-x}Znx)_3As_2$: du semi-métal de Dirac au semi-conducteur trivial" (en préparation pour publication dans Phys. Rev. B). M. Szoła, et al., "Distribution réglable du cône de Weyl et lignes de dispersion descendantes inhabituelles dans NbAs et $Nb_{1-x}Ta_xAs$ étudiées par magnéto-optique" (en préparation pour publication dans Phys. Rev. B).

En outre, en dehors des études mentionnées dans cette thèse, plusieurs autres études ont été menées pendant le programme de doctorat. L'une de ces études, intitulée "Terahertz cyclotron emission from two-dimensional Dirac fermions", a récemment été publiée dans la revue Nature Photonics (Gebert, S., Consejo, C., Krishtopenko, S.S., Ruffenach, S., **Szoła, M.,** et al., Nat. Photon. 17, 244-249, 2023). Pour une liste complète des publications, veuillez vous référer au chapitre 8.

Abstract

Ta praca doktorska skupia się na badaniach materiałów objętościowych (3D) o silnie nieparabolicznej/liniowej (Diracowskiej) strukturze pasmowej i eksploruje ważność modeli relatywistycznych w opisie układów skondensowanych. Pierwsze trzy rozdziały stanowią ogólną podstawę teoretyczną i techniki eksperymentalne wykorzystane podczas realizacji tych badań. Oryginalne wyniki są przedstawione w trzech ostatnich rozdziałach.

Pierwszy rozdział zawiera wszechstronne omówienie podstaw topologicznych w fizyce materii skondensowanej, w tym koncepcji topologii oraz różnych klas materiałów topologicznych, takich jak izolatory topologiczne, półmetale Weyla i półmetale Diraca. Podkreśla się charakterystykę topologii materiałów i jej wpływ na właściwości elektroniczne, uwzględniając jednocześnie rolę symetrii krystalicznych w ustalaniu właściwości topologicznych.

Drugi rozdział zagłębia się w zachowanie materii ciała stałego w obecności zewnętrznego pola magnetycznego, skupiając się szczególnie na odpowiedzi optycznej, przejściach optycznych w ciałach stałych o strukturze krystalicznej i tworzeniu poziomów Landaua. Rozważa się, w jaki sposób struktura poziomów Landaua wpływa na odpowiedź optyczną, szczególnie akcentując widma absorpcji i odbicia.

W trzecim rozdziale przedstawiono techniki eksperymentalne stosowane w tej pracy. Omówiono spektroskopię THz, w tym eksperymenty magneto-transmisyjne z wykorzystaniem laserów molekularnych dla dalekiej podczerwieni i spektroskopię FTIR z interferometrem Michelsona.

Czwarty rozdział prezentuje wyniki analizy spektroskopii magneto-optycznej w zakresie THz dla warstw $Hg_{1-x}Cd_xTe$ poddanych ciśnieniu hydrostatycznemu, skupiając się na próbkach o wartościach krytycznych x, które przechodzą fazowe przejście topologiczne z półmetalu w półprzewodnik. Z wykorzystaniem uproszczonego modelu Kane'a z dwoma wolnymi parametrami, badanie określa potencjały deformacji hydrostatycznej $a_c - a_v$ w temperaturze 4 K. Poprzez pomiar ujemnych i dodatnich wartości przerw pasmowych, analiza ujawnia zachowanie warstw półmetali i półprzewodnika. Badanie wyznacza potencjał deformacji $a_c - a_v$ w niskich temperaturach dla dowolnej wartości x poprzez ekstrapolację liniową na podstawie wartości zgłaszanych dla CdTe, eliminując potrzebę obliczeń struktury pasmowej dla supersieci HgTe/HgCdTe.

Piąty rozdział bada fazowe przejście topologiczne w $(Cd_{1-x}Zn_x)_3As_2$, systemie opartym na Cd_3As_2 o zmiennej zawartości Zn - od 1 do 22%. Badania magneto-optyczne ilustrują oczekiwane zachowanie przejścia topologicznego poprzez obserwację ewolucji przerwy energetycznej.

Szósty rozdział bada właściwości nowego półmetalu Weyla, $Nb_{1-x}Ta_xAs$. Materiał ten wykazuje charakterystyczne cechy teorii Weyla i łączy elementy z NbAs i TaAs, które są dobrze znane jako półmetale Weyla typu I. Poprzez analizę magneto-odbicia i struktury pasmowej, rozdział potwierdza odkrycie tego przełomowego materiału, $Nb_{1-x}Ta_xAs$, dostarczając dowodów na ważność teorii Weyla i wykazując na dół biegnące linie dyspersyjne podobne do tych obserwowanych w TaP.

W wyniku tej pracy doktorskiej uzyskano ważne postępy w zrozumieniu konkretnych właściwości materiału Diraca 3D. Wyniki rozdziału 4 zostały opublikowane w artykule: M. Szoła, et al., "Hydrostatic deformation potentials of narrow-gap HgCdTe" Phys. Rev. B 106, 195202 (2022). Wyniki rozdziałów 5 i 6 są obecnie przygotowywane do publikacji w dwóch oddzielnych artykułach: M. Szoła, et al., "Towards the topological phase transition of $(Cd_{1-x}Znx)_3As_2$: from Dirac semimetal to trivial semiconductor" (przygotowanie do publikacji w Phys. Rev. B), M. Szoła, et al., "Tunable Weyl Cone Distribution and Unusual Down-Dispersing Lines in NbAs and $Nb_{1-x}Ta_xAs$ Investigated by Magneto-Optics" (przygotowanie do publikacji w Phys. Rev. B).

Ponadto, poza badaniami wymienionymi w tej pracy doktorskiej, w ramach programu doktorskiego przeprowadzono kilka innych badań. Jedno z tych badań, zatytułowane "Terahertz cyclotron emission from two-dimensional Dirac fermions", zostało niedawno opublikowane w czasopiśmie Nature Photonics (Gebert, S., Consejo, C., Krishtopenko, S.S., Ruffenach, S., **Szoła, M.,** et al., Nat. Photon. 17, 244–249, 2023). Pełną listę publikacji można znaleźć w rozdziale 8.

Contents

List of Figures xiii

List of Abbreviations xix

1 Introduction 1

1.1 Topology . . . 1

1.1.1 Topology fundamentals for quantum materials . . . 3

1.1.2 Berry phase . . . 5

1.2 Topology in condensed matter systems . . . 7

1.3 Topological quantum materials : the emergence of topologically non-trivial states of matter . . . 12

1.3.1 Crystalline symmetries and their influence on topological classes of matter . . . 12

1.4 Summary . . . 20

2 Solid state matter in external magnetic field 21

2.1 Optical response . . . 21

2.2 Optical transitions in solids . . . 24

2.3 Landau level formation . . . 27

2.4 Dirac model with massive electrons . . . 29

2.5 Kane model . . . 32

2.6 Summary . . . 34

3 Experimental techniques 35

3.1 THz Spectroscopy . . . 36

3.1.1 Introduction . . . 36

3.1.2 THz sources . . . 37

3.2 Magneto-transmission . . . 37

3.2.1 Experimental setup . . . 38

3.3 Fourier-transform infrared spectroscopy (FTIR) . . . 45

3.3.1 Experimental setup . . . 46

3.4 Summary . . . 49

4 Topological phase transition of $Hg_{1-x}Cd_xTe$ driven by hydrostatic pressure probed by THz magneto-spectroscopy **51**
4.1 Introduction . . . 51
4.2 Influence of the substrate . . . 55
4.2.1 Samples - $Hg_{1-x}Cd_xTe$ epitaxial layers . . . 55
4.3 Experimental results . . . 56
4.4 Landau-level transitions . . . 59
4.5 Discussion . . . 63
4.6 Summary . . . 67

5 Towards the topological phase transition of $(Cd_{1-x}Zn_x)_3As_2$: from Dirac semimetal to trivial semiconductor **69**
5.1 Introduction . . . 69
5.2 (Cd_3As_2) doped with Zn . . . 73
5.3 Sample preparation description . . . 75
5.4 Results . . . 76
5.4.1 Magneto-reflectivity . . . 76
5.5 Summary . . . 84

6 Magneto-reflectivity of Weyl semimetal $Nb_{1-x}Ta_xAs$ **85**
6.1 Introduction . . . 85
6.2 Transition-metal monopnictides as examples of Weyl type-I semimetals . . . 87
6.3 Modelling the band structure in the vicinity of Weyl 1 cones . . . 90
6.4 Sample description . . . 94
6.5 Experimental details and results . . . 94
6.6 Modelled response of magneto-reflectivity . . . 95
6.7 Summary . . . 97

7 Conclusion **99**
7.1 Topological phase transition of $Hg_{1-x}Cd_xTe$ . . . 99
7.2 Towards the topological phase transition of $(Cd_{1-x}Zn_x)_3As_2$ . . . 100
7.3 Weyl semimetal $Nb_{1-x}Ta_xAs$ . . . 101

8 **103**

9 Annex **105**
9.1 Detailed information about $Hg_{1-x}Cd_xTe$ samples . . . 106

References **109**

List of Figures

1.1 Illustration of trivial loop and Mobius strip. Adapted from [10], with the permission of publisher. 4
1.2 Evolution of $\vec{\lambda}$. 6
1.3 Torus representing Brillouin zone. Adapted from: [19]. 8
1.4 On the left: 3D Dirac cone with spin degenerated bands. On the right: 3D Weyl cones with lifted spin degeneracy. 14
1.5 Breaking the symmetry of a Dirac cone leads to the creation of Weyl cones. On the left: spin degenerated and parabolic energy levels of 2DEG in the presence of time-reversal and inversion symmetry. On the right: Rashba splitting after the break of the inversion symmetry via non-zero electrostatic potential perpendicular to the plane. Adapted from [28], with the permission of publisher. 14
1.6 Classification of relationship between topological classes of matter. Adapted from [30]. 17
1.7 Normally chirality is conserved, but under parallel electric and magnetic field the quantum mechanical fluctuations might break the conservation law of chirality leading to chiral anomaly. Adapted from [35], with the permission of publisher. 18

2.1 Linear energy-momentum dispersion, with interband and intraband transitions marked. Adapted from [44]. 25
2.2 Two bands separated by a band-gap. Adapted from: [54] 30
2.3 Bands separated by a band-gap of 2Δ. Adapted from: [58], with the permission of publisher. 33
2.4 Panels a-c illustrate the dependence of Landau level (LL) spacing and magnetic field on: (a) conventional massive (Schrödinger) electrons , (b) Dirac electrons in graphene , and (c) massless Kane electrons (at $k = 0$). The insets in each panel depict the energy-momentum relationships, where k_x and k_y denote momentum along the x and y axes, respectively, and the vertical axis represents energy. Adapted from [59], with the permission of publisher. 33

3.1 Sample holder and cryostat insert for the measurements at liquid helium bath. 40
3.2 Experimental setup (a) and pressure cell (b). 41
3.3 Operating CO_2 pumped FIR laser at the laboratory of THz spectroscopy (Faculty of Physics, University of Warsaw). 42
3.4 Experimental setup for Infrared Fourier Spectroscopy. 47
3.5 Layout of Michelson interferometer. 47

4.1 Crystallographic structure of HgCdTe. Adapted from: [73], with the permission of publisher. 52
4.2 The band structure tuning from CdTe to HgTe, through gapless state for $Hg_{1-x}Cd_xTe$, with $x = 0.16$. Adapted from: [58], with the permission of publisher. 53
4.3 Pictures present planar view (a) and side view (b) of the sample mounted on the holder, which was a part of a pressure cell. . . . 56
4.4 Magneto-transmission spectra of sample A measured at four different hydrostatic pressures $P_0 = 0.0$ kbar, $P_1 = 1.63$ kbar, $P_2 = 2.96$ and $P_3 = 3.83$ kbar. 57
4.5 Magneto-transmission spectra of sample B measured at two different hydrostatic pressures $P_0 = 0.0$ kbar and $P_1 = 0.6$ kbar. . 58
4.6 Magneto-transmission spectra of sample C measured at pressure $P_1 = 1.60$ kbar. 58
4.7 Landau level transitions for sample A at four hydrostatic pressures: (a) $P = 0$ kbar, (b) $P = 1.63$ kbar, (c) $P = 2.96$ kbar, (d) $P = 3.83$ kbar. Experimental data are represented by symbols. The full lines present the fits of the simplified Kane model [75] for three lines L_1 (blue), L_2 (orange) and L_3 (yellow) which correspond to $L_{1,2,\downarrow} - L_{0,n,\downarrow\uparrow}$, $L_{1,1,\uparrow} - L_{0,n,\downarrow\uparrow}$, $L_{1,1,\downarrow} - L_{0,n,\downarrow\uparrow}$ LL transitions (see Eq. (4.2)), respectively. 61
4.8 Landau level transitions for sample B at two hydrostatic pressures: (a) $P = 0$ kbar, (b) $P = 0.6$ kbar. Experimental data are represented by symbols. The full lines present the fits of the simplified Kane model [75] for line L_2, corresponding to $L_{1,1,\uparrow} - L_{0,n,\downarrow\uparrow}$, LL transitions (see Eq. (4.2)). 62
4.9 Landau level transitions for sample C at two hydrostatic pressures: (a) $P = 0$ kbar, (b) $P = 1.6$ kbar. Experimental data are represented by symbols. The full lines present the fits of the simplified Kane model [75] for two lines L_2 (orange) and L_3 (yellow) corresponding to $L_{1,1,\uparrow} - L_{0,n,\downarrow\uparrow}$, $L_{1,1,\downarrow} - L_{0,n,\downarrow\uparrow}$ LL transitions (see Eq. (4.2)), respectively. 62

4.10 Band-gap evolution as a function of pressure. Results of all of the studied samples A, B and C. 63
4.11 Deformation potential $a_c - a_v$ at cryogenic and room temperature. The red symbols and dotted line in the figure represent the values and linear interpolation of $a_c - a_v$ at 300K, which were recalculated from the results of Latussek *et al.* [101] using the current values of $B_0(T)$ and B_0' used in this work. The black symbol corresponds to the value of $a_c - a_v$ in CdTe, which was recalculated from the low-temperature data of Dunstan *et al.* [1] (see Table 4.1). The blue open symbols show the values obtained in this work (as can be seen in Table 4.2). The blue dotted line is the linear fit of $a_c - a_v$ at 2 K. The green triangles represent the values of $a_c - a_v$ recalculated from $\partial Eg/\partial P$ provided in Refs. [93, 94, 96–100] (see Table 4.1) using Eq. (4.6) and the $B_0(T)$ used in this work. 65

5.1 (a) The crystallography structure of Cd_3As_2. (b) The unit cell structure. (c) The core-level spectroscopy results. (d) Brillouin zone with the projected surface along the (001)-direction. (e) The second derivative of ARPES measurements. (f) ARPES near the Fermi level. Adapted from [115], with the permission of publisher. 71
5.2 A diagram illustrating the electronic bands in Cd_3As_2 at the center of the Brillouin zone. The bands form two types of three-dimensional conical structures: a single cone containing Kane electrons at a higher energy scale, caused by the absence of a band gap, and two highly tilted and anisotropic 3D Dirac cones at lower energies. Adapted from [112], with the permission of publisher. 72
5.3 Relative magneto-reflectivity of two samples with different orientation - (112) and (001) - (a) and (b), respectively. The full and open points indicate the positions of observed dominant and weak cyclotron resonance modes, respectively. (c) Plots the extracted points as a function of square root of B, alongside theoretical curves for Dirac and gapless Kane model, respectively. Adapted from [117], with the permission of publisher. 73
5.4 Phase diagram of $(Cd_{1-x}Zn_x)_3As_2$. As the concentration of Zn increases, the $(Cd_{1-x}Zn_x)_3As_2$ undergoes a phase transition from a topological Dirac semimetal to a semiconductor. The background color in the diagram represents the gradual change of resistivity at 2 K as x increases. Adapted from [111]. 74

5.5 The control of carriers in $(Cd_{1-x}Zn_x)_3As_2$ by the means of Zn doping and gating. (a) Band structure of $(Cd_{1-x}Zn_x)_3As_2$. (b) Scheme of the sample with back gate made from $SrTiO_3$. (c) Resistance versus temperature dependence for various concentrations of Zn (x). (d) Electron density as a function of Zn content x, with a comparison of thin samples versus bulk crystals. (e) Mobility as a function of electron density. Adapted from [110]. 75
5.6 Results of relative magneto-reflectivity and its first derivative. . 77
5.7 Results of relative magneto-reflectivity of (112) facets. Top panel: Landau level transitions as a function of magnetic field. Bottom panel: Landau level transitions as a function of $\sqrt{B}$. 78
5.8 Energy of the plasma edge splitting at $B = 0$ T and effective mass, calculated from the cyclotron energy, as a function of Zn content. Hollow points are obtained from our results, while solid points are from Akrap et. al [117]. 80
5.9 Hollow points indicate the position of cyclotron resonance for samples with different Zn concentrations. The solid lines indicate the fitted simplified Kane model for various velocity of carriers. 81
5.10 Red points are obtained from our results, while blue points are from literature for Cd_3As_2 and Zn_3As_2 [117, 122, 124]. Blue line connect the highest values from literature of the Zn_3As_2 band-gap value [124], the green line represent the lowest value of Zn_3As_2 band-gap value [122]. 83

6.1 (a) Type I Weyl semimetal. (b) Type II Weyl semimetal. The gray surface presents the position of Fermi level. Adapted from: [132], with the permission of publisher. 87
6.2 Non-centrosymmetric crystal structure. Adapted from: [24], with the permission of publisher. 88
6.3 Brillouin zone with examples of pairs of Weyl points. Adapted from: [139]. 89
6.4 (a) Intersections of ellipse and circle are places where the Weyl cones are created. (b) Electronic band structure. Adapted from: [141], with the permission of publisher. 91
6.5 Left panel presents false color plot of relative magneto-reflectivity of S1 facet 1 and right panel its first derivative. 95

6.6 (a) Magneto-reflectivity of the $Nb_{1-x}Ta_xAs$ (001) facet plotted as $\frac{R_B}{R_0}$. (b) Magneto-reflectivity of the $Nb_{1-x}Ta_xAs$ (001) facet plotted as $\frac{R_B}{R_0}$ with extraction of the observed features. (c) Simulation of the magneto-reflectivity. The blue dotted line represents the $2\sqrt{\Delta^2+\gamma_0^2}$. (d) Calculated Landau levels. 96

9.1 Information received from growers - sample 101007. 106

9.2 Information received from growers - sample 190404. 107

9.3 Information received from growers - sample 130610. 108

List of Abbreviations

2D, 3D . . . . . Two- or three-dimensional

LL . . . . . Landau level

VTI . . . . . Variable temperature insert

LHe . . . . . Liquid helium

THz . . . . . Terahertz

FIR . . . . . Far-infrared

FTIR . . . . . Fourier-transform infrared spectroscopy

DS . . . . . Dirac semimetal

WS . . . . . Weyl semimetal

TI . . . . . Topological insulator

SPT . . . . . Symmetry protected topological

IT . . . . . Intrinsic topological

TR . . . . . Time-reversal

WSM . . . . . Weyl semimetal

DSM . . . . . Dirac semimetal

NLS . . . . . Nodal-line semimetal

DNLS . . . . . Dirac Nodal-line semimetal

WNLS . . . . . Weyl Nodal-line semimetal

BZ . . . . . Brillouin zone

LLs . . . . . Landau levels

1 Introduction

Contents

1.1 **Topology** 1
1.1.1 Topology fundamentals for quantum materials 3
1.1.2 Berry phase 5
1.2 **Topology in condensed matter systems** 7
1.3 **Topological quantum materials : the emergence of topologically non-trivial states of matter** 12
1.3.1 Crystalline symmetries and their influence on topological classes of matter 12
1.4 **Summary** 20

1.1 Topology

In recent years, there has been extensive research on the topological states of matter within the fields of condensed matter physics and materials science [2]. This progress is due to a combination of factors, including successful integration of theoretical predictions, improved material processing techniques, and innovative characterization methods. Despite significant advancements, there is still much work to be done in understanding the various phases of matter.

In the quantum world, matter can exist in different phases, such as ferromagnets, spin liquids, Bose-Einstein condensates, superconductors, and more.

Solid state physics currently focuses on discovering and describing new phases and particles that occur during phase transitions in solid state materials. The behavior of these particles can be governed by the laws analogous to the special relativity, as seen with Dirac electrons [3].

In condensed matter physics, topology provides a powerful tool for understanding the underlying behavior of the electronic and other physical properties of materials. Furthermore, it can be used to describe the arrangement of atoms and molecules in a material alongside their interaction with each other. Considering these interactions in terms of topological properties, allows one to gain new insights into the properties of materials, for example, their electrical conductivity, optical and magnetic behavior.

As an example, topology can be used to describe the wavefunction of electrons and more precisely the phase in the lattices. Especially the whole concept of topological insulators has been used to explain the unusual electrical conductivity at the edges of some materials. In such cases, electrons move freely along the surface while they are confined in the bulk, giving rise to unique electrical and optical properties.

Topological concepts are not only directly applicable in condensed matter physics, but they can also be used in other areas of physics, such as materials science and quantum field theory. One example of the application of topological concepts is the study of topological quantum field theories (TQFTs), which describe the topological phases of matter. TQFTs are crucial in understanding the behavior of exotic states of matter, including topological insulators and topological superconductors. Another example is the use of topology to design and control the behavior of photonic materials, which are materials engineered to manipulate and control light. By creating photonic materials that possess topological properties, researchers can develop new optical devices and circuits that are robust against disorder and defects. These examples illustrate how topological concepts can allow researchers to understand and control the behavior of materials in ways that would not be possible otherwise [2, 4].

In summary, topology plays a vital role in comprehending and creating new materials and technologies in solid state physics. Its potential is enormous and can lead to the development of innovative materials and technologies with diverse applications, such as information storage and processing, energy generation, and communication [5, 6].

1.1.1 Topology fundamentals for quantum materials

Topology itself studies the possibility of objects to transform into each other in a continuous manner [7, 8]. These objects classification is independent of their representation in space. One of the most famous examples is a cup and a donut (in the language of mathematics a torus). Because both of those object consist of only one hole, in the world of topology they're in the same topological class. This example is widely used to explain that the form of the object and its symmetries don't matter anymore. What remains is the intrinsic property which seems to be the number of holes in it. As long as the hole remains, the object is topologically equivalent. The hole is therefore called the topological invariant of the object.

To clarify, this property stems from a broader characteristic of the object known as the total curvature. This refers to the sum of all curvatures present within the object. The total curvature is then linked to the number of holes through the Gauss-Bonnet theorem [9]:

$$\int_0^{l(\gamma)} k_g ds = 2\pi - \int_{\mathrm{int}(\gamma)} KsA_\sigma. \tag{1.1}$$

There $\gamma(s)$ is a simple closed curve laying on a surface σ with length $l(\gamma)$ and with positively-oriented γ. Additionally k_g is the geodesic curvature of γ, K is the Gaussian curvature of σ, s is the length element and dA_σ is the area element of σ.

Let us consider a Mobius strip created by twisting one end of a ribbon by 180° before gluing the two ends together. If we compare the topology of this strip to a trivial loop we can easily notice that in order to follow the whole Mobius strip

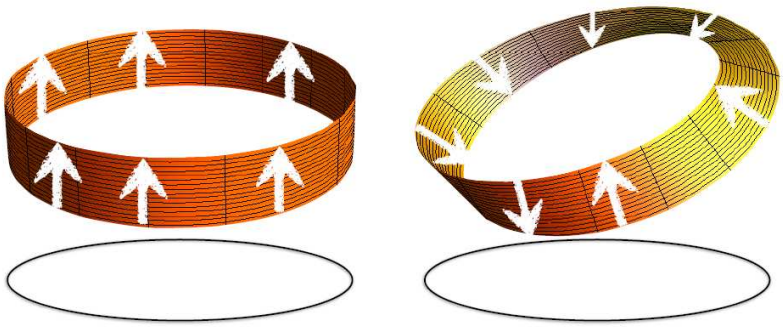


Figure 1.1: Illustration of trivial loop and Mobius strip. Adapted from [10], with the permission of publisher.

one has to create a double loop around it, while following the trivial loop one makes only one turn before arriving at the same spot, like presented in fig.1.1.

One of the interesting properties of objects in topology is the angular mismatch of parallel transport, which can be illustrated using well-known objects like the Mobius strip or traveling on the surface of the Earth.

We will now examine the concept of angular mismatch, which is used in modern geometry to define the local curvature of a surface after traversing an infinitesimal closed loop. The curvature is obtained by dividing the angular mismatch by the area of the loop. When we apply this concept to quantum mechanics, we must consider a Hamiltonian $H(\Phi, \theta)$ that depends on two angular parameters, which can be thought of as the spherical coordinates on the surface of the Earth. Assuming that the Hamiltonian has a non-degenerate ground state at zero energy, let us proceed, where the $e^{i\alpha}|\psi(\Phi, \theta)\rangle$ is the ground state.

The concept of geometric phase in quantum mechanics is closely related to the angular mismatch between the initial and final states of a quantum system during parallel transport. When a system is transported in a closed loop, its phase may shift due to parallel transport, resulting in what is known as the dynamical phase, which depends on time. However, in certain conditions, if

we consider an adiabatic motion (use of adiabatic theorem), parallel transport may cause an additional phase shift known as the geometric phase, which depends only on the path itself and doesn't depend on time. This geometric phase is known as Berry phase [11, 12].

1.1.2 Berry phase

The Berry phase is a gauge-independent geometric phase that arises when a system's wavefunction changes as a parameter the wavefunction is dependent on (denoted by ϕ) is varied along a closed path. Even though the energy spectrum of the system remains unchanged, the wavefunction ($|\psi(\phi)\rangle$) accumulates a phase that depends on the topology of the path. This phase is a physical observable [10].

Let us now introduce Berry phase mathematically [13]. Suppose we examine a closed loop within the parameter space. The adiabatic theorem states that the time-dependent Schrödinger equation can be used to evolve the ground state, as long as the parameters are varied slowly. Hamiltonian is changing slowly (adiabatic theorem) with time through the time dependence of the parameter $\vec{\lambda}(t)$ in λ space: $\vec{\lambda}(0) = \vec{\lambda}(T)$ (fig. 1.2), with Schrödinger equation [14]:

$$i\hbar\partial t\,|\psi(t)\rangle = \widehat{H}[\vec{\lambda}(t)]\,|\psi(t)\rangle\,. \tag{1.2}$$

Now let us see what happens with the wavefunction: $|\psi(0)\rangle \to |\psi(T)\rangle = ?$. $|\psi(t)\rangle$ remains proportional to the ground state, as the total number of particles is unchanged the only thing we can have here is phase:

$$|\psi(t)\rangle = e^{i\varphi(t)}\,|0,t\rangle\,. \tag{1.3}$$

Which is only true when we consider the adiabatic theorem, with slow deformation of the Hamiltonian [15].

The only unknown part is $\psi(t)$.

$$i\hbar\partial\,|\psi(t)\rangle = E_0(t)\,|\psi(t)\rangle \tag{1.4}$$

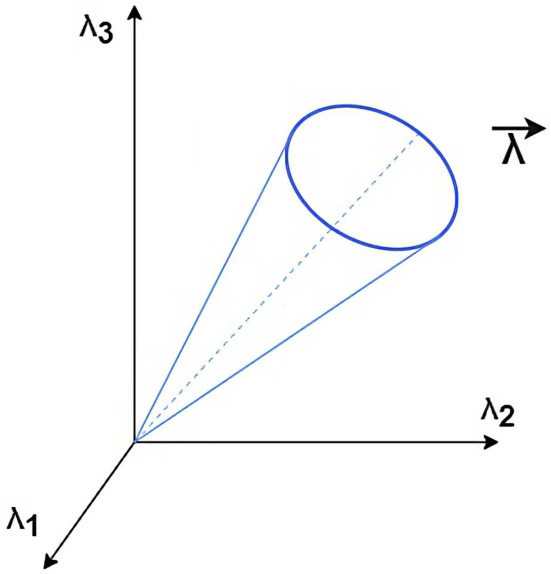


Figure 1.2: Evolution of $\overrightarrow{\lambda}$.

where $E_0(t)$ is the energy of ground state depending in t.

$$\varphi(t) = -\frac{1}{\hbar}\int_0^t E_0(t')dt' + \gamma \tag{1.5}$$

where γ is the Berry phase and $-\frac{1}{\hbar}\int_0^t E_0(t')dt'$ is the usual dynamic phase.

Now, with a new notation:

$$\gamma = \oint_C \overrightarrow{A}(\overrightarrow{\lambda})d\overrightarrow{\lambda} \tag{1.6}$$

with:

$$\overrightarrow{A}(\overrightarrow{\lambda}) = i\left\langle 0, \overrightarrow{\lambda} \middle| \frac{\partial}{\partial \overrightarrow{\lambda}} \middle| 0, \overrightarrow{\lambda} \right\rangle \tag{1.7}$$

(called Berry connection) which looks like a potential. With analogy to electromagnetism, we know that to describe magnetic field in real space we may introduce a vector potential such that the curl of this vector potential is the magnetic field with the accuracy to the gauge, with $\overrightarrow{r}$ being the position in real space :

$$\overrightarrow{B}(\overrightarrow{r}) = \nabla \times \overrightarrow{A}(\overrightarrow{r}) \tag{1.8}$$

Here, instead of a real space we have a fictitious parameter space:

$$\vec{\Omega}(\vec{\lambda}) = \nabla \times A(\vec{\lambda}). \tag{1.9}$$

From this, we find that the quantum phase acquired by the wave function during its evolution is the flux of a fictitious magnetic field, called Berry curvature:

$$\gamma = \oint_C \vec{A}(\vec{\lambda}) d\vec{\lambda} = \int\int \vec{\Omega}(\vec{\lambda}) d\vec{\lambda}. \tag{1.10}$$

In this context, the Berry phase is a measurement of the angular mismatch of the parallel transport around the closed loop.

This idea can be applied in physics and the band structure of a topological insulator can be thought of as a twisted version of a conventional insulator, in similar way as twisting of a ribbon to form a Mobius strip (fig. 1.1). The twist in the band structure creates non-trivial topology which in turn leads to the formation of protected surface states. The concept of Mobius strip here is used as an analogy to understand the topology of the band structure of topological insulators [2, 16].

1.2 Topology in condensed matter systems

Up to this point, we have discussed a general description of the concept. Now, we will examine how this concept applies to solids in reciprocal space, using the Brillouin zone (BZ) to further illustrate the point. In this context, the BZ plays the role of the surface, serving as an analogy to the surface of the Earth or the one of the Mobius strip, in the previous examples.

In the context of solids, the electron momentum serves as the natural parameter space. Any alteration to the electron wavefunction within the unit cell creates a Berry connection and curvature, as previously explained. However, it's worth noting that the electron momentum is not the sole parameter space available. The other examples include BZ in shapes dependent

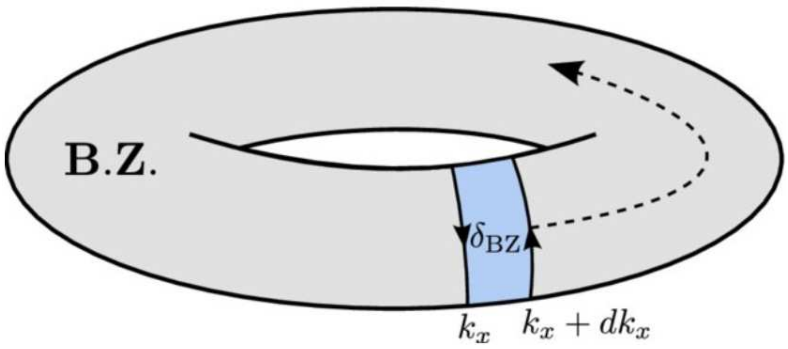


Figure 1.3: Torus representing Brillouin zone. Adapted from: [19].

on crystal symmetry and the specific natural parameter space is depending on the physical system under study and the parameters that are relevant for describing its behavior [17].

Let us now consider one of the most characteristic feature of the Berry phase - its continuous parameter space, where the state of the system travels in a closed loop. In this sense, BZ is a torus shaped parameter space which exists naturally in the band structure of solids (see fig. 1.3). In BZ the Bloch k vector is used for the description of the energy band. When considering periodic solid, k is a conserved quantity, where the Bloch function $\psi_{nk}(r)$ can be specified by the band index n and k. The $\psi_{nk}(r)$ will pick up a Berry phase when by applying the perturbation to the solid, k varies on a closed path in the Brillouin zone. If BZ is a torus, therefore when changing the k up to the edge of the zone, the path is closed when reaching the edge. This situation can be observed in a 1D solid, where the end points of the BZ are $\frac{\pi}{a}$ and $-\frac{\pi}{a}$ (where a is a lattice constant). In case when k is sweeped through the whole BZ, the Bloch function $\psi_{nk}(x)$ is corresponding to the whole energy band. In this consideration, if k varies from $\frac{\pi}{a}$ to $-\frac{\pi}{a}$, then the $\psi_{nk}(x)$ will pick up the Berry phase [18].

In the situation when in solid, the inversion symmetry is preserved, the Berry phase becomes quantized and assumes values of 0 and π. When the parity of the wavefunction at two high symmetry points is different, the Berry phase for a closed path encircling both points would be π. If the wavefunction has the same parity, then the corresponding Berry phase would be zero [20].

The parity argument allows us to explain that in a specific case parity is a good parameter to probe the topological nature of the system. It allows to give a clear example as in graphene, where parity argument shows that the product of the parity of the Bloch wave function in all the high symmetry points of the BZ is even in trivial and odd if non-trivial. There is in this case a twist of the parity that can't be removed, just like the one of the Mobius strip. Then it comes logically that there is only one way to have such twist of the parity in the BZ - to have a band inversion. That's why crystals with band inversion are of high demand - in order to search for non-trivial topological properties. And the only way to remove the twist is to close the gap.

Berry phase is linked with the band inversion through a parity argument, which is a powerful tool used in condensed matter physics to understand the relationship between the topology of the electronic band structure and the underlying symmetries of the crystal lattice. Band inversion refers to a situation in which the ordering of the energy bands in a crystal is associated with topologically non-trivial phases of matter, where the electronic properties are robust against certain types of perturbations [2, 21]. The parity argument itself establishes a link between the band inversion and the Berry phase, through the consideration of the symmetry properties of the crystal lattice. It relies on the fact that the electronic wavefunctions of a crystal can be classified in accordance to their behavior under the symmetry operations of the lattice. In particular the wavefunctions can be classified as even or odd with the respect to a particular symmetry operation.

To sum up, analogously, the relationship between the Mobius strip and a quantum system is similar. Similar to a Mobius strip that has a twist and doesn't return to its original state after a full rotation, a quantum system made up of a particular wavefunction in the Hilbert space may not go back to its initial state after its parameters complete a cycle around a closed loop in the parameter space. As the system goes through this process, the Berry phase accumulates.

When dealing with 3D solids, we are still working with the 3D torus and in certain conditions, we anticipate a non-zero value of the Berry phase for any closed path in the Brillouin zone. Due to the symmetry present in the BZ, which serves as a parameter space, the Berry phase is quantized and only takes on values that correspond to Wyckoff positions in the crystal, which tells us the positions of atoms in a crystal. Ultimately, the Berry phase can be utilized to characterize the whole bands of solids, similar to how the band center is used in the band representation of space groups.

In condense matter physics, the topology of the system is determined by the band structure and the band-gap. For two systems to be topologically equivalent or invariant, we must be able to continuously transform their Hamiltonians into each other - without closing or opening the band-gap at any given point. If this condition is preserved we can say that the topology of the system was preserved. The given condition cannot be preserved for example in a situation of a topological phase transition from a topological insulator to the ordinary semiconductor, as the band-gap may close at a critical point, causing a change in the topological properties of the system. Such topological phase transitions are a subject of intense research in condensed matter physics, and are of great interest due to their potential applications in the development of new materials with unique electronic properties [22].

For the quantum systems only the global structure has influence on its properties. In other words the results of measurements on the topologically invariant property is not affected by any impurities or defects of the material.

In this thesis, I will focus on the analysis of band inversion, band-gap closing, and related phenomena in materials. While the Berry phase is a crucial concept in the study of topological materials, I will not be exploring it in this work. Instead, I will delve into the characterization of materials with inverted band structures, such as Weyl and Dirac semimetals. I will examine the optical properties of these materials, as well as their response to external stimuli such as pressure and magnetic fields, to gain a better understanding of their

behavior. By investigating these properties, we can gain insight into the design and engineering of novel topological materials with desirable properties for practical applications.

1.3 Topological quantum materials : the emergence of topologically non-trivial states of matter

During the past decade the topologically non-trivial states of matter have been widely studied within the field of condensed matter physics. The interest first started after the discovery of topological insulators (TI) [2], which are characterized by an insulator-like bulk states, but at the same time have protected conducting states on their surface. More recently, the attention of the community shifted towards the topological semimetals - among this broad family of 'relativistic'-like materials, we distinguish Dirac and Weyl semimetals (DSM and WSM, respectively) [23–25]. These two classes of materials will play a crucial role in the development of this thesis.

1.3.1 Crystalline symmetries and their influence on topological classes of matter

Crystalline symmetries play a fundamental role in the behavior of matter and its electronic properties. In solid-state physics, the presence of crystalline symmetries is a key factor which determines the specific topological properties of materials. All of the topological materials are materials which possess special electronic properties that are robust against perturbations or disorder. Properties which arise due to the non-trivial topology of the electronic band structure of said material. Examples of crystalline symmetries like rotational symmetry, mirror symmetry, or space-inversion symmetry (I), can protect these topological properties by imposing constraints on the electronic band structure. In this sense studying the crystalline symmetries in topological materials is crucial for understanding the unique electronic properties of these materials and for predicting the existence of new topological materials.

When a crystal has time-reversal symmetry (TR), it follows that the electronic states at $\mathbf{k}$ and -$\mathbf{k}$ in reciprocal space, which have the same energy, possess opposite spins, as expressed by the equation:

$$E_{n,\uparrow}(\mathbf{k}) = E_{n,\downarrow}(-\mathbf{k}). \tag{1.11}$$

Conversely, for systems with space-inversion symmetry, the spin remains consistent at both **k** and -**k**, as demonstrated by the equation:

$$E_{n,\uparrow}(\mathbf{k}) = E_{n,\uparrow}(-\mathbf{k}). \tag{1.12}$$

Dirac semimetals are created when two doubly degenerated bands cross at a discrete point called a Dirac point. DSMs are characterized by the linear band dispersion in k and their low energy excitation can be described as a massless Dirac fermions in the close vicinity of Dirac nodes [22].

In a situation when time-reversal or inversion symmetry is broken in combination with SOC (presented in fig. 1.4), the double degenerated bands are separated into two non-degenerated conical bands. This band crossing is called Weyl nodes. Similar situation with an external stimuli can be seen when considering spin-splitting of the bands by Rashba splitting for instance (see fig. 1.5). Rashba splitting is caused by uniaxial symmetry, so it can have also 'internal' origin. Of course, external electric field induces always uniaxial symmetry. Where the inversion symmetry is broken by an external electrostatic potential $V \neq 0$ which is perpendicular to the plane and leading to Rashba splitting.

Within WSMs we can find Weyl points of opposite chirality which are separated in the momentum space. Weyl nodes which exhibit opposite chirality are separated in this crystal space and connected only through Fermi arcs, which are non-closed surface states. Importantly the Berry curvature at the Weyl points becomes singular and is a 'source' or 'sink'. We can see the Weyl nodes as 'magnetic monopoles' in k-space [6, 26, 27].

Differently than in the case of WSMs or DSMs, the touching point of Nodal-line semimetals (NLS) is rather an extension into a 1D line or ring which is propagating through the Brillouin zone. NLS can exist in a form of Dirac Nodal-line semimetal (DNLS) or Weyl Nodal-line semimetal (WNLS), depending on the symmetry protection. DNLS are occurring with both time-reversal

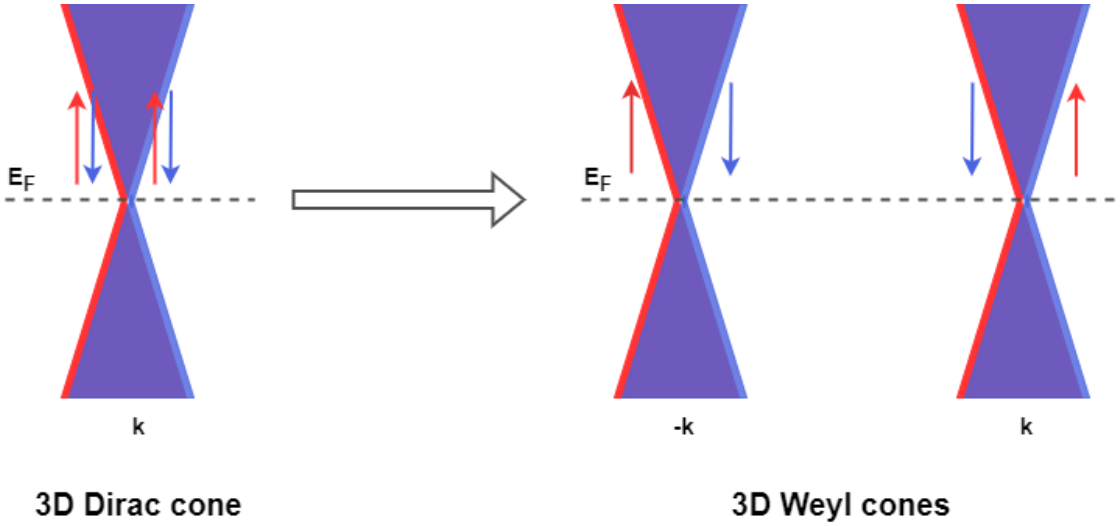


Figure 1.4: On the left: 3D Dirac cone with spin degenerated bands. On the right: 3D Weyl cones with lifted spin degeneracy.

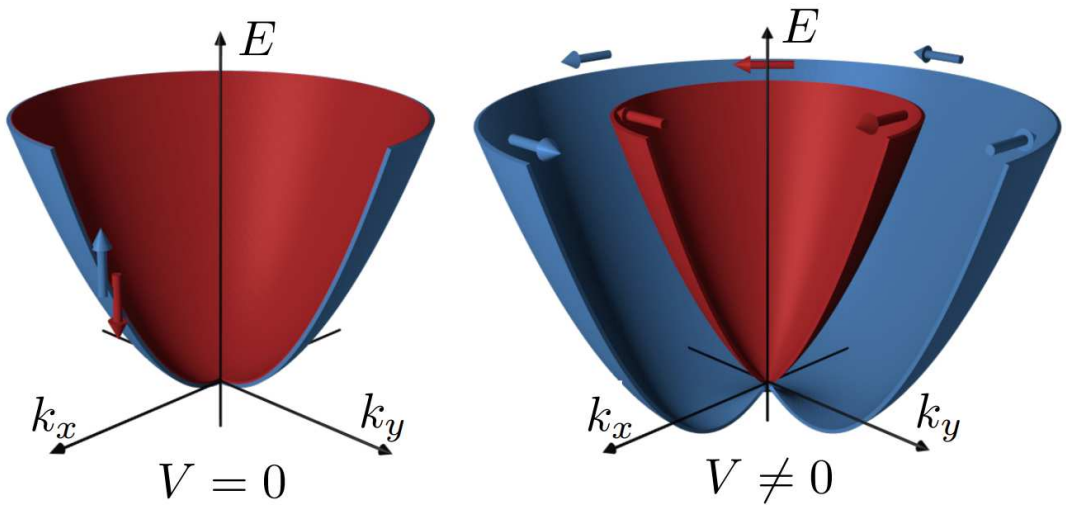


Figure 1.5: Breaking the symmetry of a Dirac cone leads to the creation of Weyl cones. On the left: spin degenerated and parabolic energy levels of 2DEG in the presence of time-reversal and inversion symmetry. On the right: Rashba splitting after the break of the inversion symmetry via non-zero electrostatic potential perpendicular to the plane. Adapted from [28], with the permission of publisher.

and inversion symmetry, while in WNLS crystals either one of the symmetry is broken, which allows for the spin splitting. This allows for the fourfold degenerated nodal-lines to split forming two singly degenerated nodal-lines.

Non-symmorphic symmetry is referring to a type of crystals symmetry, which combines a lattice translation with a non-spatial symmetry operation which would be for example - glide reflection or screw rotation. Especially in DNLS without SOC non-symmorphic symmetry is crucial because it protects the band crossing between the conduction and valence bands, forming a 1D nodal line. In a combination with time-reversal symmetry it also ensures the protection against perturbations and secure its presence in the band structure [29].

Mirror reflection symmetry is such symmetry operation where an object is reflected across a certain plane (mirror) and then appears as a mirror image of itself.

Rotational symmetry is a type of symmetry where an object is rotated around a fixed point, which is called a center of rotation, by an angle and remains unchanged. The angle of rotation which is required in order to produce the symmetry is called in this case the rotational symmetry angle.

Let us now discuss the connection between various topological classes of materials as presented in fig. 1.6. Beginning with a spinless [1] DNLS with spin orbital coupling one can obtain [30]:

1. spinfull DNLS - with occurrence of non-symmorphic, time-reversal and inversion symmetry.

[1] All electrons, as well as all fermions, possess an intrinsic property called "spin." Spin has a value of 1/2 in units of the reduced Planck constant $\hbar$ and can take on one of two values, +1/2 or -1/2. In many phenomena in condensed matter physics, such as magnetism, transport, and optical properties, the spin properties of electrons are crucial. When we refer to a material as "spinless" it means that the electrons in the material have spin, but we can ignore the spin property for simplicity. However, in reality, all electrons have spin. On the other hand, when we refer to a material as "spinful" we are emphasizing the fact that the spin properties of the electrons in the material are essential for understanding its physical properties. Therefore, the distinction between spinless and spinful materials is primarily a matter of emphasis rather than an indication that some materials have spin while others do not.

2. spinfull WNLS - with nodal-lines are protected by mirror reflection with high-symmetry plane and at the same time if either time-reversal or inversion symmetry is broken. This way the spin component of the nodal-ring is splitted and two Weyl loops are created.

3. 3D DSM - when rotation symmetry protects symmetry-invariant points. One has to note, that if either time-reversal or inversion symmetry of DSM is broken, one can also obtain WSM.

4. WSM - When the conditions are right, such as a suitable strength of spin-orbital coupling that doesn't create a gapped insulator, the presence of mirror reflection symmetry and electronic states composed of orthogonal orbital components.

5. TI - when material has both inversion and time-reversal symmetry.

Let's explore the different topological classes of materials. Spinfull Dirac nodal line semimetals (DNLS) have an electronic structure characterized by a nodal line. In these materials we consider electrons with spin, which gives them magnetic properties. In addition, they have properties similar to those of the Dirac equation in quantum field theory. These materials exhibit a large magneto-resistance effect, topologically protected surface states, and strong spin-dependent scattering, which is a process in which scattering of particles depends on their spin orientation [29].

Spinfull Weyl nodal line semimetals have a similar electronic structure to DNLS. However, instead of Dirac points, WNLS have Weyl points. In these materials we also consider electrons with spin and a nodal line that intersects the valence and conduction band. The crossing points in WNLS are of Weyl type, which means that the band structure has properties similar to those of the Weyl equation [29].

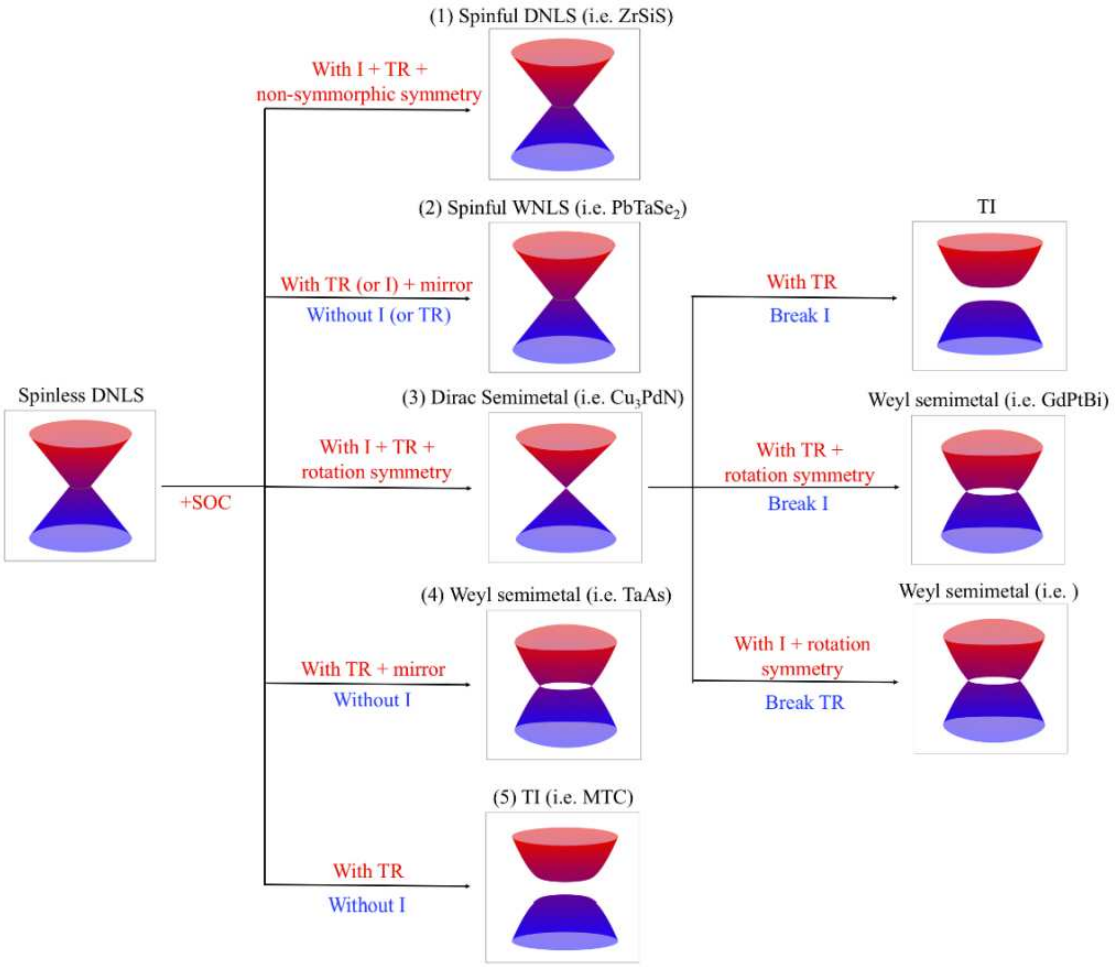


Figure 1.6: Classification of relationship between topological classes of matter. Adapted from [30].

3D Dirac semimetals (DSMs) have an electronic structure characterized by the presence of Dirac cones. These cones are special points in the energy-momentum space, where the energy levels of electrons behave like cone-shaped dispersion relations. This class of materials has a linear relationship between the energy and momentum of electrons near the Dirac point, similar to the behavior of relativistic particles described by the Dirac's equation. This results in unusual phenomena such as extremely high conductivity and large specific heat capacity [31–33].

Weyl semimetals (WSMs) are characterized by the presence of Weyl points. In WSMs, electrons near the Weyl points have a chiral charge related to the direction of their motion. Just like in DSMs, WSMs have a large number of

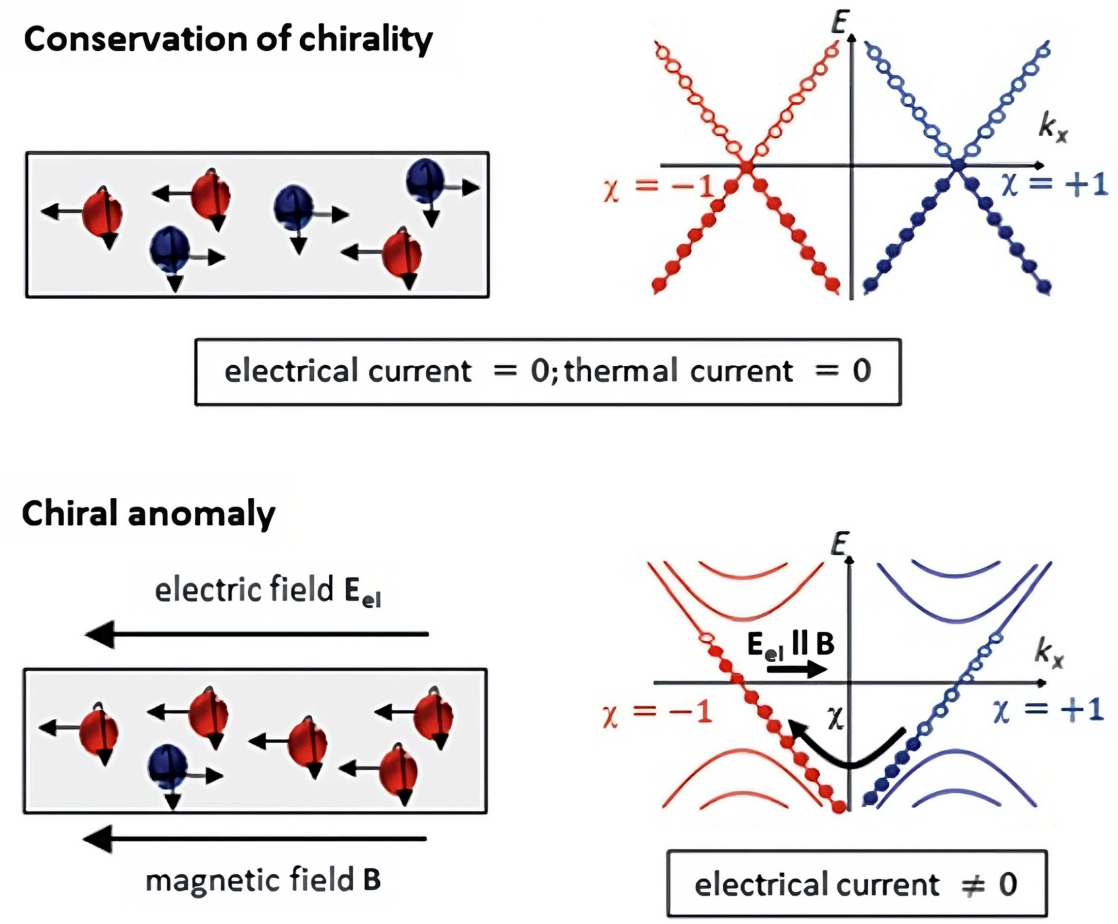


Figure 1.7: Normally chirality is conserved, but under parallel electric and magnetic field the quantum mechanical fluctuations might break the conservation law of chirality leading to chiral anomaly. Adapted from [35], with the permission of publisher.

carriers near the Weyl points, giving rise to unique magneto-electric and optical properties. Additionally, WSMs are expected to exhibit chiral anomaly (fig. 1.7 presents the conservation of chirality and chiral anomaly) [26, 34]. It should be emphasized that typically, the Weyl point has a net chirality of zero, as this is a direct consequence of the requirement for the integrated net Berry flux over the Brillouin zone to be zero [22].

Topological insulators (TIs) are characterized by insulating behavior in the material's interior and metallic behavior on the surface due to the topological nature of the electronic states near the surface. These states are protected by topological invariants and are resistant to defects or impurities. Electronic

states on the surface of a TI are topologically protected surface states and have a linear dispersion relation and large spin-orbit interaction. This leads to interesting physical phenomena such as the absence of back-scattering. The unique electronic structure of TIs makes them good candidates for use in a variety of demanding applications [2, 36–38].

1.4 Summary

This chapter provides a comprehensive introduction to topology, a mathematical field with numerous applications in condensed matter physics, and its importance in understanding the electronic properties of materials. I start by explaining the fundamental concepts of topology and their relevance in studying electronic properties that are resistant to perturbations.

In addition, I discuss the unique properties of Dirac matter, which has become an outstanding class of topological materials in recent years. Furthermore, I explore how the topological properties of Dirac matter are determined by crystalline symmetries, which can lead to different topological classes of matter and significantly impact all electronic properties of the material.

To summarize, this chapter introduces the fundamental concepts of topology and Dirac matter, and their relevance in solid-state physics.

In the upcoming chapters, I will describe specific materials that have been studied, including HgCdTe, CdZnAs, and NbTaAs. These materials possess unique topological properties that can be explored using magneto-optical experiments, providing insight into the energy levels of electrons in a magnetic field, the band structure of the material, and the properties of the electrons within them. This will be achieved by analyzing the changes in transmission and reflection of THz radiation as a function of a magnetic field.

2 Solid state matter in external magnetic field

Contents

2.1 Optical response 21
2.2 Optical transitions in solids 24
2.3 Landau level formation 27
2.4 Dirac model with massive electrons 29
2.5 Kane model 32
2.6 Summary 34

2.1 Optical response

The complex response functions are encoding the optical properties of solid state matter. One of the most widely used functions are: optical conductivity ($\sigma(\omega)$), dielectric function ($\varepsilon(\omega)$) and index of refraction ($N(\omega)$) [39, 40].

The complex index of refraction consist of real and imaginary part:

$$N = n + ik, \tag{2.1}$$

where n is a real index of refraction and k is the extinction coefficient. The real part of N in a dielectric is directly linked to the speed of light v inside

the said material, as:

$$v = \frac{c}{n}, \tag{2.2}$$

where c is the speed of light in vacuum.

In an isotropic material, the dielectric function presents itself in a form of scalar function, depending on the angular frequency ω , which is defined by a materials parameters:

$$\mathbf{D} = \varepsilon_0 \varepsilon(\omega)\mathbf{E}, \tag{2.3}$$

where $\mathbf{D}$ is the electric displacement field, ε_0 is the permittivity of the vacuum and $\mathbf{E}$ is the intensity of the electric field.

The index of the refraction is linked to the dielectric function as [41]:

$$\varepsilon(\omega) = N(\omega)^2. \tag{2.4}$$

The dielectric function also consists of real and imaginary parts, which are dependent on the frequency of the radiation:

$$\varepsilon(\omega) = \varepsilon_1(\omega) + i\varepsilon_2(\omega). \tag{2.5}$$

The real part of the dielectric function $\varepsilon_1(\omega)$ characterizes the distortion of the charge distribution of the material, by the electric field and the imaginary part, $\varepsilon_2(\omega)$, characterizes the absorption properties of the material.

In isotropic materials the optical conductivity presents as follows:

$$\mathbf{j}(\omega) = \sigma(\omega)\mathbf{E}(\omega), \tag{2.6}$$

where $\mathbf{j}$ is the induced current density.

Now let us develop the relationship between $\varepsilon(\omega)$ and $\sigma(\omega)$. From Maxwell equations we obtain:

$$\sigma(\omega) = \sigma_1(\omega) + i\sigma_2(\omega) = -i(\omega)\varepsilon_0(\varepsilon(\omega) - 1). \tag{2.7}$$

And then:

$$\sigma_1(\omega) = \omega\varepsilon_0\varepsilon_2(\omega) \text{ and } \sigma_2(\omega) = -\omega\varepsilon_0(\varepsilon_1(\omega) - 1). \tag{2.8}$$

The complex refractive index can be used to describe the dissipation of light interaction with matter:

$$N(\omega) = n(\omega) + ik(\omega). \tag{2.9}$$

The reflectivity is influenced by the complex refractive index as follows:

$$R(\omega) = \left|\frac{1-N(\omega)}{1+N(\omega)}\right| = \frac{(1-n(\omega))^2 + k(\omega)^2}{(1+n(\omega))^2 + k(\omega)^2}. \tag{2.10}$$

With then the simple formula for transmission:

$$T(\omega) = \frac{4n(\omega)}{(n(\omega)+1)^2 + k^2} = 1 - R(\omega). \tag{2.11}$$

2.2 Optical transitions in solids

The transitions between conduction and valence band are referred as interband transitions (fig.2.1) [42]. In an ideal case, without any free carriers, there is no contribution from the interband transitions to the optical conductivity below the energy of the band gap. Then for the energies of value above the band gap value an onset of absorption can be observed. This onset is called a fundamental absorption edge. Relative positions of the valence and conducting bands in the Brillouin zone has its influence on the strength of the absorption edge and in optics it represents gap and Fermi level. In materials with the direct band-gap (valence and conduction bands extrema are occupying the same position in BZ) the absorption edge is strong [43].

In a situation when valence and conduction band extrema are further from one another the materials are called indirect band materials. In the case of an indirect band gap, for an electron to be promoted to the other band, electron-phonon interaction is needed (according to momentum and energy conservation laws), which in general means that these system have much weaker absorption edge.

The contribution from intraband transitions, occurring from free carriers, can be modeled classically using Drude model [45]. This model is treating electrons with density N, as a diluted gas of particles, which is moving freely in any direction. In order to relax to equilibrium state, this system is colliding with impurities, other particles and crystal defects. The relaxation is characterized by the scattering time τ. In a situation when electric field is applied, the system is brought out of the equilibrium state, where the electric field is as follows: $E(t) = E_0 e^{-i\omega t}$. Now let us introduce the equation of motion, which describes the interaction of a single electron with the electrical component of the radiation:

$$m\frac{\partial^2 r}{dt^2} + \frac{m}{\tau}\frac{\partial r}{\partial t} = -eE(t). \tag{2.12}$$

The solution can be obtained as a complex optical conductivity:

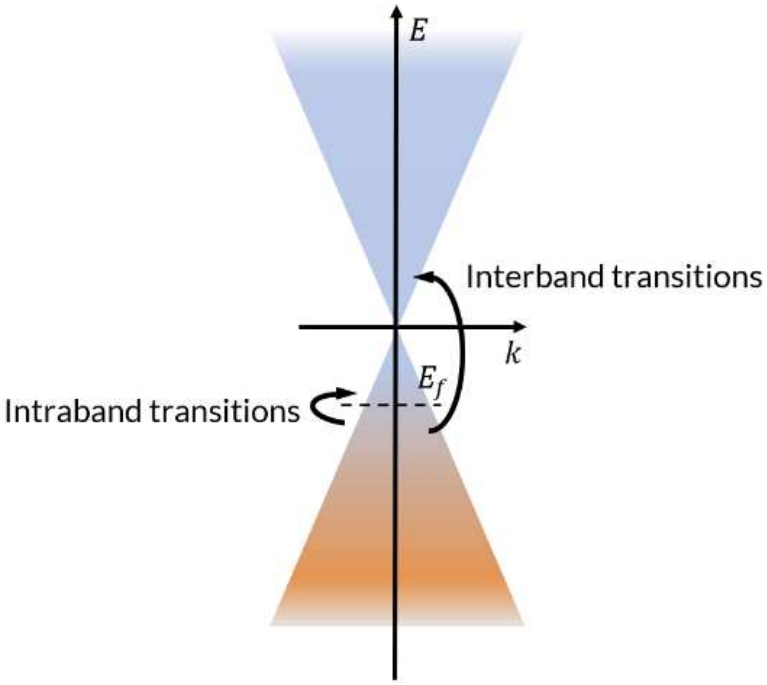


Figure 2.1: Linear energy-momentum dispersion, with interband and intraband transitions marked. Adapted from [44].

$$\sigma(\omega) = \frac{\sigma_0}{1 - i\omega\tau}, \tag{2.13}$$

where we denote σ_0 as the optical conductivity at $\omega = 0$.

An entirely quantum-mechanical approach is required for the interband excitations. In the case when electrons are promoted between two electronic states $\langle\alpha|$ and $|\beta\rangle$, the absorption of light is described by the real part of the optical conductivity as in Kubo-Greenwood formula [46]:

$$\sigma(\omega) = \frac{\pi e^2}{\omega\hbar^2} \sum_{\alpha\neq\beta} \int \frac{\partial^3 k}{(2\pi)^3} |\langle\alpha|\hat{v}_i|\beta\rangle|^2 \times \left[f(E_\alpha) - f(E_\beta)\right] \times \delta\left[\hbar\omega - (E_\beta - E_\alpha)\right]. \tag{2.14}$$

In this formula there are three most important terms, which need to be further described, they are: selection rules, joint density of states (jDOS) and Pauli blocking (occupation factor).

The velocity operator $\hat{v}_i$ describes the absorption rate of an optical transition between states $\langle\alpha|$ and $|\beta\rangle$, as the selection rules. The term $\sum_k \delta\left[\hbar\omega - (E_\beta - E_\alpha)\right]$

is the joint density of states, which marks the number of optical transitions at the frequency ω and is obtained by an integral over the relevant part of reciprocal space. Finally let us move to the Pauli blocking and the occupation factor. Where $f(E_\alpha) - f(E_\beta)$ is representing a joint occupation factor, ensuring that only transition from occupied states to non-occupied states are allowed. For the gapped system with the preservation of the electron-hole symmetry, when the Fermi energy is counted from the edge of the band, we can observe the onset of interband absorption at the energy of photon of $2(\delta + E_F)$. While in a gapless system this onset can be observed at $2E_F$, with the same electron-hole symmetry preserved.

2.3 Landau level formation

Let us begin with a situation when a 3D free electron - an electron placed inside a gas of non-interacting particles, is in a homogeneous magnetic field **B**, which is described by the vector potential **A**. Searching for the solution of the Schrödinger equation, let us find the corresponding eigenvalues and eigenstates:

$$i\hbar\frac{\partial\Psi(x,y,z,t)}{\partial t} = \hat{H}\Psi(x,y,z,t). \tag{2.15}$$

One has to only solve the time-independent Schrödinger equation, because of the assumption that the magnetic field is constant in time. Solving the time-independent equation is equivalent to looking for eigenvalues and eigenvectors of a Hamiltonian:

$$\hat{H}\psi(x,y,z) = E\psi(x,y,z), \tag{2.16}$$

here $\hat{H}$ is Hamiltonian of the particle, E energy, and $\psi(x,y,z)$ is a wavefunction depending on the x, y, z space coordinates. Now the Hamiltonian of an electron placed in magnetic field is:

$$\hat{H} = \frac{1}{2m_e}(\mathbf{p} - q\mathbf{A})^2, \tag{2.17}$$

where m_e is the mass of the electron, $\overrightarrow{p}$ is the momentum, and q is the charge of the electron. Standard Landau gauge can be used to solve the Schrödinger equation. In the Landau gauge the vector potential $\mathbf{A} = (-B_y, 0, 0)$ is corresponding to the magnetic field which is applied to along the z axis $\mathbf{B} = (0, 0, B)$. Therefore the 2.16 can be written as:

$$\frac{1}{2m_e}((p_x - eBy)^2 + p_y^2 + p_z^2)\psi(x,y,z) = E\psi(x,y,z) \tag{2.18}$$

Equation 2.18 does not depend on x and z, so it can be rewritten as:

$$\left[\frac{1}{2}m_e\frac{e^2B^2}{m_e^2}(y-\frac{p_x}{eB})^2+\frac{p_y^2}{2m_e}\right]Y(y)=\left(E-\frac{p_z^2}{2m_e}\right)Y(y), \tag{2.19}$$

since $\psi(x,y,z)=X(x)Y(y)Z(z)=e^{-i(k_xx+k_zz)}X(y)$.

Now 2.19 clearly resembles the equation which describes the 1D quantum harmonic oscillator:

$$\left[\frac{1}{2}m_e\omega^2(y-y_0)^2+\frac{p_y^2}{2m_e}\right]Y(y)=\varepsilon Y(y) \tag{2.20}$$

One can see that ω is a classical cyclotron frequency of a charged particle in magnetic field, so from this point on we will call it ω_c. In z direction the energy levels of this oscillator have parabolic dispersion, this corresponds to free motion in the direction of the magnetic field applied to the system. Nevertheless the motion which is perpendicular to B is quantized and the kinetic energy reaches only discrete, equidistantly spaced values, called Landau levels:

$$E_n=\omega_c\hbar\left(n+\frac{1}{2}\right)+\frac{k_z^2\hbar^2}{2m_e}, \tag{2.21}$$

where n is the index of a Landau level and $\omega_c=\dfrac{eB}{m_e}$.

In the end in a region, where the electronic band is relatively parabolic, the Landau level spectrum of an electron reads:

$$E_{LL,n}=\frac{eB}{m_e}\hbar\left(n+\frac{1}{2}\right)+\frac{k_z^2\hbar^2}{2m_e}. \tag{2.22}$$

Then the distribution of the Landau levels of an electron in a parabolic band is equidistant, with the adjacent levels separated by the energy, which is given by the classical cyclotron frequency ω_c.

2.4 Dirac model with massive electrons

Even though we already described the behavior of a free electron in a single parabolic band, in order to explain a response of electrons in a material, we have to propose a model with two or more bands [47].

During the study of the electronic properties of solids, the band structure is a crucial concept that helps with the understanding of the behavior of electrons in a crystal lattice. The traditional approach is based on non-relativistic quantum mechanics, that is assuming that the electrons move much slower than the speed of light. However, in certain cases, such as in the presence of high magnetic fields, the relativistic effects on the electronic structure can be significant.

The relativistic-like description of the band structure was first proposed by Keldysh in 1965 [48]. Where he introduced the concept of the Dirac equation to describe the behavior of electrons in a crystal lattice, with taking into account their relativistic motion. This approach was further developed by Zawadzki in the 1980s [49–53]. He proposed a new model based on the Dirac equation to describe the electronic structure of semiconductors.

Zawadzki's work shows that the band structure of a crystal can be understood in terms of the relativistic motion of electrons within the lattice. With this approach, the electrons are described as Dirac particles that are moving in a periodic potential which is created by the crystal lattice. One of the key features of the relativistic band structure is the existence of a Dirac cone at the center of the BZ. The Dirac cone has a point where the valence and conduction bands touch and the electrons behave as relativistic particles with zero rest mass.

Let us now present the Hamiltonian of a massive Dirac electrons, to describe a conical band with a possibly open energy band-gap of 2Δ (fig. 2.2):

$$\hat{H}_D = \begin{bmatrix} \Delta & \hbar v(q_x + iq_y) \\ \hbar v(q_x - iq_y) & -\Delta \end{bmatrix}, \tag{2.23}$$

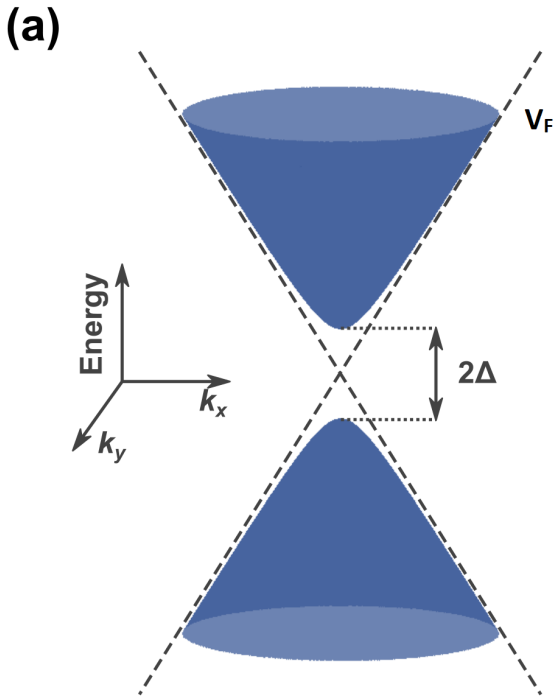


Figure 2.2: Two bands separated by a band-gap. Adapted from: [54]

where v is the asymptotic velocity. Using the Peierls substitution to obtain the LL spectrum of the Hamiltonian 2.23, with the addition of magnetic field $(0,0,B)$:

$$\hat{H}_D = \begin{bmatrix} \Delta & \hbar v(q_x - iq_y + ieBx) \\ \hbar v(q_x + iq_y - ieBx) & -\Delta \end{bmatrix}. \tag{2.24}$$

The mass of the electrons is determined by the size of the gap and so for strictly linear bands the electrons move as massless particles and with a mass of $m = \frac{E_g/2}{v^2}$ for the pseudo-parabolic bands.

As in Peierls substitution, we incorporate the periodic lattice potential into the Hamiltonian of the system as a perturbation.

Now we can obtain the energy spectrum for the valence and conduction band (negative and positive values of n, respectively):

$$E_{D,n} = \mathrm{sgn}(n)v\sqrt{2\hbar eB|n| + \Delta^2},\ n = 0, \pm 1, \pm 2, \ldots . \tag{2.25}$$

We need to remember that the selection rules determine the allowed and forbidden transitions between different electronic energy states in material. The dipole selection rule in spectroscopy is stating that the transitions between two states are only allowed between two states if there is a change in the quantum number of the electron state's energy level by one unit. This rule arises because of the electric dipole moment operator which characterizes the interaction between the electromagnetic field and the atom. The change in the dipole moment during a transition is related to the change in angular momentum, and the conservation of angular momentum gives rise to the selection rule, which determines the allowed transition.

With the assumption of conventional selection rules for the isotropic system, the electric-dipole active transitions can occur when changing the Landau level index as $\Delta n = \pm 1$.

Both interband and intraband transitions make up the optical contribution:

$$E_{D,n}^{Inter} = \sqrt{2\hbar evB|n+1| + \Delta^2} + \sqrt{2\hbar evB|n| + \Delta^2}, \tag{2.26}$$

$$E_{D,n}^{Intra} = \sqrt{2\hbar evB|n+1| + \Delta^2} - \sqrt{2\hbar evB|n| + \Delta^2}. \tag{2.27}$$

It should be noted that the selection rules are a result of the matrix elements found in the Kubo-Greenwood formula discussed in the preceding section. In an anisotropic system, non-conventional selection rules with a greater difference in the LL index can be observed.

2.5 Kane model

Kane model is used for the description of the band structure of semiconductors with a zinc-blende structure in the six-band approximation [55]. That is without taking into account the spin-split hole band. It was originally proposed by Kane in his 1957 and 1958 papers [56, 57], and it has since been extended and refined to describe a wide range of semiconductor materials. The model is constructed at Γ-point:

$$H_k = \begin{pmatrix} H_{W,\uparrow}^{\frac{1}{\sqrt{3}}} & \hbar v k_z C \\ \hbar v k_z C^\top & H_{W,\downarrow}^{\frac{1}{\sqrt{3}}} \end{pmatrix} \tag{2.28}$$

where:

$$H_{W,\uparrow}^{\frac{1}{\sqrt{3}}} = \gamma \begin{pmatrix} 0 & \sqrt{3}k_- & 0 \\ \sqrt{3}k_+ & \bar{E}_g & -k_- \\ 0 & -k_+ & 0 \end{pmatrix}, \tag{2.29}$$

$$H_{W,\downarrow}^{\frac{1}{\sqrt{3}}} = \gamma \begin{pmatrix} 0 & k_- & 0 \\ k_+ & \bar{E}_g & -\sqrt{3}k_- \\ 0 & -\sqrt{3}k_+ & 0 \end{pmatrix}, \tag{2.30}$$

$$C = \begin{pmatrix} 0 & 0 & 0 \\ -1 & 0 & 0 \\ 0 & -1 & 0 \end{pmatrix}, \tag{2.31}$$

here parameter $\gamma = \hbar v/2$. The k-dependence in the z-direction is denoted by matrix C and $\bar{E}_g = E_g/\gamma$, which is a re-normalized gap between the upper and lower cone. With the assumption that $k_z = 0$, the matrices $H_{W,\uparrow}^{\frac{1}{\sqrt{3}}}$ and $H_{W,\downarrow}^{\frac{1}{\sqrt{3}}}$ are decoupled.

At $\mathbf{k} = 0$, the heavy-hole (HH) band exhibits degeneracy with the light-hole (LH) bands (fig. 2.3). As a result, the position of the heavy-hole flat band relative to the upper or lower band depends on the sign of the gap, which can be determined from the energy dispersion:

$$E_{E,LH} = \frac{E_g}{2} \pm \sqrt{\frac{E_g^2}{4} + (\hbar v k)^2},\ E_{HH} = 0 \tag{2.32}$$

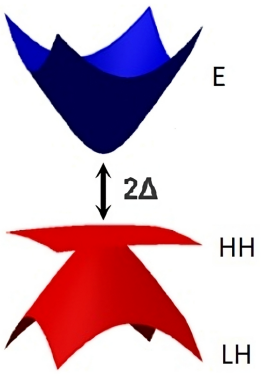


Figure 2.3: Bands separated by a band-gap of 2Δ. Adapted from: [58], with the permission of publisher.

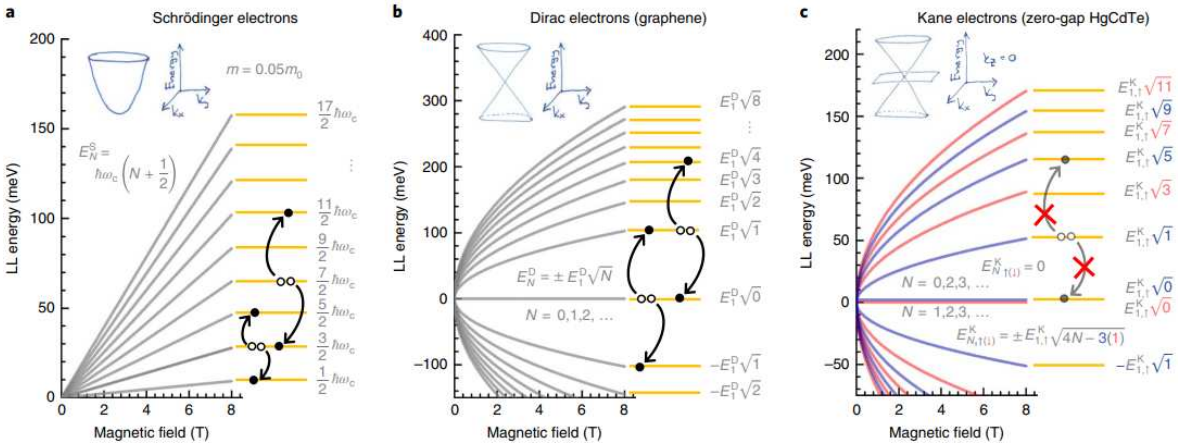


Figure 2.4: Panels a-c illustrate the dependence of Landau level (LL) spacing and magnetic field on: (a) conventional massive (Schrödinger) electrons , (b) Dirac electrons in graphene , and (c) massless Kane electrons (at $k = 0$). The insets in each panel depict the energy-momentum relationships, where k_x and k_y denote momentum along the x and y axes, respectively, and the vertical axis represents energy. Adapted from [59], with the permission of publisher.

Further visualization of the differences between Schrödinger, Dirac, and Kane electrons is presented in fig. 2.4. There panels present: (a) the Landau levels equidistantly spaced in energy, (b) the Dirac electrons in graphene and finally (c) Landau levels with Kane electrons.

2.6 Summary

This chapter discusses various aspects of optical responses and transitions in solids. This includes optical conductivity, dielectric function, index of refraction, reflectivity, and transmission. Described properties are crucial for understanding the behavior of materials in response to electromagnetic radiation, and additionally can be calculated using theoretical models.

The chapter also covers Kubo-Greenwood formula, which describes optical transitions in solids and relates the optical conductivity to the probability of electronic transitions between different states in crystalline matter. Moreover, it provides a mean of understanding the relationship between electronic structure of materials and their optical properties.

Formation of Landau levels in solids is also discussed. It arises from the quantization of electronic energy levels in magnetic field.

This chapter also considers the Dirac model with massive electrons, which is a theoretical framework used to describe the behavior of electrons in solids with relativistic type effects taken into account. In particular this model is relevant for the materials with narrow gap or even gapless and is used to explain the variety of optical and electronic properties of these materials.

Finally Kane model is introduced to describe the behavior of electrons in semiconductors with a large spin-orbit coupling and is based on the concept of a $k \cdot p$ perturbation theory. Here electrons are described by three bands, with a band-gap.

3 Experimental techniques

Contents

3.1 THz Spectroscopy 36
3.1.1 Introduction 36
3.1.2 THz sources 37
3.2 Magneto-transmission 37
3.2.1 Experimental setup 38
3.3 Fourier-transform infrared spectroscopy (FTIR) 45
3.3.1 Experimental setup 46
3.4 Summary 49

3.1 THz Spectroscopy

Optical spectroscopy is an experimental tool used to probe single particle as well as collective excitations of solids. Excitations over far-infrared region are of great interest since they can be used to examine the electronic properties of materials. At this particular energy scale, some of the possible excitations include magnons, phonons, and excitons, among others. Magnetic field have a significant impact on materials, as it can change the band structure or cause topological phase transitions. By studying the effects of magnetic field on materials using techniques such as THz magneto-spectroscopy, one can uncover new physical phenomena that help us understand previously unsolved problems in physics. One established method for measuring the effective masses of charged carriers is cyclotron resonance spectroscopy. Beyond intraband transitions (CR) one can also have access to interband transitions and beyond the effective mass, all these optical transitions allow one to reconstruct the band structure of the material, determine its gap, and probe the pecularities of certain LLs.

3.1.1 Introduction

Infrared radiation was first discovered by sir W. Herschel after his experiments regarding thermometers with blackened bulbs, that were used as radiation detectors [60]. One hundred years later Max Planck developed a well known formula representing spectral energy distribution of a black-body radiation, laying the foundation stone for quantum mechanics. It can be seen that the infrared physics is definitely not a new area of science, or physics for that matter, with sir Herschel's experiments conducted in 1800 and Planck's formula derived in 1900. Although there is still a missing part of the far-infrared spectrum depicted as the so-called terahertz-gap [61], due to the lack of small coherent sources. This altogether has been the reason for significant growth of THz physics and technology over the past few decades [62].

3.1.2 THz sources

Nowadays the terahertz range is somewhat a well developed range of electromagnetic spectrum, equipped with an array of sources with power of megawatt or kilowatt ranges, some of which include frequency tunable free-electron lasers, molecular lasers or femtosecond-fast broadband sources, BWO (backward wave oscillator), Gunn diodes, klystrons [63]. Unfortunately it must be admitted that terahertz technologies suffer from one important drawback, which is the lack of availability of relatively cheap semiconductor continuous wave (CW), tunable monochromatic sources.

One of the first used terahertz radiation sources were globars and high-pressure mercury lamps. They were used to uncover the origin of Reststrahlen bands and other fundamental laws of terahertz radiation. Such thermal sources made it possible to perform broadband Fourier-transform spectroscopy, which is one of the most important methods of spectroscopy in MIR/THz range. Currently, globars and high-pressure mercury lamps are commonly used in THz spectroscopy. However, certain applications require monochromatic sources of a specific wavelength, such as THz magneto-spectroscopy [63].

Monochromatic THz sources can be presented by various devices operating based on different physical phenomena. Those devices are represented by Gunn diodes (operating on Gunn effect in semiconductor), vacuum electronics - BWO, gyrotrons, electronic sources based on frequency multiplying of microwave sources [63]. Apart from previously listed monochromatic sources, there are sources of THz radiation using laser, for example: optically pumped molecular lasers, quantum-cascade lasers and free-electron lasers.

3.2 Magneto-transmission

Magneto-transmission is an important experimental tool as it provides a mean of studying the electronic properties of the materials. By measuring how the transmission of electromagnetic radiation changes as a function of the

magnetic field strength or direction, we can gain an insight into the electronic structure of the material under study.

One of the techniques used in this thesis was magneto-transmission measurements performed at cryogenic temperatures. The effect of magnetic field on the electronic system can be defined as an introduction of filled and empty bands, which form a set of energy levels called Landau levels (LLs). This experimental method is not without its limitations. Mainly it requires stabilization of the parameters of used equipment - power of the source, as well as temperature of the crystal and bolometer.

The measurements of the magneto-transmission were performed in the Laboratory of THz Spectroscopy at the Faculty of Physics, University of Warsaw.

3.2.1 Experimental setup

During the studies two types of experiments were carried out:

- Magneto-transmission with the sample in liquid helium (LHe) bath,
- Magneto-transmission with the sample in the pressure cell in a frozen compound of transformer oil and kerosene (50/50), at different hydrostatic pressures.

In both cases, transmission experiments were carried out in a cryostat that has a superconductive coil, is filled with pumped LHe at T = 2 K, with magnetic fields of up to 5 T. This cryostat has two separate chambers, one that is permanently filled with liquid nitrogen and another that is filled with liquid helium.

During the measurements at the LHe bath a special sample holder was used. Fig. 3.1 (a) presents this sample holder with two samples glued on top of it, beneath those samples there are two holes allowing THz radiation to penetrate through the holder in order to measure transmission on the bolometer, mounted underneath the holder. Panel (b) presents the side view of the ending of the cryostat insert, with the pins used to attach the sample holder

to the insert. Panel (c) presents a side view of cryostat insert prepared to be used for experiments. The cryostat insert ends with a brass cone that focuses the incident radiation on the sample. Fig. 3.2 presents the used experimental setup. The sample was then placed inside a variable temperature insert (VTI), which controls the temperature of the sample. As a detector of THz radiation thinned Allan-Bradley resistor was used.

A custom-made bronze clamp pressure cell with an optical access (sapphire window) was used to perform experiments in the hydrostatic pressure. The pressure transmitting medium was a mixture of kerosene and transformer oil. The sample was placed on the spring supported, triple-level sample holder as close to the sapphire window as possible. This solution ensured the reduction of absorption of the THz radiation by the pressure transmitting liquid. The bolometer was placed directly underneath the sample. Additionally an InSb pressure gauge was used to have a direct read-out of the pressure inside the pressure cell, both at the room and cryogenic temperature. Fig. 4.3 presents the holder with a sample mounted on top of it. The initial pressure was applied at the room temperature, after that the pressure cell attached to the insert was carefully and slowly cooled down to the temperature of 2 K. After the cooling down process the pressure value was significantly lower and the measurements were ready to begin. As a THz source a far-infrared (FIR) molecular CO_2 laser was used. Other lower energy range THz sources include backward wave oscillator and a VDI. Seven optical lines were used are presented in tab. 3.1.

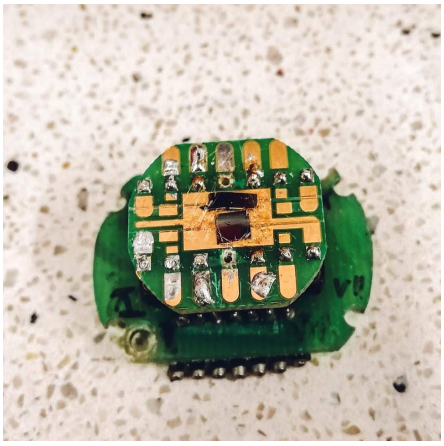
All spectra were normalized by the power of the laser which was constantly monitored by the pyroelectric detector.

Optically pumped molecular far-infrared laser

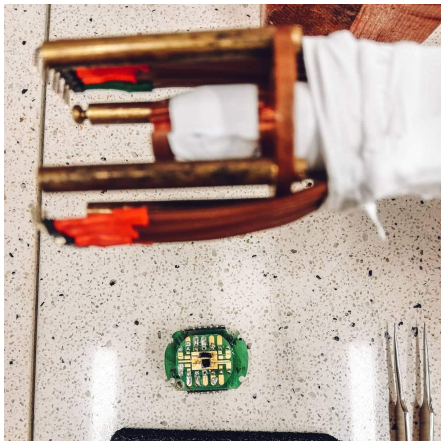
Optically pumped molecular lasers consist of two lasers, first one is used as a pump source, while the second as THz radiation source. Mostly CO_2 or

Table 3.1: Used optical lines with their sources.

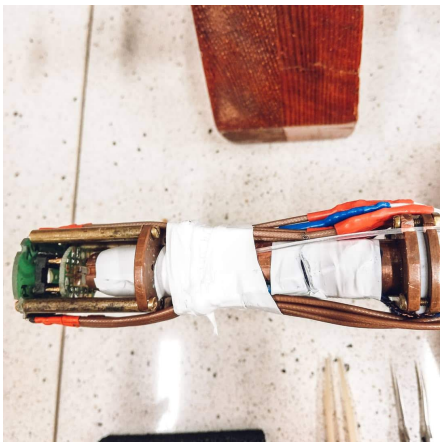
Wavelength [THz]	Wavelength [μm]	Energy [meV]	Source
4.3	70.6	17.6	FIR molecular laser
3.1	96.5	12.9	FIR molecular laser
2.5	118.8	10.4	FIR molecular laser
1.8	163	7.6	FIR molecular laser
1.6	186	6.7	FIR molecular laser
0.9	334.6	3.7	BWO
0.7	454	2.7	VDI



(a) Two samples glued to the sample holder



(b) View of the attachment for the sample holder to the insert



(c) Cryostat insert

Figure 3.1: Sample holder and cryostat insert for the measurements at liquid helium bath.

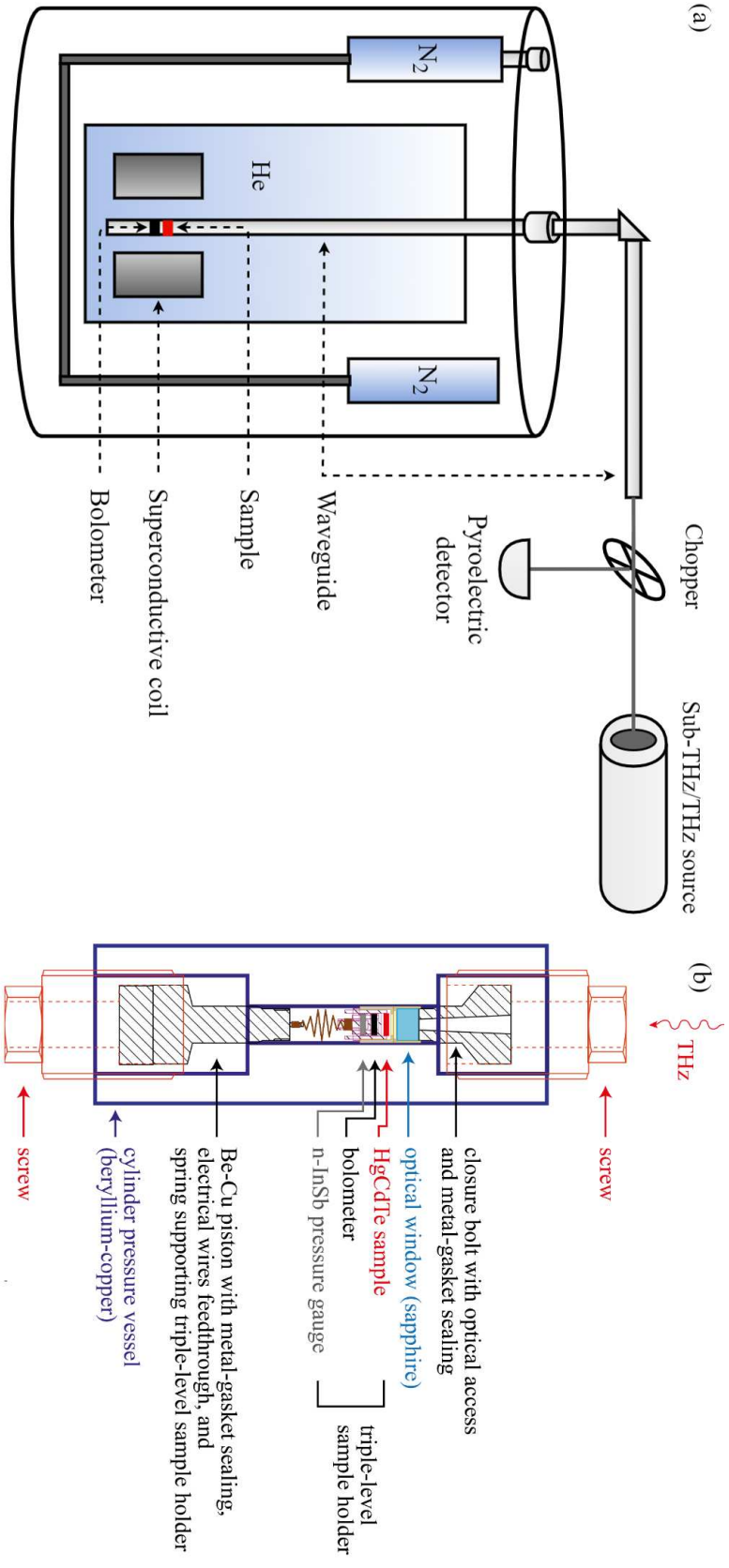


Figure 3.2: Experimental setup (a) and pressure cell (b).

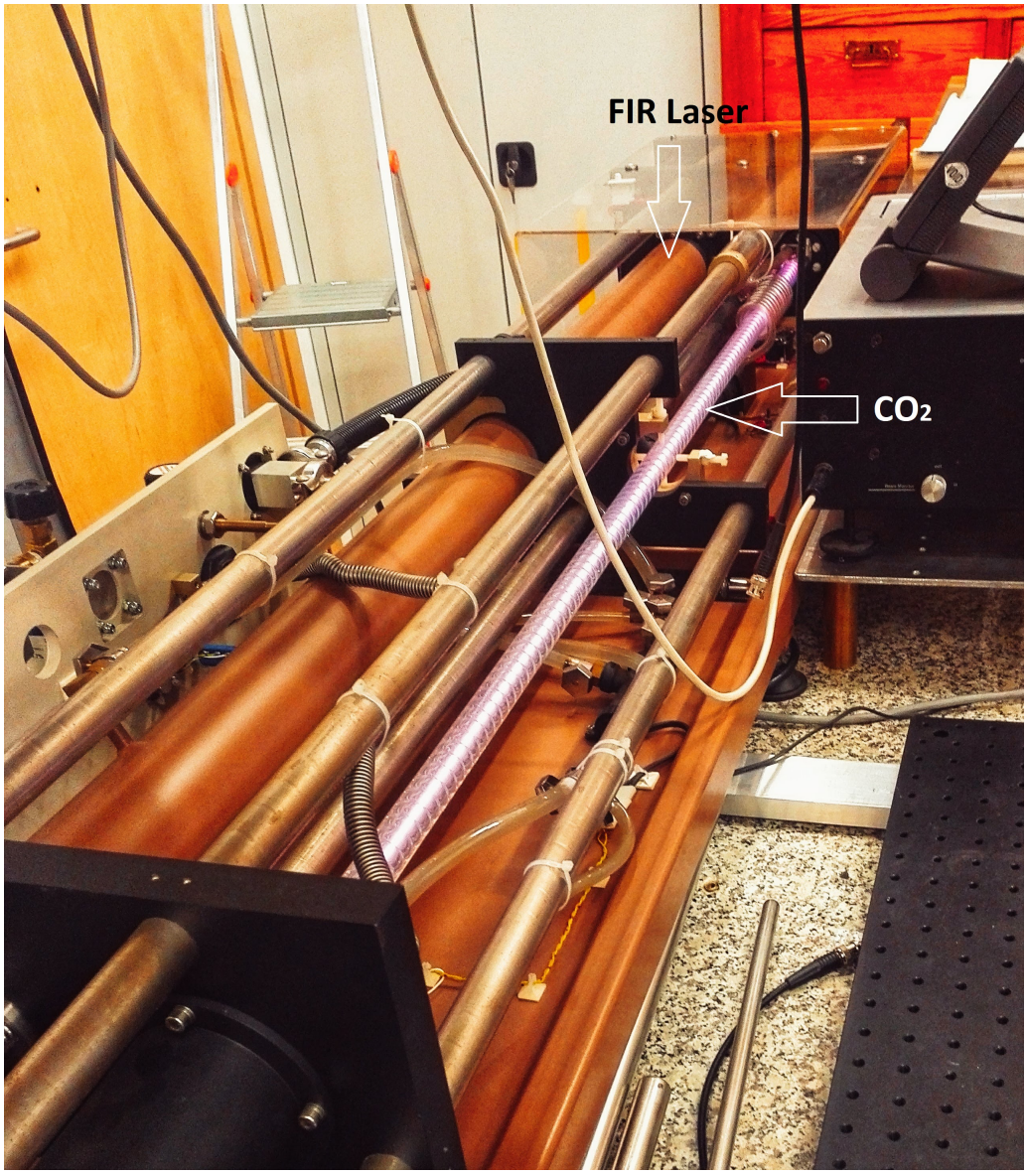


Figure 3.3: Operating CO_2 pumped FIR laser at the laboratory of THz spectroscopy (Faculty of Physics, University of Warsaw).

N_2O lasers can be used as pump sources, while CO_2 laser is mostly used as a pump source nowadays.

CO_2 laser was chosen as a pumping laser due to the opportunity of tuning such a laser in the range of 9.2 - 11.2 μm. Something that isn't possible with the use of low-power continuous wave (CW) pump radiation. In order to find conditions that would be agreeable for lasing in the THz range, one must concentrate on finding convenient gain media and such lines of CO_2 laser that

Table 3.2: FIR laser output specifications. Source: www.edinst.com/products/firl-100-pumped-fir-system.

$\lambda(\mu m)$	FIR molecule	CO_2 pump line	Power
96.5	CH_3OH	9R10	60 mW
118.8	CH_3OH	9P36	150 mW
184.3	CH_2F_2	9R32	150 mW
432.6	HCOOH	9R20	30 mW
513.0	HCOOH	9R28	10 mW

would become in resonance with corresponding molecular transitions. Up to date thousands lines were found, covering almost the whole THz range, with wavelengths from 20 μm to 2 mm.

This part of the experimental work was prepared with the use of FIRL-100 FIR Laser (Edinburgh Instruments), as presented in the fig. 3.3. The CO_2 section provides lines ranging from 9.1 μm and 10.9 μm and is equipped with a flowing gas single discharge tube offering up to 50 W within the strongest line. In order to couple CO_2 laser output into the FIR laser two steering mirrors and ZnSe lens are used. Tab. 3.2 presents typical FIR laser output specifications. I was mostly working using methanol as FIR molecule and obtained up to 5 lines: 70.6 μm, 96.5 μm, 118.8 μm, 163 μm and 186 μm, with 118.8 μm being the strongest line as it is using 9P36 CO_2 pump line. For THz spectroscopy used in semiconductor research finding new laser lines is not as important as finding strong and stable laser emission at a single frequency. Another important feature of FIR lasers is the laser gas pressure. For low pressures the collision rate is small but at the same time the laser gain is low because there are only a few molecules in the pump beam. At high pressures the density of molecules is high but the degree of inversion is small because of the collisions. Which means that there is a most favorable pressure for every laser line.

From my experience, operating FIR molecular lasers requires experience, intuition and patience as it rarely works steadily, especially for the smaller wavelengths. Additionally FIR laser is large and requires an equally large CO_2 laser, as well as high voltage power supply. Each of these disadvantages

contributes to the fact that they are less often used, now when there are other available sources of THz radiation, like quantum cascade lasers.

3.3 Fourier-transform infrared spectroscopy (FTIR)

The measurements of magneto-reflectivity were performed using the setup with infrared Fourier spectrometer, which was used for probing of the materials band structure. This particular technique allows examination of the optical response of solids with the use of polychromatic sources of radiation. As a result an interferogram is obtained, which provides information about the dependence of intensity of the light as a function of the position of a mirror inside the interferometer. Interferogram can be easily converted into a wavelength-dependent signal via Fourier-transformation. Nowadays typical setup used for FTIR experiments is build from: light source, interferometer (predominantly Michelson interferometer), sample placed in cryogenic temperatures and magnetic field, and a detector reading out the response. The arrangement of the latter depends on the type of measurement, and is placed outside the cryostat when measuring th reflectivity.

Main advantage of this method over any grating infrared spectroscopy technique, is the possibility to obtain spectral information about a wide range of photon frequencies simultaneously (Felgett's advantage). Moreover high throughput increases a signal-to-noise ratio, which in return compensates weak brightness of sources used in the infrared range. This is due to the fact that slits which reduce the aperture aren't needed, in return this allows for the whole signal to be recorded at once (Jacquinot's advantage). Finally the only movable part of FTIRs is the interferometer mirror. The position of said mirror is calibrated by a laser passing through an interferometer. In return this eliminates the possibilities of inaccuracies of readout of the photon frequency, caused by misalignment of the mechanical parts, as can happen in dispersive setups (Connes' advantage) [64].

All of the FTIR measurements were performed at the Laboratoire National des Champs Magnétiques Intenses (LNCMI), Grenoble.

3.3.1 Experimental setup

Figure 3.4 presents the FTIR-equipped setup used for the magneto-reflectivity measurement. The infrared radiation is generated by either one of three sources: mercury lamp, Globar or tungsten filament. When reaching the interferometer, the radiation beam is divided into two branches. The length of one of them is modified by the movable mirror, while the length of the other one remains the same, as can be seen in 3.5. This allows the constructive and destructive interferences of the individual wavelengths to define the spectral profile of the outgoing beam [65]. A detector measures the intensity of the radiation at each of the mirror positions. As a result an interferogram is created which can be transformed into the domain of frequencies by Fourier transformation. In this thesis a commercially available spectrometer was used (Bruker Vertex 80v), alongside two poly-chromatic thermal sources (Mercury lamp and Globar) and three different beam-splitters (T230 - silicon, T222 - mylar multilayer and KBr). In order to suppress the infrared-active components from air molecules the whole optical path was pumped. The output beam of the spectrometer was guided onto a gold-covered parabolic mirror placed on a removable stage on top of the probe. Radiation was then guided, through a gold-plated waveguide and focused by an optical cone onto the sample. The reflected light was guided back into the external bolometer, through the same waveguide. The external bolometer was placed outside in a separate cryostat. The entire probe area was under low-pressure helium, which allowed a heat transfer between the probe and the LHe bath inside the cryostat. The cryostat was equipped with superconductive solenoid reaching up to 16 T. During the measurement the magnetic field was always applied perpendicular to the surface of the sample.

The external bolometer contains of two separate detectors units. Each of them consists of its own optical window and a condensing cone. The one equipped with TPX window allows one to measure in the far-infrared range,

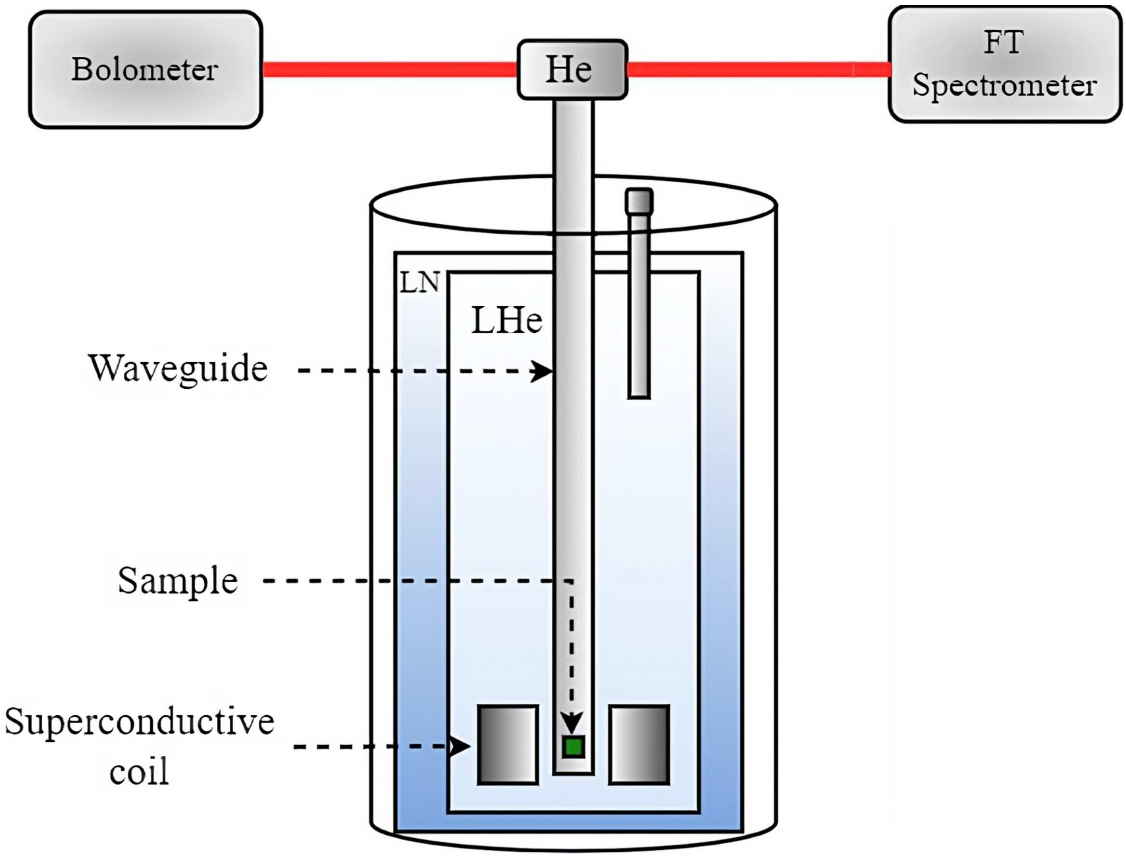


Figure 3.4: Experimental setup for Infrared Fourier Spectroscopy.

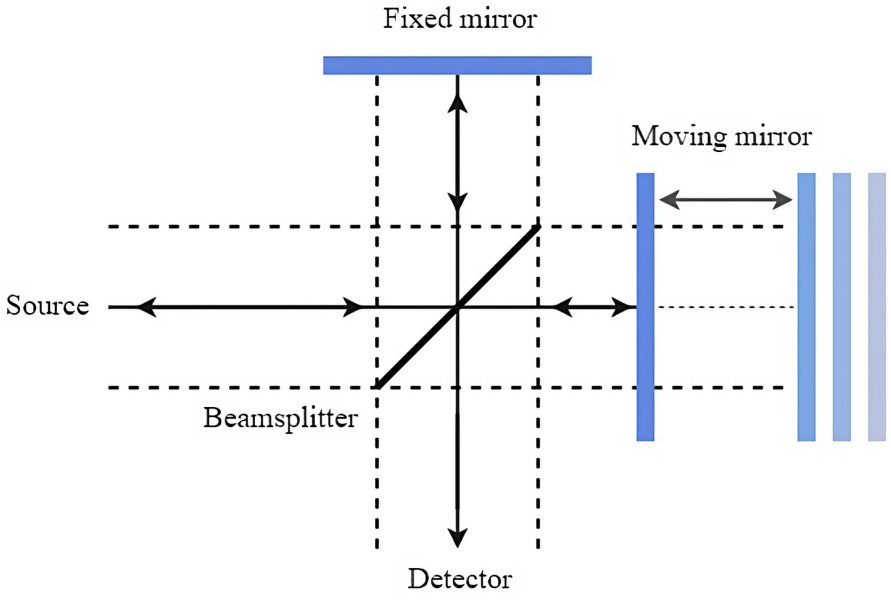


Figure 3.5: Layout of Michelson interferometer.

while the other one with KRS5 window, at the mid-infrared range. The external bolometer is cooled down to 2 K via pumping the evaporated helium gas.

During the measurements at LNCMI a high-magnetic field installation (up to 34 T) was also explored. The resistive coil used in this setup is made out of two parts - outer Bitter coil, and the inner co-centric helical insert with a bore diameter of 34 mm. The installation can reach up to 25 MW of power. In order to disperse the Joule heating two hydraulic pumps are used. The hydraulic pumps allow for the 150 l/s flow rate. The reflectivity setup operates at the same principle as superconductive coil equipped setup, with the additional use of 4 m long waveguide, which allows one to keep the magnetic field as low as possible at the location of the FTIR spectrometer.

3.4 Summary

In this chapter the use of THz spectroscopy while studying optical properties of materials is discussed. As well as description of two experimental setups for studying these properties: magneto-transmission and FTIR spectroscopy with a Michelson interferometer.

THz spectroscopy uses the electromagnetic radiation in the THz frequencies to probe the optical properties of materials. It has become a vital tool in the study of condensed matter systems, as it allows for the investigation of the behavior of materials at low energies and in the presence of strong magnetic fields.

In addition to band gap determination, specific Landau dispersion is also an important tool in analyzing the electronic properties of materials. This technique helps to discriminate between Schrödinger and Dirac electrons, which is crucial for understanding the behavior of certain materials. A key aspect of this technique is the ability to reconstruct the Landau level fan chart, which allows one to define whether they are dealing with a parabolic or linear dispersion, among other properties. Understanding the specific Landau dispersion of a material is essential for characterizing its electronic properties.

The magneto-transmission setup was used to measure the transmission of THz radiation through a sample placed inside the magnetic field and hydrostatic pressure cell. This method allows for the study of the electronic properties of the material, like the formation of Landau levels.

FTIR spectroscopy with a Michelson interferometer involves the measurements of the dielectric function of the material, which is related directly to its optical properties. With the analysis of the interferogram, obtained as a result, one can obtain information about the material's electronic structure and optical transitions.

Overall, the chapter highlights the versatility of THz spectroscopy and the various experimental setups that can be used to study the optical properties

of materials. The described techniques allowed the valuable insight into the behavior of materials in different conditions, like magnetic field and hydrostatic pressure.

4

Topological phase transition of $Hg_{1-x}Cd_xTe$ driven by hydrostatic pressure probed by THz magneto-spectroscopy

Contents

4.1 Introduction 51
4.2 Influence of the substrate 55
4.2.1 Samples - $Hg_{1-x}Cd_xTe$ epitaxial layers 55
4.3 Experimental results 56
4.4 Landau-level transitions 59
4.5 Discussion 63
4.6 Summary 67

The findings presented in this chapter have been published in an article titled 'Hydrostatic deformation potentials of narrow-gap HgCdTe' in Phys. Rev. B.

4.1 Introduction

Mercury cadmium telluride (MCT - crystallographic structure presented in fig. 4.1) is a material used in MIR-FIR photodetectors [66]. Its manufacturing technology process has been evolving during the last twenty years [67]. This

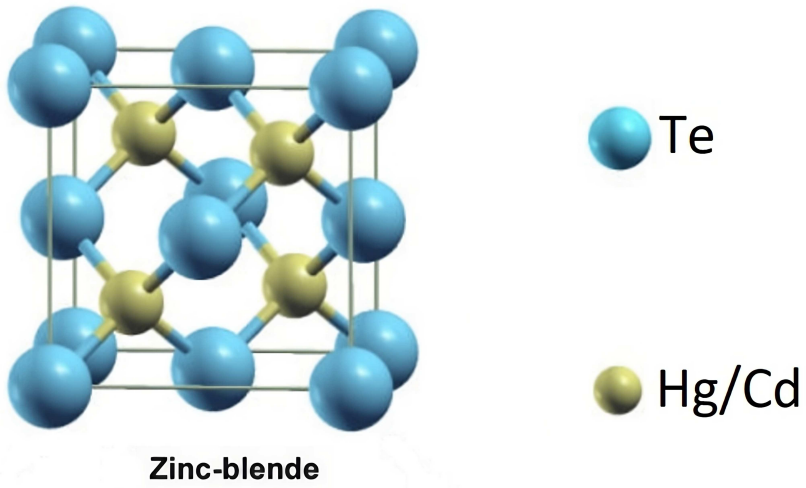


Figure 4.1: Crystallographic structure of HgCdTe. Adapted from: [73], with the permission of publisher.

development has paved the way for the possible use of HgCdTe in the technology of THz sensors [68, 69] and lasers [70–72]. Key factors of advantage of MCT include direct band-gap and its wide tunability, high mobility of electrons and low dielectric constant.

Band structure of HgCdTe can be tuned continuously from the inverted band semimetal phase of HgTe [74] to a conventional semiconductor - CdTe, see fig. 4.2. The tuning can be achieved via various parameters - temperature, Cd concentration and pressure [75, 76]. The band inversion in MCT, that occurs between Γ_6 and Γ_8 bands, can be observed for $x \leq x_c$, where x_c is a temperature-dependent parameter ($x_c \simeq 0.165$ at 2 K and $x_c \simeq 0.155$ at 77 K [75]). Hence HgCdTe can be called a semimetal with a negative pseudo gap E_g, when assuming the energy difference that occurs between Γ_6 and Γ_8 bands. The possibility of band inversion leads to different topological states of matter both in HgCdTe bulk films [21, 77–80] and HgTe/HgCdTe quantum wells [81–84]. HgCdTe alloys present a temperature-dependent band-gap, which allows for the temperature tuning of topological phase transitions in HgCdTe heterostructures [85–87].

The band structures of three-dimensional and two-dimensional systems are significantly impacted by both intrinsic and applied strains. These strains

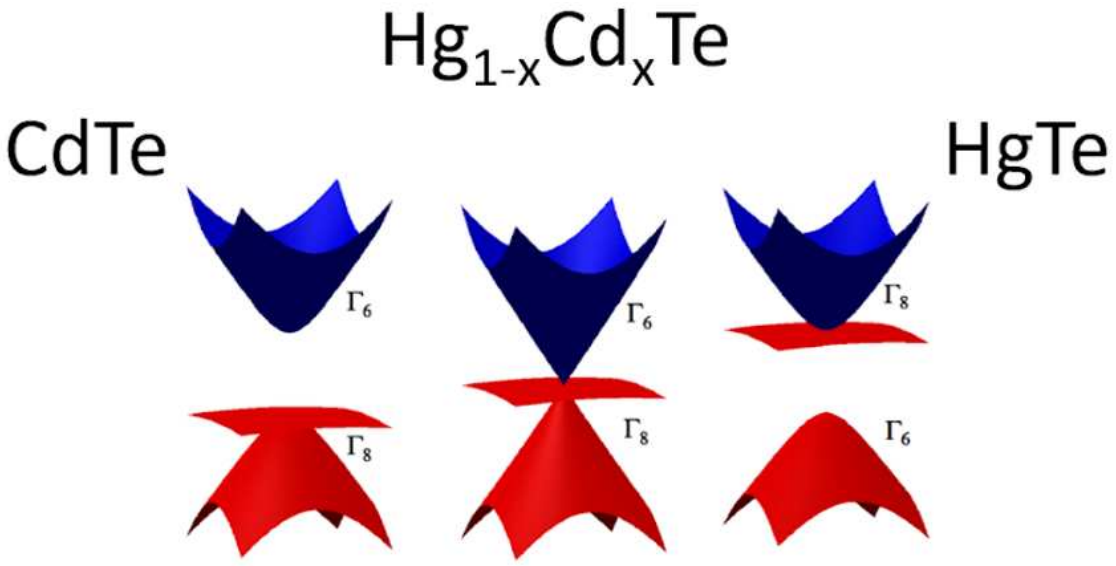


Figure 4.2: The band structure tuning from CdTe to HgTe, through gapless state for $Hg_{1-x}Cd_xTe$, with $x = 0.16$. Adapted from: [58], with the permission of publisher.

are characterized by the deformation potentials of the bulk materials, which describe how the band structures evolve under strain. One example of this is the way in which uniaxial strain, defined by the shear deformation potentials b and d, can split the Γ_8 band at the Γ point in the Brillouin zone and transform semi-metallic HgCdTe bulk films into either 3D topological insulators [21, 77, 88] or 3D Dirac/Weyl semimetals [78, 79]. On the other hand, hydrostatic deformation potentials a_c and a_v describe the evolution of the Γ_6 and Γ_8 bands, respectively, under applied strain. While the values of a_c and a_v cannot be directly measured experimentally, their difference, $a_c - a_v$, can be obtained from the hydrostatic pressure dependence of the direct band gap $E_g(P)$ or $\partial E_g/\partial P$.

Deformation potentials of bulk materials, such as a_c, a_v, b, and d, can be used to describe how the band structures evolve under different types of strain. By studying the hydrostatic pressure dependence of the direct band gap, one can obtain the information about the difference between a_c and a_v, which is crucial for understanding the impact of applied strain on the band structures of materials.

A significant number of studies have been conducted to investigate the $E_g(P)$, in MCT using various methods, including transport measurements,

Table 4.1: Pressure coefficients of the direct energy gap E_g for $Hg_{1-x}Cd_xTe$ bulk crystals obtained by various techniques: transport, optical absorption, reflectivity, and photoluminescence (PL).

	$\partial E_g/\partial P$ (meV/kbar)	T (K)	Method
$x = 1$	7.9±0.2	300	reflectivity [89]
	8.0		PL [90]
	8.3		absorption [91]
	8.4		absorption [92]
	7.9±0.2	77	PL [93]
	6.5±0.2	2	PL [1]
$x = 0.7$	8.7	300	absorption [94]
$x < 0.3$	8.7	> 77	transport [95]
$x = 0.27$	10.0	4.2	transport [96]
$x = 0.164$	8.0	300	transport [97]
$x = 0.15$	7.0	77	transport [98]
	3.0		transport [99]
$x = 0$	10.4±0.6	300	transport [100]
	8.72±0.25		absorption [101]

optical absorption, reflectivity, and photoluminescence, as well as theoretical calculations. These studies are reported in references [1, 89–101]. The values of $\partial E_g/\partial P$ obtained from these experiments are summarized in 4.1. However, the large scatter in these values can be attributed to differences in the experimental techniques used, which can lead to uncertain parameter values. For example, to extract $\partial E_g/\partial P$ from transport data, one must use models with unknown third-party parameters that can vary from study to study [95–100]. On the other hand, more reliable data can be obtained from optical absorption, reflectivity, or photoluminescence, as they allow for a more direct measurement of E_g.

To date, the most self-consistent values of $\partial E_g/\partial P$ and deformation potentials for $Hg_{1-x}Cd_xTe$ have been obtained through linear interpolation between the values measured for CdTe [89–92] and those measured for HgTe by Latussek *et al.* [101]. These values of HgTe were derived from optical absorption measurements of $HgTe/Cd_{0.7}Hg_{0.3}Te$ superlattices, using advanced numerical band structure calculations. While the deformation potentials $a_c - a_v$ for CdTe [89–92] and HgTe [101] were only determined at room temperature, they

have been widely used to theoretically describe low-temperature investigations of HgTe/HgCdTe quantum wells [77, 79, 82, 86, 87].

4.2 Influence of the substrate

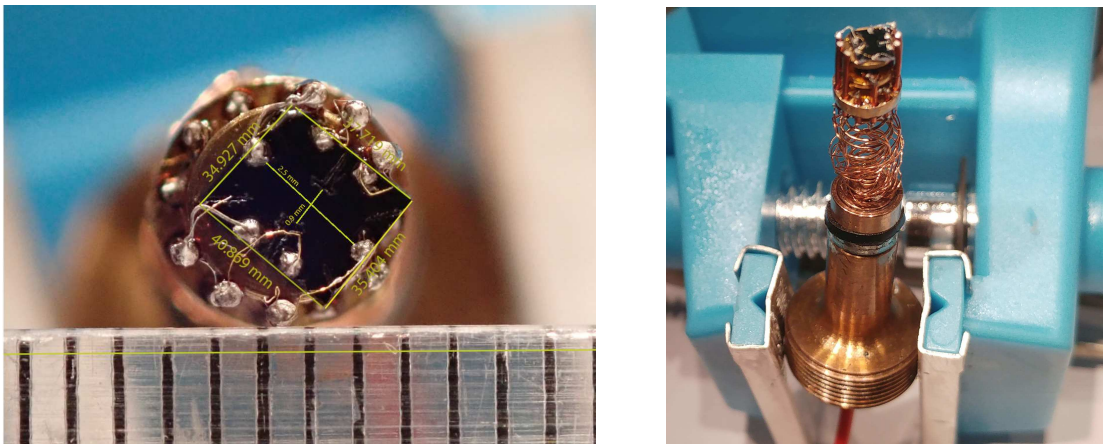
The substrate can play a significant role in multi-layer systems, especially in pressure/strain dependent measurements. Recently, experiments were conducted on samples with etched substrates of GaAs [102]. The study shows magneto-optical measurements performed on as-grown sample as well as on a sample after the substrate was removed. As a result the pressure coefficients were similar (within 20%) to each other in both cases. The authors explain this discrepancy by the presence of the CdTe buffer layer, that is separating the epitaxial layer from the substrate. Moreover it is discussed that it absorbs the stress which appears from the different elastic properties of GaAs and $Hg_{1-x}Cd_xTe$.

4.2.1 Samples - $Hg_{1-x}Cd_xTe$ epitaxial layers

The bulk $Hg_{1-x}Cd_xTe$ samples were grown by molecular beam epitaxy. The Cd concentration was chosen in the range near the critical value $x_c \simeq 0.165$ corresponding to the semimetal-to-semiconductor topological phase transition at 2 K [75]. Three (013)-oriented $Hg_{1-x}Cd_xTe$ layers with $x = 0.155$, 0.165 and 0.175 were used in this thesis. The samples were grown on semi-insulating GaAs substrate with relaxed CdTe buffers [103]. All films were sufficiently thick ($\approx 3.2\ \mu$m) to be considered as 3D materials and thin enough to be transparent in the far-infrared spectral range. We used a special ultra-high vacuum multi-chamber molecular beam epitaxy set, which allows for the growth of very high-quality HgCdTe crystals monitored by *in situ* reflection high-energy electron diffraction and single wavelength ultra-fast ellipsometry (0.5 nm).

Parameters of the samples are listed in Table 4.2.

The remaining information about the samples can be found in the Annex.



(a) planar view **(b)** side view

Figure 4.3: Pictures present planar view (a) and side view (b) of the sample mounted on the holder, which was a part of a pressure cell.

Table 4.2: Parameters of $Hg_{1-x}Cd_xTe$ samples studied in this work.

Sample	x	Carrier concentration at 77 K
A	0.152	$n = 4.3 \cdot 10^{15}$ cm^{-3}
B	0.165	$n = 3.5 \cdot 10^{15}$ cm^{-3}
C	0.172	$n = 2.8 \cdot 10^{15}$ cm^{-3}

4.3 Experimental results

In order to determine $a_c - a_v$ value a series of measurements of different samples (A, B, C) in magneto-transmission in the THz range as a function of P was performed.

Figs. 4.4, 4.5 and 4.6 present the results of magneto-transmission spectra of samples A, B and C, respectively. The presented spectra contain up to four absorption lines (marked with black triangles), which are identified as Landau level transitions. Each of the presented spectra are a result of an average of multiple measurements. This procedure was done to achieve better signal-to-noise ratio, especially among the higher energy lines of CO_2 pumped FIR-molecular laser, which by default are less intensive and less stable in time.

During the pressure experiments a number of problems were encountered. In the time of the measurements of sample B, through the faulty closing of

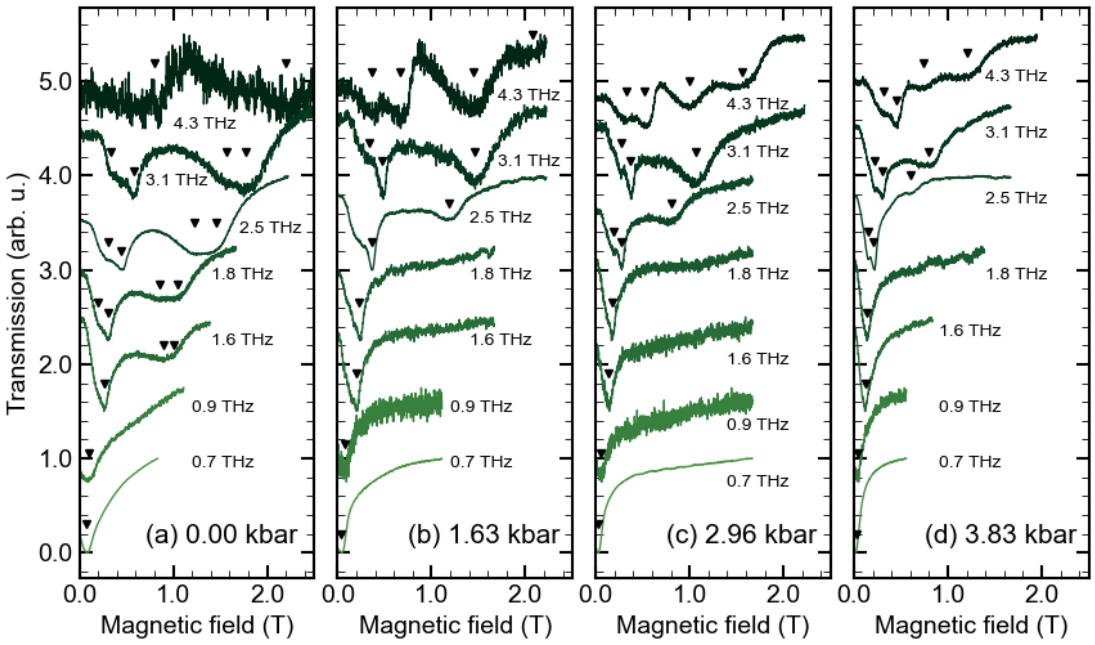


Figure 4.4: Magneto-transmission spectra of sample A measured at four different hydrostatic pressures $P_0 = 0.0$ kbar, $P_1 = 1.63$ kbar, $P_2 = 2.96$ and $P_3 = 3.83$ kbar.

the pressure cell, the quartz window cracked. This accident left our pressure cell broken (it had to be re-polished) and sample with bolometer turned to dust. This problems translated into only two pressure measurements shown for this sample. While measuring the sample C after a few measurements we noticed that a sample is cracked in a lot of places on its surface, probably because of the faulty mounting on the holder. This led us to reject a series of experiments performed on this samples, as we were not able to trace back when the breaking of the sample occurred.

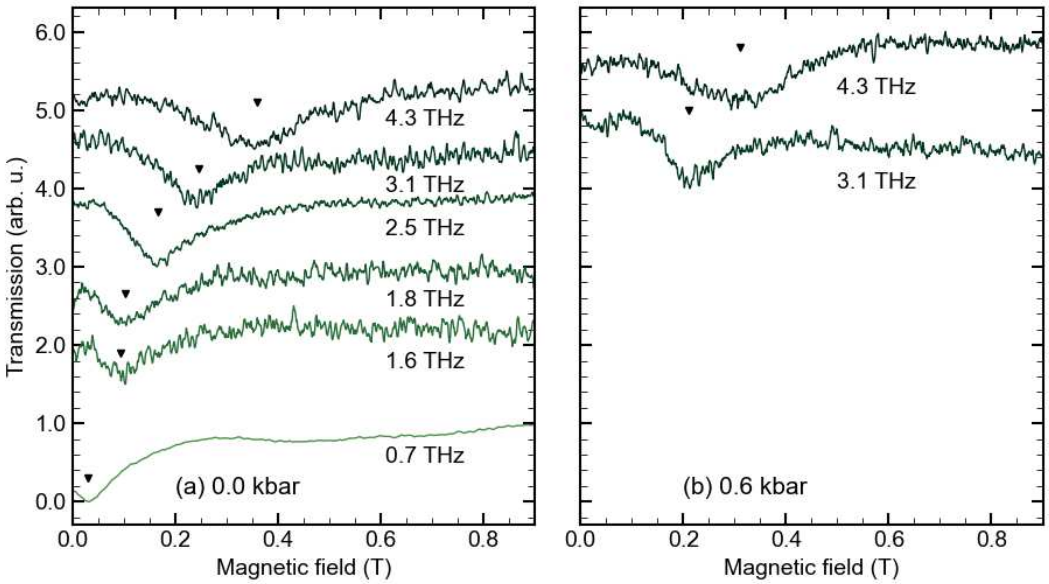


Figure 4.5: Magneto-transmission spectra of sample B measured at two different hydrostatic pressures $P_0 = 0.0$ kbar and $P_1 = 0.6$ kbar.

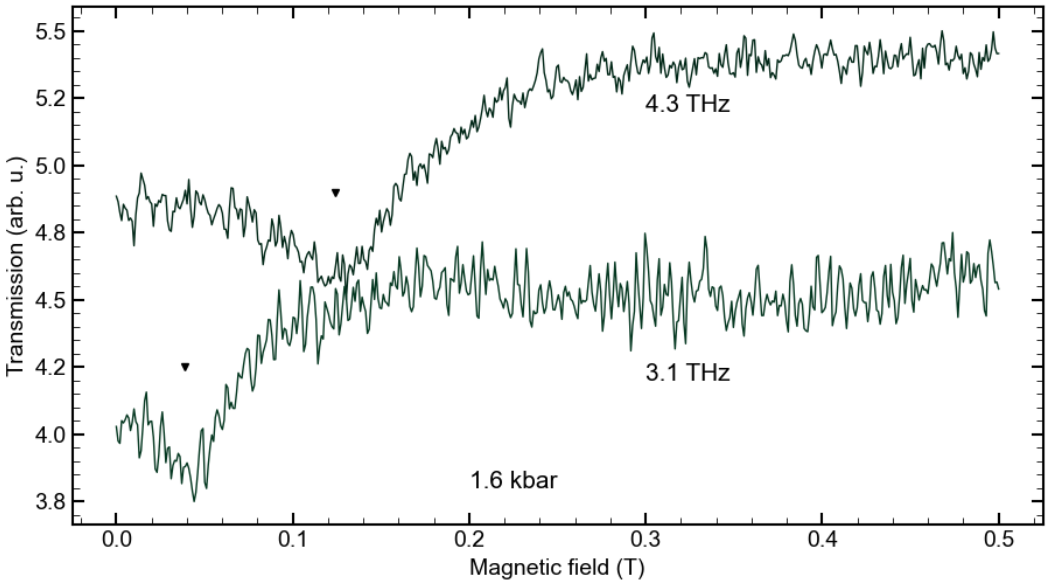


Figure 4.6: Magneto-transmission spectra of sample C measured at pressure $P_1 = 1.60$ kbar.

4.4 Landau-level transitions

A simplified Kane model [75] was used to describe LL transitions. This model takes into account only linear terms in $k \cdot p$ interaction between Γ_6 and Γ_8, without taking into account the interactions of Γ_7 split-off band. Due to the hybridization of the two Γ_8 bands the 6×6 Hamiltonian describing the dispersion of relativistic 3D particles cannot be reduced to a Dirac Hamiltonian. In this way we move forward with the term "Kane fermions" as describing the particles which Hamiltonian is invoked for the band structure of HgCdTe in the vicinity of topological phase transition.

This 6×6 Hamiltonian's three double-degenerated eigenvalues can be described as [75]:

$$E_\xi(p) = \xi^2 \tilde{m}\tilde{c}^2 + (-1)^{1-\theta(\tilde{m})}\, \xi \sqrt{\tilde{m}^2\tilde{c}^4 + p^2\tilde{c}^2}, \tag{4.1}$$

where p is an absolute momentum value and $\theta(x)$ is a Heaviside step function, equal to 1 for $x \geq 0$, to 0 when x is of negative value. The eigenvalues take on three forms. The first one for $\xi = 0$ is corresponding to the dispersionless, in the linear approximation, Γ_8 heavy-hole band. The second and third ones are describing the electrons Γ_6 conical bands for $\xi = +1$ and Γ_8 light-hole for $\xi = -1$. The Γ_6 and Γ_8 conical bands are separated by the band-gap $E_g = 2\tilde{m}\tilde{c}^2$. In this equation $\tilde{m}$ and $\tilde{c}$ are representing the rest-mass and asymptotic velocity of Kane fermions [75], accordingly.

The topological phase transition, in HgCdTe, between semimetal and semiconductor is described by the rest mass parameter $\tilde{m}$ from Eq. (4.1). While $\tilde{m}$ presents negative values it corresponds to the band inversion non-trivial topology with Γ_6 band lying below the Γ_8 bands. Due to the always touching Γ_8 bands at the Γ point of the BZ, the HgCdTe is a semimetal at a $\tilde{m} < 0$. While $\tilde{m}$ presents positive values the crystal is a conventional narrow-gap semiconductor and the p-type Γ_8 bands lying below s-type Γ_6 band.

Magnetic fields transform the energy dispersion of conduction and valence band into Landau levels [75]:

$$E_{\xi,n,\sigma}(p_z) = \xi^2 \tilde{m}\tilde{c}^2 + (-1)^{1-\theta(\tilde{m})} \times \\ \times \xi \sqrt{\tilde{m}^2\tilde{c}^4 + \frac{e\hbar\tilde{c}^2 B}{2}(4n-2+\sigma) + \tilde{c}^2 p_z^2}, \quad (4.2)$$

with n as the LL index, which values depends on ξ and p_z being a momentum projection onto direction of magnetic field. While $\xi = \pm 1$, then n assumes values of positive integers $n = 1,2,\ldots$ and for the zero-energy heavy-hole band ($\xi = 0$), n assumes non-negative integers, except 1: $n = 0,2,3\ldots$. Magnetic fields $\mathbf{B} = (0,0,B)$ lift Kramer's degeneracy by the quantum number σ. Electric-dipole selection rules determine the magneto-optical response as: $\Delta n = n \pm 1$ with "$\pm$" corresponding to the two circular polarizations, $\Delta p_z = 0$, $\Delta\sigma = 0$ with no restriction on the changes of ξ.

The equation (4.2) contains only two parameters ($\tilde{m}$) and ($\tilde{c}$) which can be determined from the field evolution of multiple LL transitions observed in magneto-transmission spectra. An analysis of LL transitions based on Eq. (4.2) gives, not only the absolute values, but also the sign of $\tilde{m}$ [75]. With the latter, it is possible to determine E_g for semi-metallic HgCdTe and probe the semimetal-to-semiconductor topological phase transition. An extrapolation of the energy of optical transitions in sample C determines the gap of said sample. For the sample A and B to the values of the negative pseudo-gap between the inverted Γ_6 conduction band and Γ_8 heavy hole band, were used. This allowed for the extraction of the band-gap value similarly as in the [75].

Figs. 4.7, 4.8 and 4.9 presents the analysis done for the samples A, B and C, respectively. These figures presents the positions of absorption energy minima, which are plotted in the function of the magnetic field, in a manner to plot Landau fan chart. The simplified Kane model is adopted to fit the data for three lines L_1, L_2 and L_3 which correspond to $L_{1,2,\downarrow} - L_{0,n,\downarrow\uparrow}$, $L_{1,1,\uparrow} - L_{0,n,\downarrow\uparrow}$ and $L_{1,1,\downarrow} -$

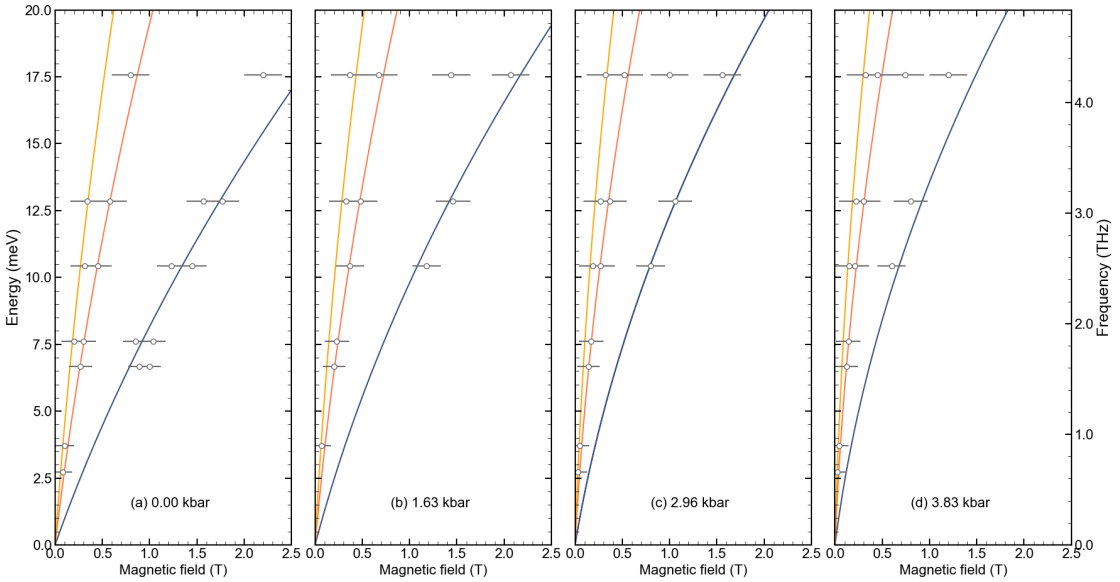


Figure 4.7: Landau level transitions for sample A at four hydrostatic pressures: (a) $P = 0$ kbar, (b) $P = 1.63$ kbar, (c) $P = 2.96$ kbar, (d) $P = 3.83$ kbar. Experimental data are represented by symbols. The full lines present the fits of the simplified Kane model [75] for three lines L_1 (blue), L_2 (orange) and L_3 (yellow) which correspond to $L_{1,2,\downarrow} - L_{0,n,\downarrow\uparrow}$, $L_{1,1,\uparrow} - L_{0,n,\downarrow\uparrow}$, $L_{1,1,\downarrow} - L_{0,n,\downarrow\uparrow}$ LL transitions (see Eq. (4.2)), respectively.

$L_{0,n,\downarrow\uparrow}$ LL transitions, accordingly (cf. Ref. [75]). For the data interpretation not all of the minima of magneto-transmission were taken into account. This is due to the fact of the attribution of the origin of this resonances to the ionization of the impurities [104]. The discussed resonances occur at around 1 T. This hypothesis can be also supported by the occurrence of various positions of said resonances between the three measured samples.

The joint density of states is most favorable for $p_z = 0$, which makes for the LL energies being sufficient enough at $p_z = 0$ to describe the magneto-optical transmission spectra. The rest mass $\tilde{m}$ was fitted during the analysis and the velocity $\tilde{c}$ was taken to be $\tilde{c} = (E_P/3m_0)^{1/2} = 1.05 \cdot 10^6$ m/s, where $E_P \approx 18.8$ eV is the Kane energy and m_0 is the free-electron mass [105]. It was already shown that the velocity $\tilde{c}$ is independent both of temperature and Cd content [75].

The joint result of band-gap evolution as a function of pressure for all of the measured samples can be found in fig. 4.10.

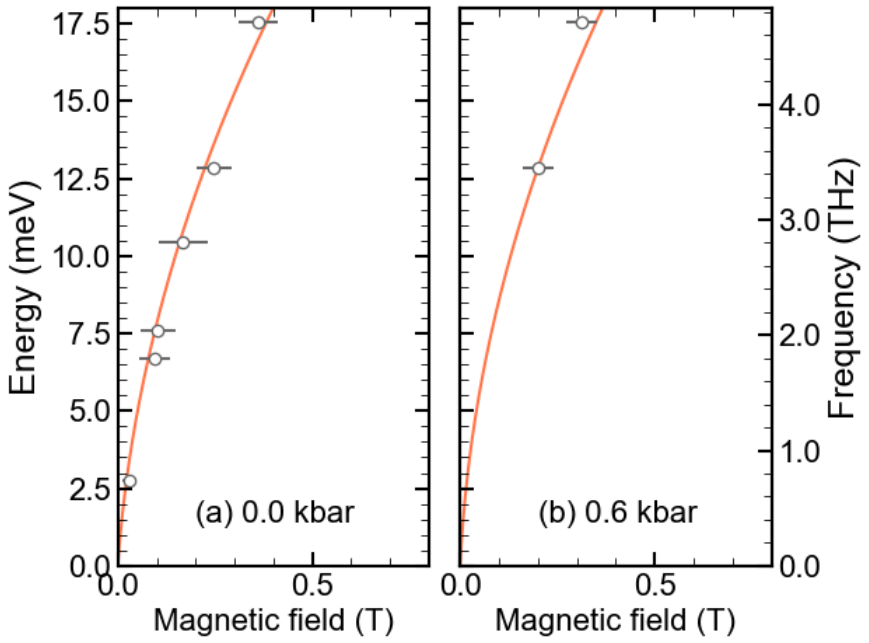


Figure 4.8: Landau level transitions for sample B at two hydrostatic pressures: (a) $P = 0$ kbar, (b) $P = 0.6$ kbar. Experimental data are represented by symbols. The full lines present the fits of the simplified Kane model [75] for line L_2, corresponding to $L_{1,1,\uparrow} - L_{0,n,\downarrow\uparrow}$, LL transitions (see Eq. (4.2)).

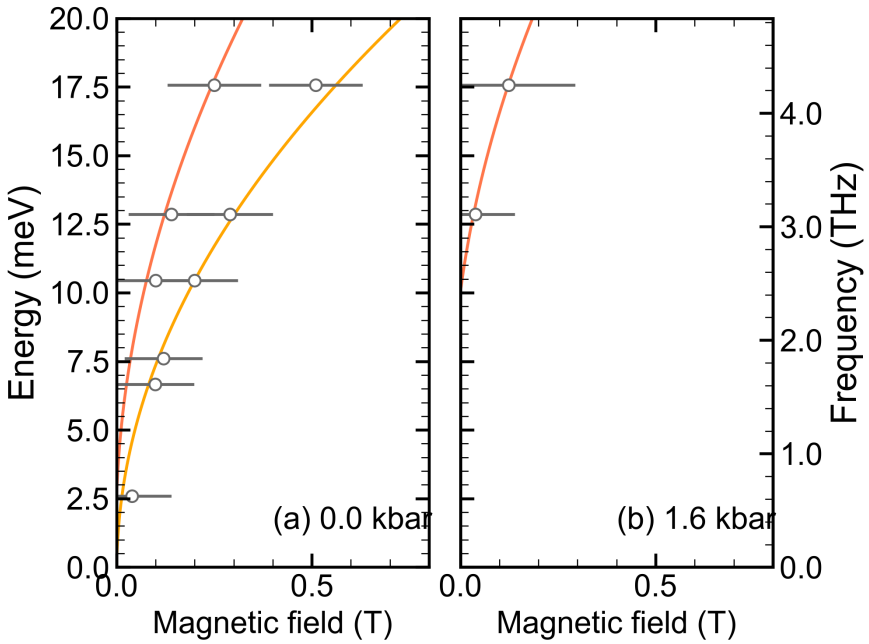


Figure 4.9: Landau level transitions for sample C at two hydrostatic pressures: (a) $P = 0$ kbar, (b) $P = 1.6$ kbar. Experimental data are represented by symbols. The full lines present the fits of the simplified Kane model [75] for two lines L_2 (orange) and L_3 (yellow) corresponding to $L_{1,1,\uparrow} - L_{0,n,\downarrow\uparrow}$, $L_{1,1,\downarrow} - L_{0,n,\downarrow\uparrow}$ LL transitions (see Eq. (4.2)), respectively.

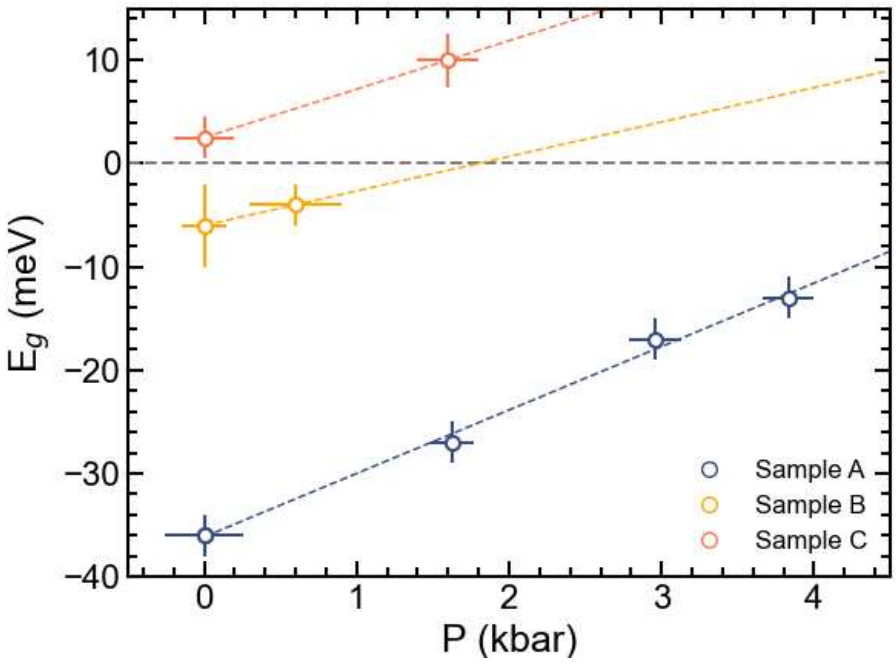


Figure 4.10: Band-gap evolution as a function of pressure. Results of all of the studied samples A, B and C.

4.5 Discussion

I will now calculate the values of $a_c - a_v$ using the experimental data presented in Figure 4.10. The pressure dependence of the band gap, $E_g = E_c - E_v$, in a bulk crystal is determined by the non-zero elements of the strain tensor ε_{ij}:

$$E_g(P,T) = E_g^{(0)}(T) + (a_c - a_v)(\varepsilon_{xx} + \varepsilon_{yy} + \varepsilon_{zz}). \tag{4.3}$$

The temperature-dependent band-gap in $Hg_{1-x}Cd_xTe$ in the absence of hydrostatic pressure is represented by $E_g^{(0)}(T)$ [75, 76], and the elements of the strain tensor are calculated using Murnaghan's equation of state [106].

$$\varepsilon_{xx} = \varepsilon_{yy} = \varepsilon_{zz} = \left(1 + P\frac{B_0'}{B_0(T)}\right)^{-1/3B_0'} - 1. \tag{4.4}$$

The temperature-dependent bulk modulus is represented by B_0, and its derivative with respect to pressure is $B_0' = \partial B_0/\partial P$. These are calculated using the elastic constants $cij(P,T)$ according to $c_{ij}(P,T)$ as $B_0(T) = (c_{11}(T) +$

$2c_{12}(T))/3$. It's worth noting that Eq.(4.4) is only valid when the elastic constants have a linear dependence on P [107, 108].

$$c_{ij}(P,T) = c_{ij}^{(0)}(T) + P\frac{\partial c_{ij}}{\partial P}. \tag{4.5}$$

In the above equation, $c_{ij}^{(0)}(T)$ represents the temperature-dependent elastic constants of $Hg_{1-x}Cd_xTe$ in the absence of hydrostatic pressure. The derivative of elastic constants with respect to pressure is assumed to be independent of pressure and temperature. As stated in Ref.[101], the elastic constants and its derivatives are assumed to vary linearly with the alloy composition x in $Hg_{1-x}Cd_xTe$. To calculate B_0', we used the values of $\partial c_{ij}/\partial P$ reported in Refs [107, 108], which are 3.23 and 3.83 for CdTe and HgTe, respectively. The values of $c_{ij}^{(0)}(T)$ at a specific x are based on the experimental data for CdTe and HgTe, obtained from measurements of ultrasonic wave velocities in bulk crystals [109].

With the help of Eqs.(4.3)–(4.5), the deformation potential $a_c - a_v$ was calculated from the band-gap E_g at non-zero pressures. To determine the deformation potential at $P = 0$, the Taylor expansion of Eq.(4.4) was utilized, which results in a quadratic dependence of $E_g(P)$ [101]. This expression allows to express the deformation potential with a linear coefficient $\partial E_g/\partial P$ at zero pressure. This coefficient was calculated by using $E_g^{(0)}(T)$ at $P = 0$ and the value at the lowest available pressure for the given sample. Then, using a set of $a_c - a_v$ values obtained from $E_g(P)$, the mean and variance of the deformation potential was calculated for a given sample (as can be seen in Table 4.2).

Figure 4.11 shows a summary of the deformation potential values for $Hg_{1-x}Cd_xTe$ obtained from the analysis of far-infrared magneto-optical spectroscopy. The values for the samples under study are represented by blue open symbols. For comparison, we have also added values of $a_c - a_v$ that were calculated from $\partial E_g/\partial P$ in Table 4.1 using the $B_0(T)$ at the corresponding temperature used in this work. However, it is important to note that in order to make this comparison, we have assumed that $\partial E_g/\partial P$ corresponds to measurements at

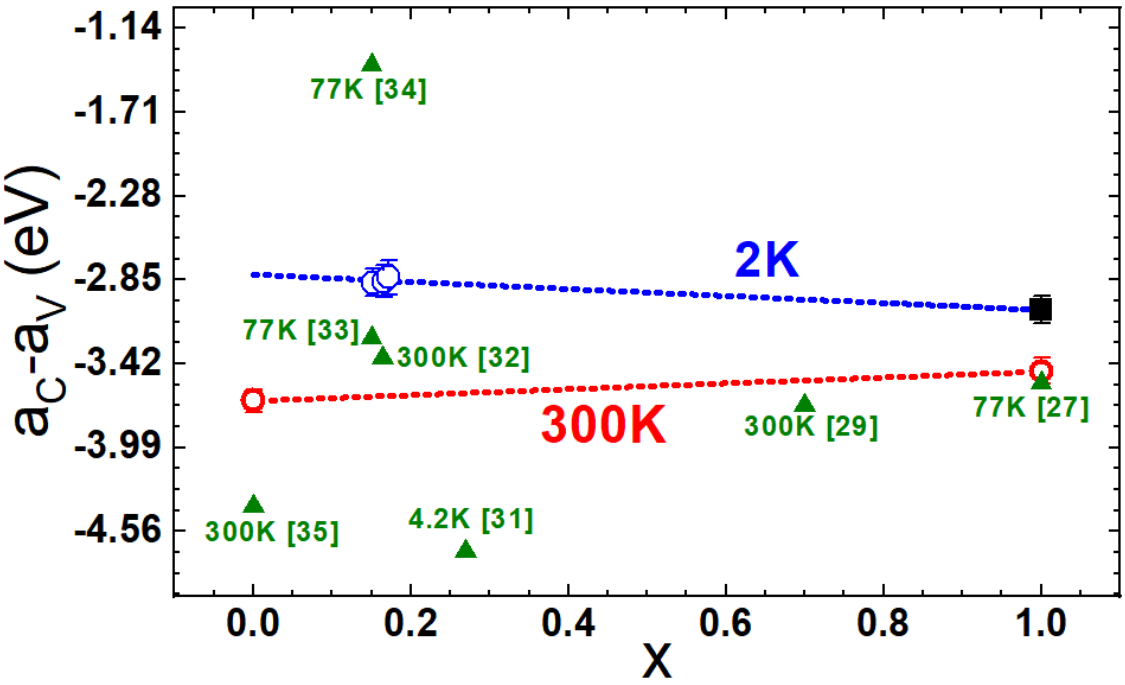


Figure 4.11: Deformation potential $a_c - a_v$ at cryogenic and room temperature. The red symbols and dotted line in the figure represent the values and linear interpolation of $a_c - a_v$ at 300K, which were recalculated from the results of Latussek *et al.* [101] using the current values of $B_0(T)$ and B_0' used in this work. The black symbol corresponds to the value of $a_c - a_v$ in CdTe, which was recalculated from the low-temperature data of Dunstan *et al.* [1] (see Table 4.1). The blue open symbols show the values obtained in this work (as can be seen in Table 4.2). The blue dotted line is the linear fit of $a_c - a_v$ at 2 K. The green triangles represent the values of $a_c - a_v$ recalculated from $\partial Eg/\partial P$ provided in Refs.[93, 94, 96–100] (see Table4.1) using Eq. (4.6) and the $B_0(T)$ used in this work.

low hydrostatic pressures, which is not necessarily the case for some of the references. Our assumption allows us to use the simple expression:

$$\left.\frac{\partial E_g}{\partial P}\right|_{P=0} = -\frac{1}{B_0(T)}\,(a_c - a_v)\,, \tag{4.6}$$

from Eq. (4.3).

By using the procedure described above, we determined the deformation potential in CdTe, represented by the black symbol in Fig. 4.11, using the low-temperature data of Dunstan *et al.* [1]. We have assumed that the deformation potential linearly varies with Cd concentration [101], which allows us to determine the deformation potential at 2K in $Hg_{1-x}Cd_xTe$ for any value of

x. Additionally, the red symbols in Fig.4.11 represent the values of $a_c - a_v$ at 300 K, which were recalculated from the results of Latussek *et al.*[101] using the current values of $B_0(T)$ and B_0' used in this work. The linear fit of the deformation potential as a function of x gives $a_c - a_v \simeq -2.815 - 0.237x$ at 2 K, while the same procedure based on the results of Latussek *et al.*[101] results in $a_c - a_v \simeq -3.675 + 0.208x$ at 300 K.

From the figure, it is clear that there is a difference between the low and room temperature deformation potentials, indicating that $a_c - a_v$ in $Hg_{1-x}Cd_xTe$ is temperature dependent. The reason for this temperature dependence is not yet understood. It is likely that it is caused by the unique electron-phonon coupling present in $Hg_{1-x}Cd_xTe$ alloys. This specific coupling results in a significant temperature variation of the band-gap $E_g^{(0)}(T)$ at any Cd concentration x [76] and should also lead to a temperature dependence of hydrostatic deformation potentials.

4.6 Summary

In this chapter, the results and analysis of THz magneto-optical spectroscopy of $Hg_{1-x}Cd_xTe$ films under hydrostatic pressure were presented. The samples chosen for the measurements were close to critical values of x in order to enable the topological phase transition from semimetal to semiconductor. The energies of the observed interband LLs transitions were analyzed as a function of magnetic field using a simplified Kane model. In the semirelativistic approach, this model is characterized by two free parameters: the rest mass and velocity of the Kane fermions. These parameters were extracted at various hydrostatic pressures, allowing for the determination of the hydrostatic deformation potentials $a_c - a_v$ at a cryogenic temperature of 4 K. This avoided the need for band structure calculations, which are required for HgTe/HgCdTe superlattices. The measurements allowed for the investigation of both negative and positive band gap values, corresponding to semi-metallic and semiconductor films, respectively. By using linear extrapolation between the obtained values and those reported by Dunstan *et al.* [1] for CdTe at 2 K, the deformation potential $a_c - a_v$ at low temperatures for any value of x was obtained.

5 Towards the topological phase transition of $(Cd_{1-x}Zn_x)_3As_2$: from Dirac semimetal to trivial semiconductor

Contents

5.1 Introduction 69
5.2 (Cd_3As_2) doped with Zn 73
5.3 Sample preparation description 75
5.4 Results 76
5.4.1 Magneto-reflectivity 76
5.5 Summary 84

The findings presented in this chapter are being prepared as a manuscript titled 'Towards the topological phase transition of $(Cd_{1-x}Zn_x)_3As_2$: from Dirac semimetal to trivial semiconductor'.

5.1 Introduction

The main focus of this chapter is to explore the expected topological quantum phase transition in $(Cd_{1-x}Zn_x)_3As_2$ by tuning the Zn content. To achieve this, I will investigate the electronic properties of $(Cd_{1-x}Zn_x)_3As_2$ using tools of

magneto-optics. By gaining a deeper understanding of the topological properties and phase transitions in $(Cd_{1-x}Zn_x)_3As_2$, we can further our knowledge of topological quantum materials and potentially contribute to their practical applications in fields such as quantum computing and spintronics.

Chemical doping of Zn is a convenient way of reducing the electron density of Cd_3As_2 [110] and also lifting up the band inversion, which finally induces a topological phase transitions from a Dirac semimetal to a trivial semiconductor. This system, which utilizes chemical doping for control, enables investigations of the topological quantum phase transition of 3D Dirac electrons and can be continuously fine-tuned [111]. Previously this kind of band inversion transition originating from the change of the spin orbital coupling, was observed in solid solutions of semimetals and semiconductors, like it was in the case of $Hg_{1-x}Cd_xTe$, as discussed in the previous chapter.

The band structure calculations of cadmium (Cd_3As_2), among many proposed reports, indicate the presence of a pair of 3D Dirac cones protected by symmetry, indicating the presence of 3D massless Dirac electrons in the system [112, 113]. These particles are described by Dirac equation for particles with a vanishing rest mass, which implies a double degenerated (due to the spin) conical bands [114]. The reported 3D Dirac cones were observed not only via theoretical predictions, but also through angle-resolved photoemission spectroscopy (ARPES) (fig. 5.1) [111, 115]. However, this is not the only approach to the topic.

Bodnar [116] presented the simplified model describing the complex structure of Cd_3As_2. The initial method utilized in this approach was to consider this material as a typical narrow-gap Kane semiconductor-semimetal with a near-zero band-gap. In this approximation, similarly to gapless HgCdTe, the band structure of Cd_3As_2 exhibits, centered around Γ point, a widely extended conical band. The appearance of this not protected cone is due to the degeneracy of p- and s-like states of arsenic, and cadmium, respectively. What is also revealed in this material, within the scope of Bodnar model, are the symmetry

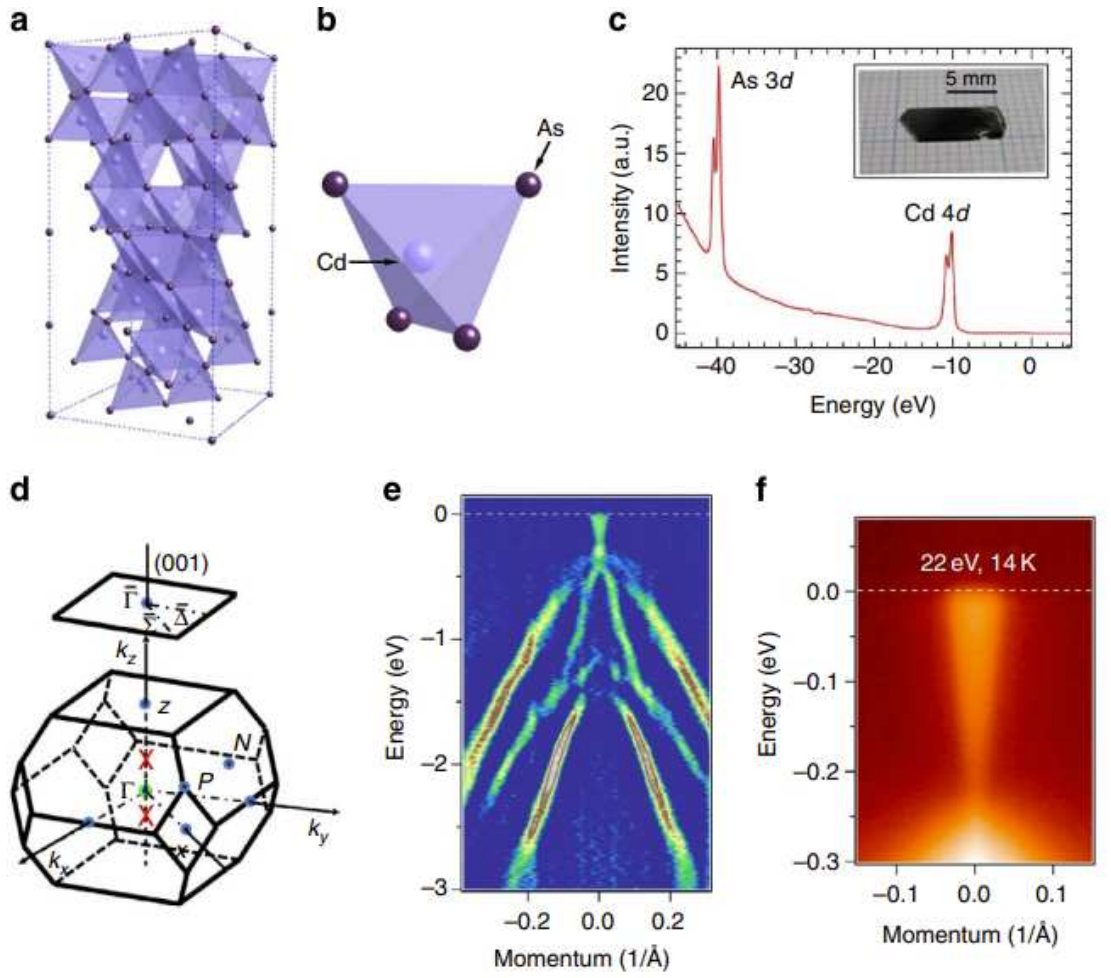


Figure 5.1: (a) The crystallography structure of Cd_3As_2. (b) The unit cell structure. (c) The core-level spectroscopy results. (d) Brillouin zone with the projected surface along the (001)-direction. (e) The second derivative of ARPES measurements. (f) ARPES near the Fermi level. Adapted from [115], with the permission of publisher.

protected Dirac cones. They are highly anisotropic and strongly tilted cones which appear at low energies within the proximity of the crossing points of two arsenic-like p-type bands. Said crossing points are created when the cubic symmetry of Kane semimetal/semiconductor is reduced to a tetragonal symmetry. This is the case of Cd_3As_2. The lowering of the symmetry can be quantized in a form of crystal field splitting (δ), which is a parameter describing the energy separation between two p-type bands at $k = 0$, which is measuring the direct energy scale of Dirac electrons.

Landau level spectroscopy [112] revealed the energy scale of 3D Dirac elec-

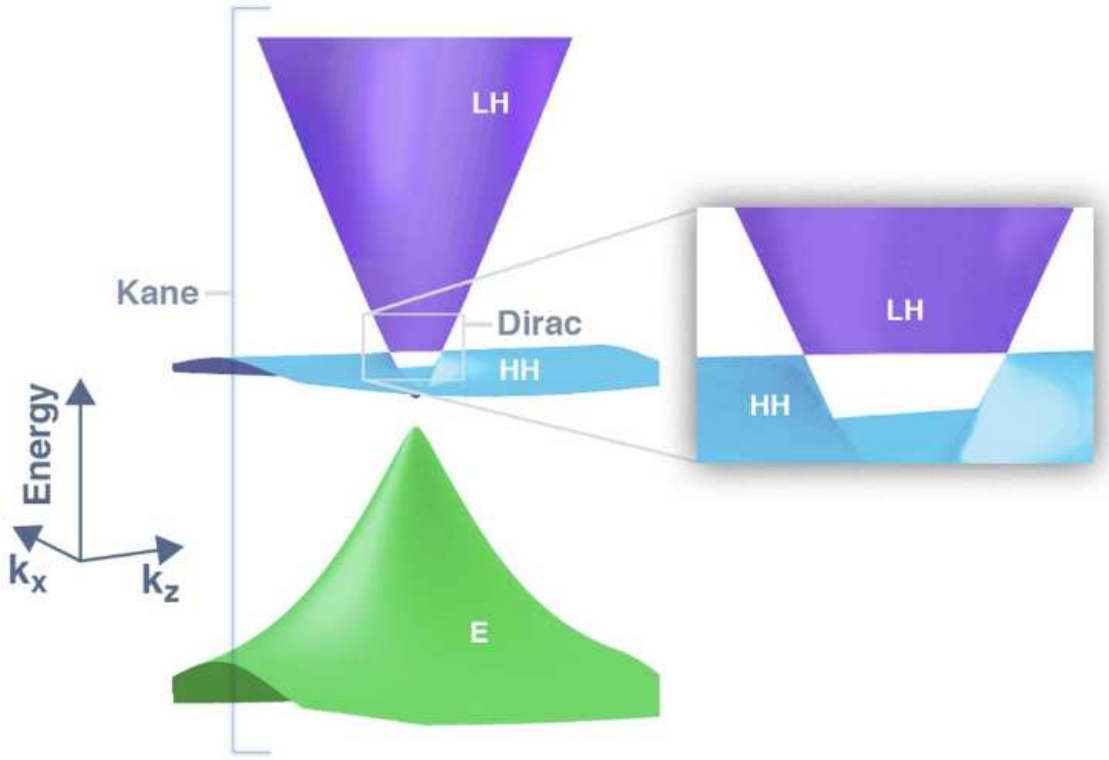


Figure 5.2: A diagram illustrating the electronic bands in Cd_3As_2 at the center of the Brillouin zone. The bands form two types of three-dimensional conical structures: a single cone containing Kane electrons at a higher energy scale, caused by the absence of a band gap, and two highly tilted and anisotropic 3D Dirac cones at lower energies. Adapted from [112], with the permission of publisher.

trons in the Cd_3As_2. Initially what brought the attention to the cadmium arsenide was its high mobility of electrons (over 10^4 cm^2/Vs at room temperature) [114]. Additionally the compouns is stable under ambient conditions [112]. Moreover it shows evidence of quantum Hall effect after thinning down, strong linear magneto-resistance and anomalous Nernst effect [114].

Cadmium arsenide may host 3D symmetry protected Dirac electrons, at the energy scale which does not exceed several dozens of meV. As is shown in fig. 5.2, where Dirac cones can be observed in the close proximity of the crossing points of $p-$type bands. For energies higher than δ cadmium arsenide can be described as a Kane semimetal, which is characterized by an inverted gap.

The claim of co-existing Kane and Dirac systems within cadmium arsenide, can be further supported by report of magneto-optical spectroscopy which presents specific cyclotron resonance absorption within the quantum limit,

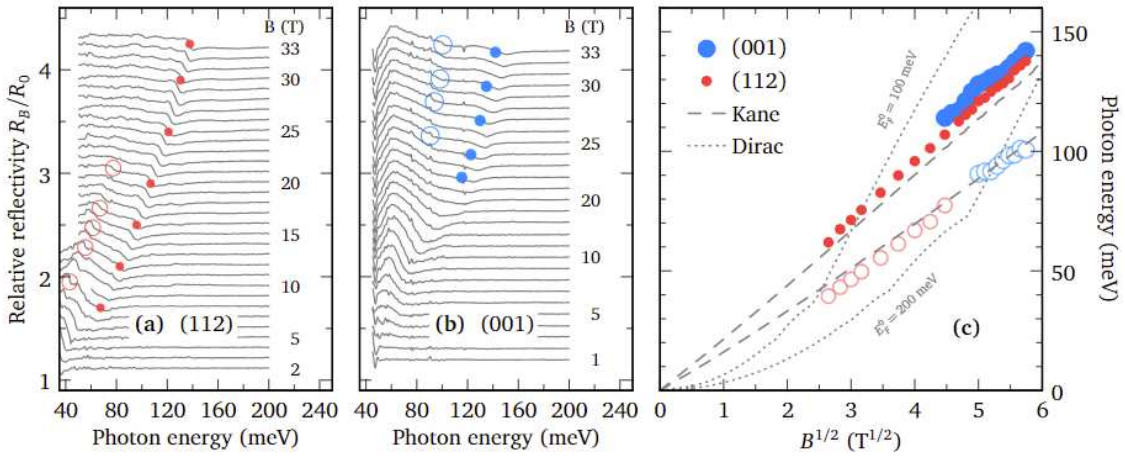


Figure 5.3: Relative magneto-reflectivity of two samples with different orientation - (112) and (001) - (a) and (b), respectively. The full and open points indicate the positions of observed dominant and weak cyclotron resonance modes, respectively. (c) Plots the extracted points as a function of square root of B, alongside theoretical curves for Dirac and gapless Kane model, respectively. Adapted from [117], with the permission of publisher.

which implies probing of the Kane electrons (fig. 5.3) [117]. It is worth mentioning that this claims go in line with STM/STS data [118], and against ARPES studies [119, 120].

5.2 (Cd_3As_2) doped with Zn

Previously $(Cd_{1-x}Zn_x)_3As_2$ was studied in transport measurements [110, 111]. Fig. 5.4 presents the phase diagram of $(Cd_{1-x}Zn_x)_3As_2$. Relying on the analysis of electrical properties authors show a transition from a 3D Dirac semimetal to a semiconductor. What is important to note is that authors suggest the critical value of the Zn $x_c \sim 0.38$, based on the results of the experiments. With the estimation that the band-gap changes linearly with respect to the x , the estimated critical point of the band inversion transition falls in the range of $0.23 \leq x \leq 0.41$. Next estimation which authors propose is established while considering the change of spin-orbital coupling strength. In this context the authors make an assumption that the band inversion can occur only due to the variations in the strength of the SOC, which is directly proportional to Z^4/n^3. This relationship holds true for hydrogenic wavefunctions in a Coulomb field,

where Z represents the nuclear charge and n denotes the principal quantum number. With this estimation the critical point $x_c \sim 0.35$, falling close to the values obtained from the experiments [111].

Fig. 5.5 presents the results of article where the authors show carrier density controlled both by the chemical doping and electrostatic gating in a transistor configuration. This is due to the investigation of quantum transport at various Fermi-level positions. Let us note that panel (d) depicts the topological phase transition to occur at $x_c \sim 0.17$ [110], which is in a discrepancy in comparison to the results presented in previously described article [111].

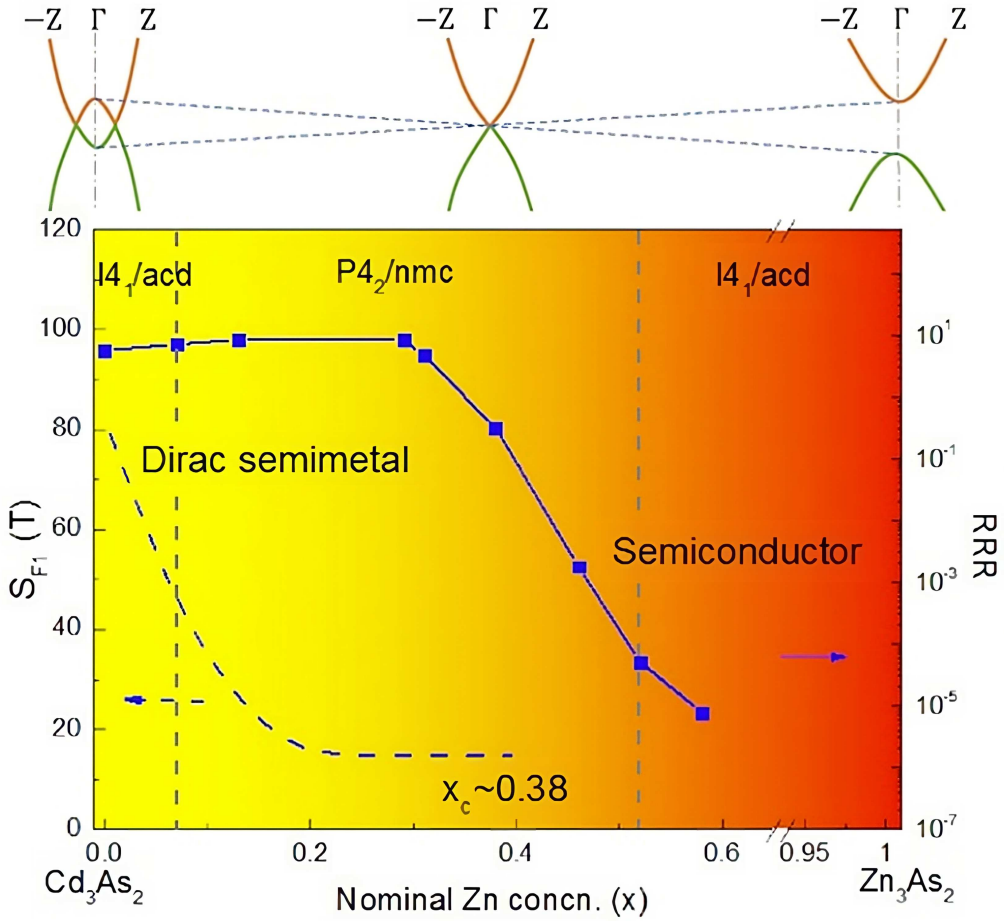


Figure 5.4: Phase diagram of $(Cd_{1-x}Zn_x)_3As_2$. As the concentration of Zn increases, the $(Cd_{1-x}Zn_x)_3As_2$ undergoes a phase transition from a topological Dirac semimetal to a semiconductor. The background color in the diagram represents the gradual change of resistivity at 2 K as x increases. Adapted from [111].

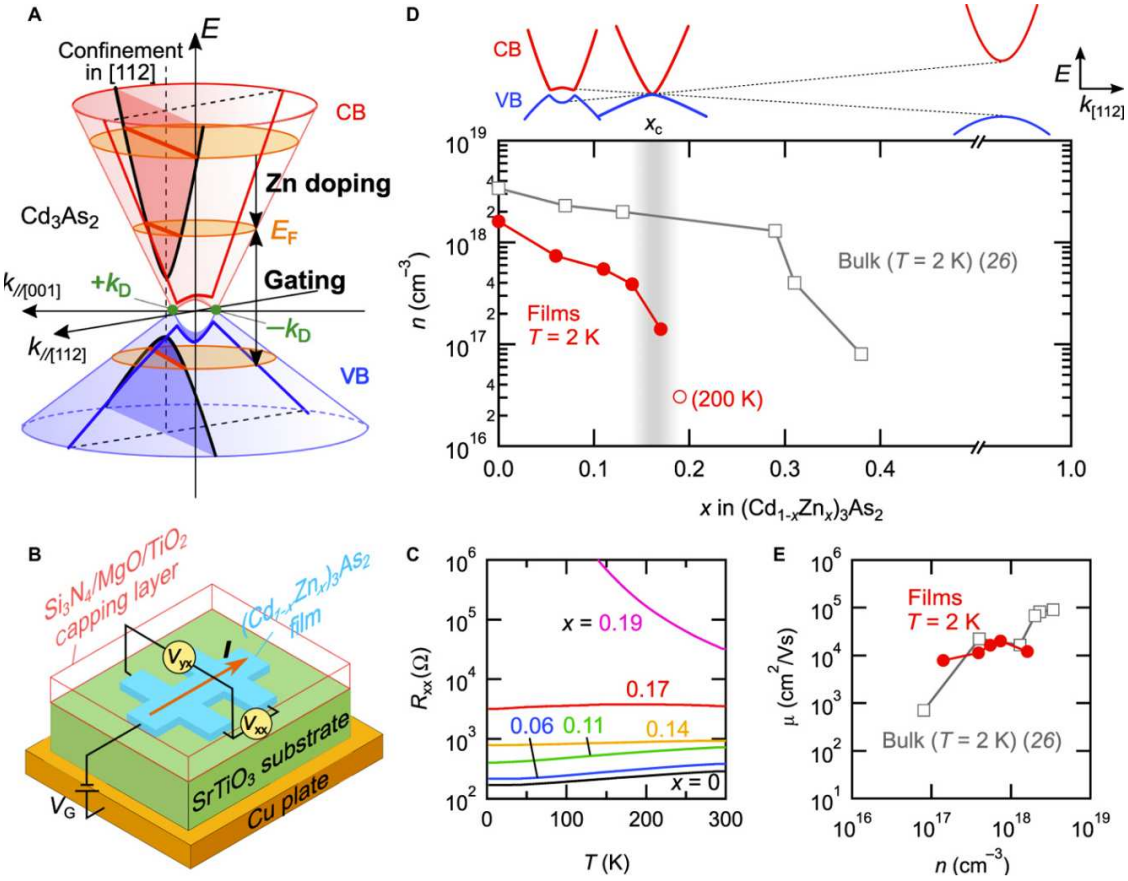


Figure 5.5: The control of carriers in $(Cd_{1-x}Zn_x)_3As_2$ by the means of Zn doping and gating. (a) Band structure of $(Cd_{1-x}Zn_x)_3As_2$. (b) Scheme of the sample with back gate made from $SrTiO_3$. (c) Resistance versus temperature dependence for various concentrations of Zn (x). (d) Electron density as a function of Zn content x, with a comparison of thin samples versus bulk crystals. (e) Mobility as a function of electron density. Adapted from [110].

5.3 Sample preparation description

Chemical vapor deposition techniques were used to fabricate single crystals of Cd_3As_2-Zn_3As_2 solid solutions. A mixture of pre-synthesized polycrystalline Cd_3As_2 and Zn_3As_2 was used as the source material for crystal fabrication. For the synthesis of initial Cd_3As_2 and Zn_3As_2, Zn (99,999), Cd (99,999), and As (99,9999) were used. The synthesis of Cd_3As_2 and Zn_3As_2 involved direct fusion of Zn, Cd, and As in a stoichiometric ratio at temperatures above the melting points of these compounds, followed by sublimation in vacuum for homogenization. All routines were carried out in sealed quartz ampoules.

The crystal growth process was also carried out in sealed quartz ampoules of approximately 20-24 mm in diameter and 200-250 mm in length, in a furnace with two temperature zones. The temperature in the source zone ranged from 550-600°C, while in the deposition zone it ranged from 500-550°C. The source mixture Cd_3As_2 and Zn_3As_2 had a ratio of 50/50 (usually 10/10 grams), and after 1-2 weeks, crystals of solid solutions grew in the low temperature part of the ampoule. During crystal growth, crystals with different compositions of solid solutions were formed. The real single crystals' composition was determined using EDAX analysis. The relationships between the temperatures of the zones, the Cd_3As_2/Zn_3As_2 ratio in the source mixture, and the compositions of the final crystals were not studied.

5.4 Results

The magneto-optical spectroscopy was used in order to probe the band structure of the system. In total 8 facets between 6 samples were measured using the tools of magneto-optics, in this case magneto-reflectivity.

5.4.1 Magneto-reflectivity

All of the experiments were performed in the Faraday configuration. The measurements results were normalized by the response at the magnetic field $B = 0$ T to further visualize the changes induced by the magnetic field. Fig. 5.6 presents the results of relative magneto-reflectivity measurements. The bottom panel shows the first derivative of the results. What can be observed is the lack of LL-transitions in higher energy limit for the sample with Zn content $x = 14\%$.

For the analysis 5 samples of the same crystallography orientation (112) were chosen, for the unification of analysis process. The points extracted from the measurements are plotted in fig. 5.7, with the bottom panel presenting the relative magneto-reflectivity plotted as a function of $\sqrt{B}$.

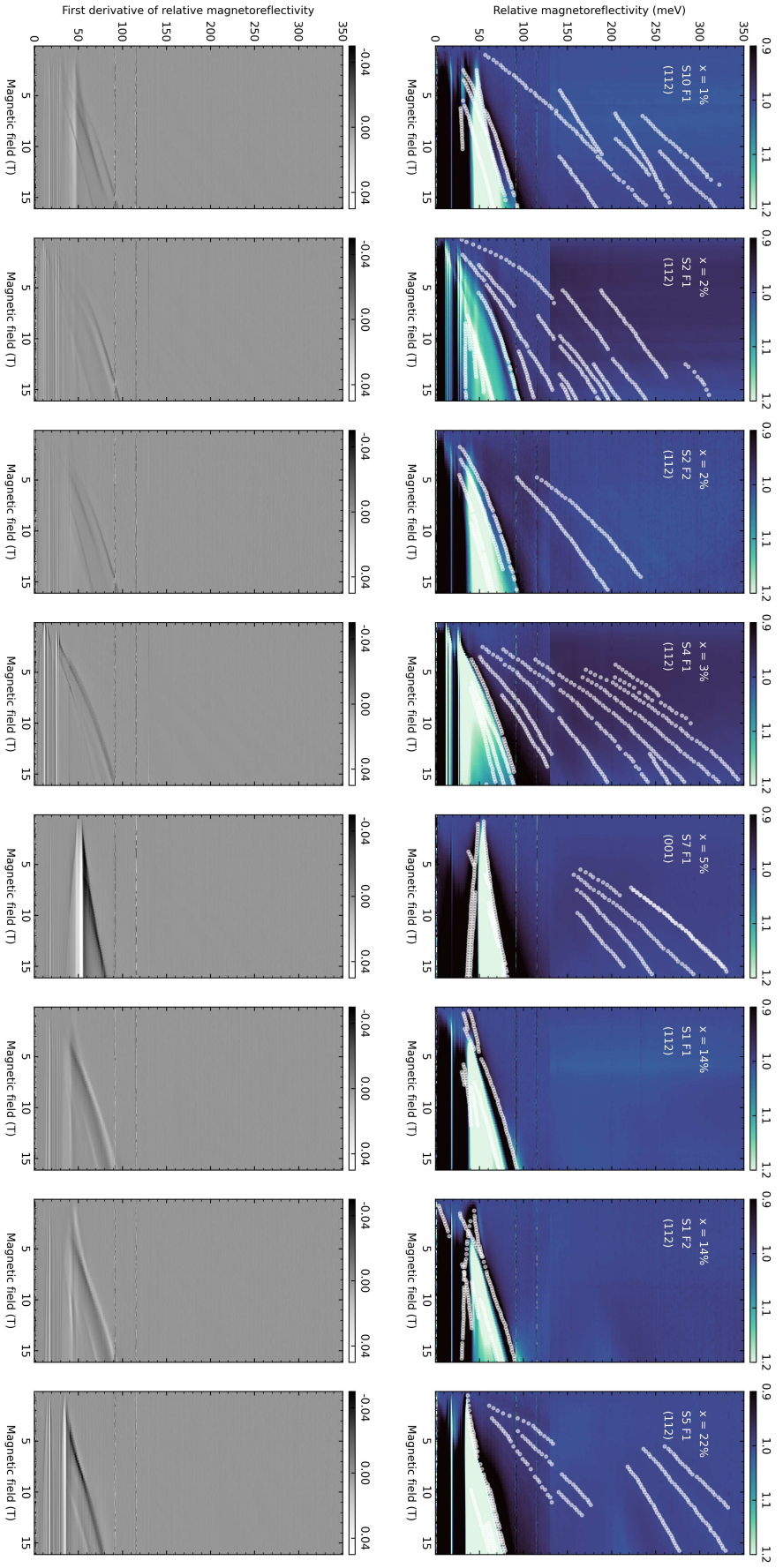


Figure 5.6: Results of relative magneto-reflectivity and its first derivative.

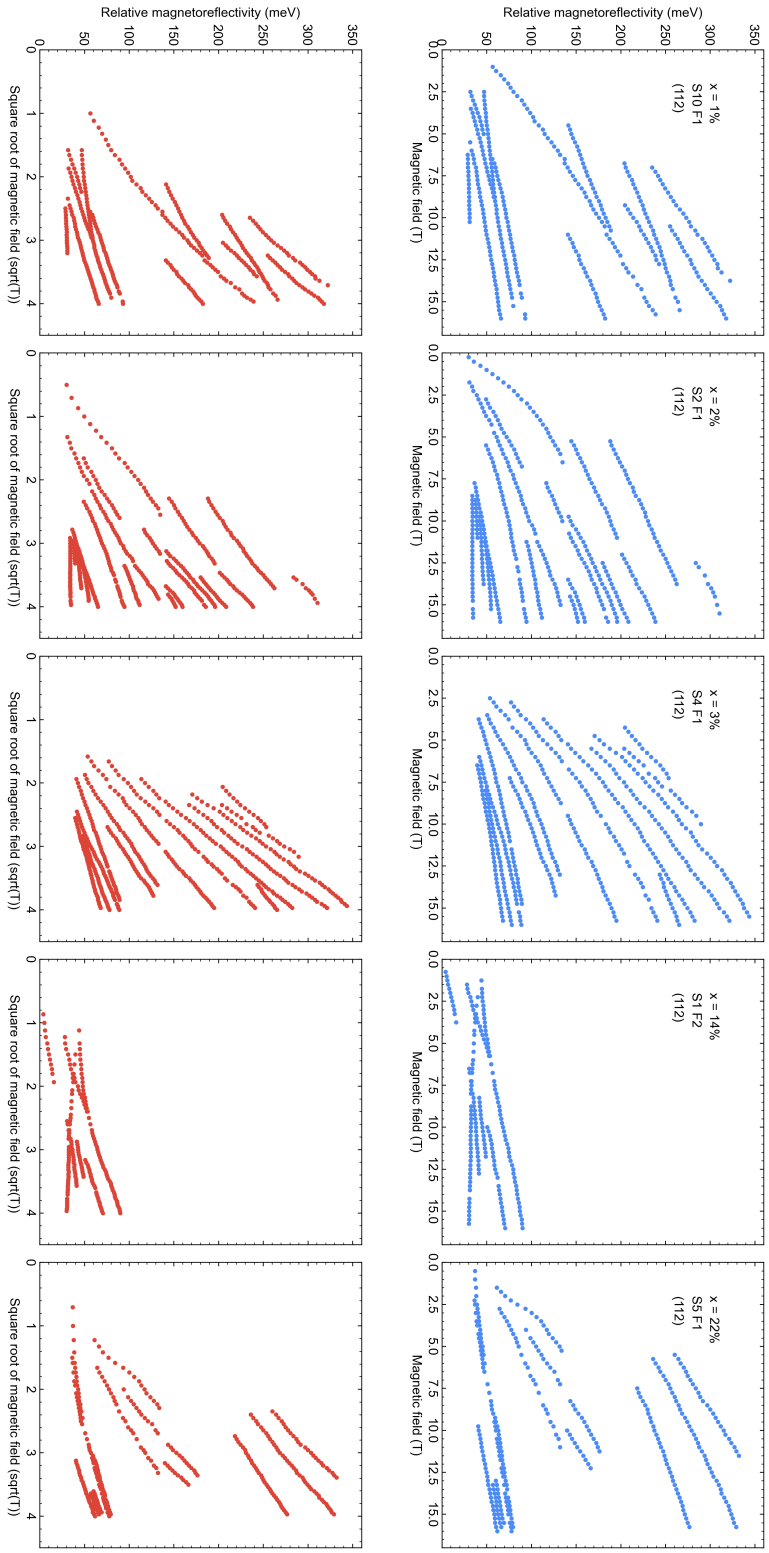


Figure 5.7: Results of relative magneto-reflectivity of (112) facets. Top panel: Landau level transitions as a function of magnetic field. Bottom panel: Landau level transitions as a function of $\sqrt{B}$.

The presence of free charge carriers within a 3D solid is demonstrated by the plasma edge in the reflectance spectrum. When electrons undergo cyclotron motion in a magnetic field with a defined cyclotron frequency $\omega_c = eB/m$, the response of the system in the magneto-optical regime changes. This is observed when the system is probed with radiation of opposite circular polarizations, resulting in two modes of light: cyclotron resonance active (CRA) and inactive (CRI). The CRA has the same sense of rotation as electrons, causing the position of the plasma edge to increase with B, whereas the CRI has the opposite sense of rotation and causes the position of the plasma edge to decrease with B.

From the standard magneto-plasma theory [121] it is known that the plasma edge divides into two branches that are spaced apart by the cyclotron energy:

$$E_c = \hbar\omega_c = \frac{eB}{m}. \tag{5.1}$$

Some of the measured samples (1 %, 14 % and 22 % of Zn content) exhibit field-induced splitting of the plasma edge, as was previously observed by Akrap et. al [117].

As known from literature the cadmium vacancies are annealing with time at room temperature [122, 123]. This process is found to be contributing to the plasma edge progression with time [123]. It was found that with a several month difference in measurements the plasma edge was found almost 15 meV lower. This corresponds to a loss of around 50% of carriers. In result it has to be noted that the low-energy properties of the Cd_3As_2 are changing in time, this can be also expected of the $(Cd_{1-x}Zn_x)_3As_2$ samples.

Plasma edge splitting

The splitting of the plasma edge is estimated to be $\sim$ 2.5 meV/T, $\sim$ 3.75 meV/T and $\sim$ 2.7 meV/T for samples with 1 %, 14 % and 22 % of Zn content, respectively. It is important to note this is just a rough estimate, due to large overlap

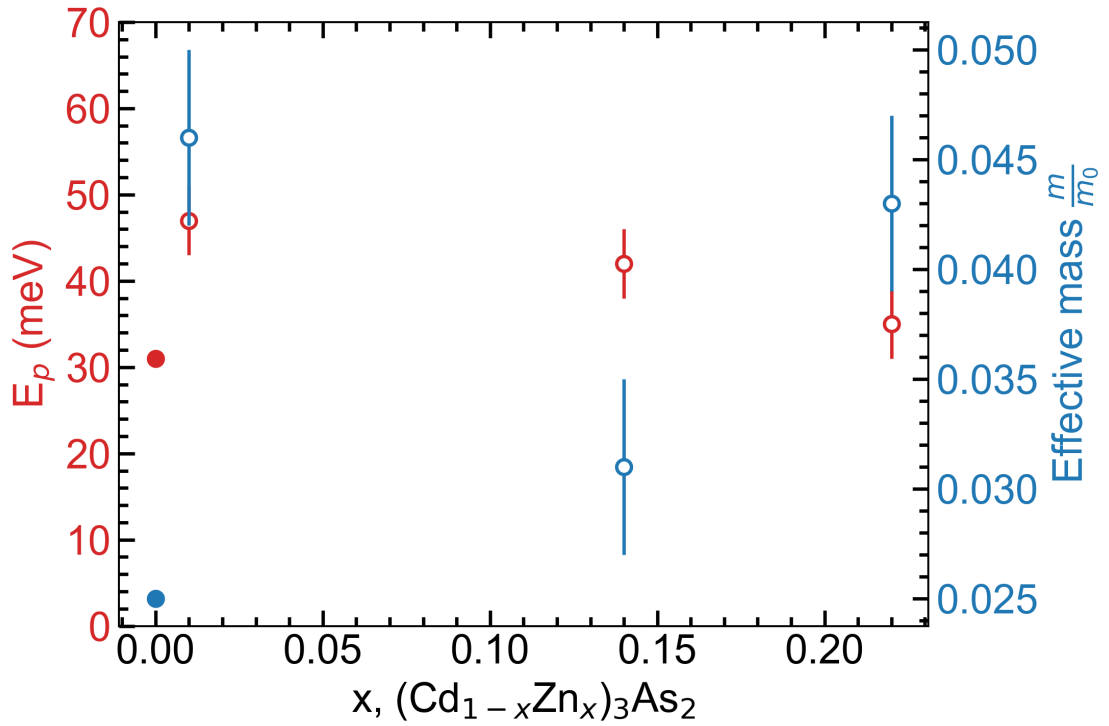


Figure 5.8: Energy of the plasma edge splitting at $B = 0$ T and effective mass, calculated from the cyclotron energy, as a function of Zn content. Hollow points are obtained from our results, while solid points are from Akrap et. al [117].

with phonons and inter-LL transitions, which make it harder to establish the correct values.

Then from the estimation of the spacing of the plasma edge splitting, we obtain following values of effective mass of the carriers: $m_{1\%} = 0.046m_0$, $m_{14\%} = 0.031m_0$, $m_{22\%} = 0.043m_0$.

Figure 5.8 presents the dependency of the energy of plasma edge splitting (E_p) at $B = 0$ T and effective mass ($\frac{m}{m_0}$) as a function of Zn content. Comparing our results (hollow points) with the ones from the literature (solid points) [117] we see that the Cd_3As_2/Zn_3As_2 samples have a comparable value of the effective mass to the values of effective mass of the Cd_3As_2. Similarly the values of the energy of plasma edge splitting (E_p) has similar order of magnitude to the ones from the literature [117].

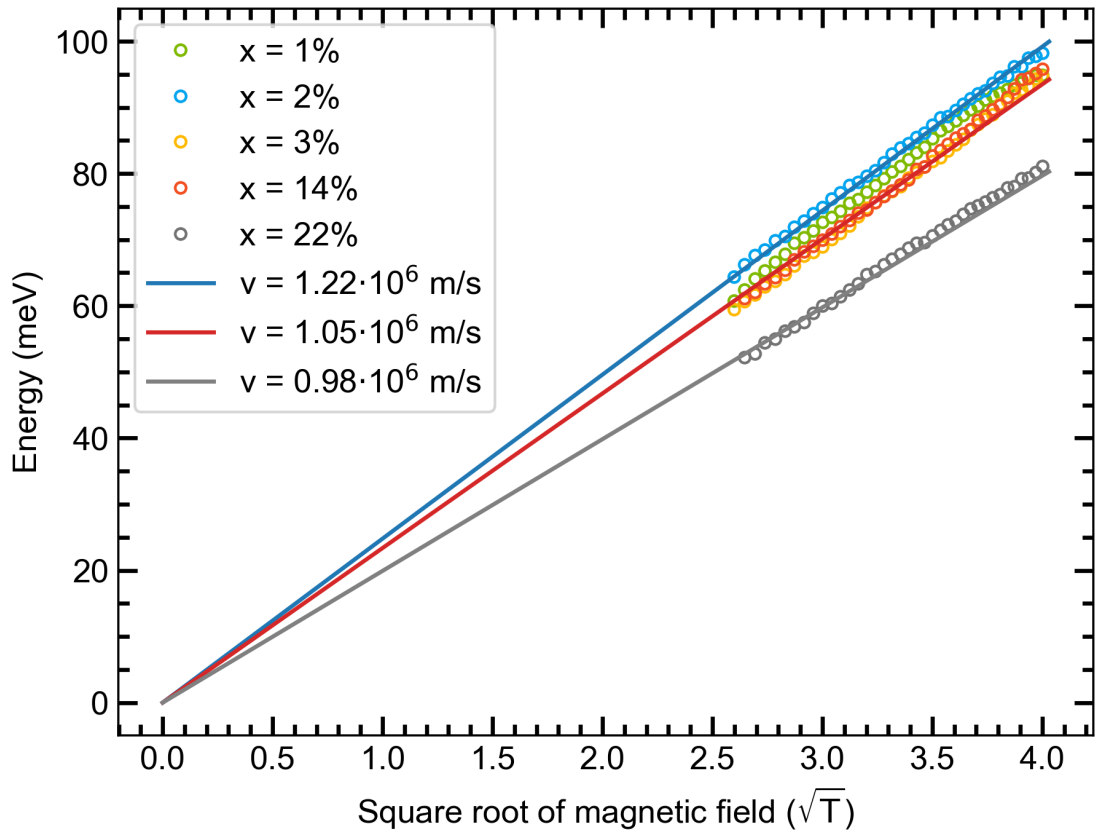


Figure 5.9: Hollow points indicate the position of cyclotron resonance for samples with different Zn concentrations. The solid lines indicate the fitted simplified Kane model for various velocity of carriers.

Cyclotron resonance analysis

In the further analysis I extracted the positions of observed cyclotron resonances (CR) in each of the samples . The results are plotted in fig. 5.9 as a function of square root of magnetic field. Hollow points are the positions of CR for each of the measured samples, what is worth to notice is that the CR for sample with 22% of Zn content lays separately from the low Zn content samples.

The solid lines are fitted CR transitions via simplified Kane model for various velocities of the carriers. For this fitting only transitions from $n = 1$ to $n = 2$ with spin down in the conduction band were chosen. The velocity of the carriers varies from $v = 0.98 \cdot 10^6$ m/s to $v = 1.22 \cdot 10^6$ m/s. From the literature the velocity of carriers in Cd_3As_2 is established as $v_L = 0.93 \cdot 10^6$ m/s[117]. Although our

carrier velocity is relatively high, it remains within an acceptable range of agreements with literature.

We have to note that within the available literature we have not found the value of carrier velocity for Zn_3As_2 in the regime of simplified Kane model. Our results indicate that the velocity of $(Cd_{1-x}Zn_x)_3As_2$ carriers change with the Zn content, which could imply that the velocity of carriers of Zn_3As_2 is indeed different than the one of Cd_3As_2.

From the fitted values of velocity of the carriers one can obtain the value of Kane parameter E_{Kane} (in the literature one can find the name E_p, instead). E_{Kane} is a parameter related to the matrix element of the Bloch function of p- and s-type bands. The values for $(Cd_{1-x}Zn_x)_3As_2$ are $E_{Kane_1} = 25.42$ eV, $E_{Kane_2} = 22.59$ eV and $E_{Kane_3} = 16.40$ eV, for $v = 1.22 \cdot 10^6$ m/s, $v = 1.05 \cdot 10^6$ m/s and $v = 0.98 \cdot 10^6$ m/s, respectively.

Band-gap evolution

The fig. 5.7 was used for the extraction of values of band-gap for each of the analyzed samples. To do so the linear in $\sqrt{B}$ high energy optical transitions were used. The resulted values were plotted in fig. 5.10 alongside band-gap values for Cd_3As_2 and Zn_3As_2 known from literature [117, 122, 124]. It has to be noted that the exprimentally obtained value of band-gap is equal to 1110 meV [124]. While in [122] it is shown that the low temperature band-gap of Zn_3As_2 is equal to 820-1100 meV. Further investigation is needed to determine the exact nature of this discrepancy and its possible implications for future research of this area.

From the extrapolation of our results it appears that the topological phase transition would likely occur at around 5% of Zn concentration. As such, our results for 22% of Zn suggest that the material already behaves like a normal semiconductor. Conversely, our results for lower Zn concentrations all fall within the regime of an inverted band structure of semimetal. However, some difficulties were encountered with the analysis of the 14% of Zn concentration,

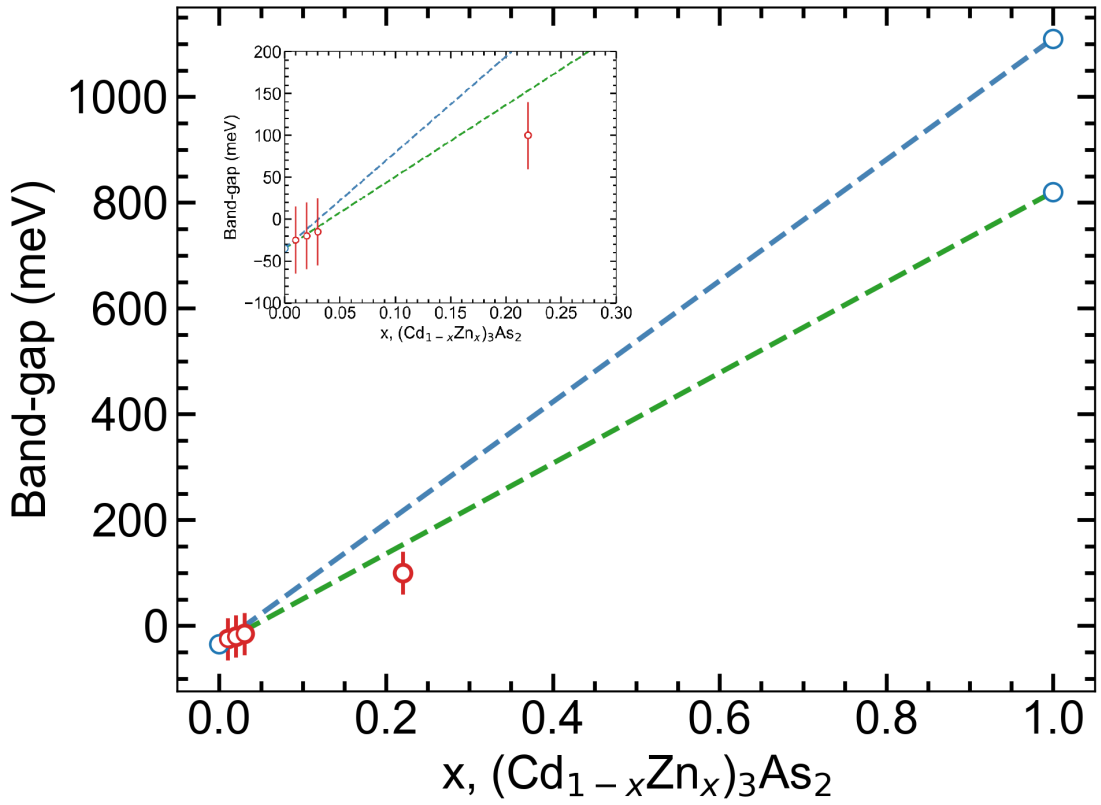


Figure 5.10: Red points are obtained from our results, while blue points are from literature for Cd_3As_2 and Zn_3As_2 [117, 122, 124]. Blue line connect the highest values from literature of the Zn_3As_2 band-gap value [124], the green line represent the lowest value of Zn_3As_2 band-gap value [122].

as I was unable to extract the band-gap value due to the lack of high energy transitions. At the moment we are unable to determine why is that so. Although we are not convinced it could origin due to the close proximity of the topological phase transitions.

5.5 Summary

In this chapter, my main focus is on investigating the electronic properties of $(Cd_{1-x}Zn_x)_3As_2$, which is a material that is expected to undergo a topological quantum phase transition as the Zn content is varied. To achieve this, I use magneto-optics - a powerful tool that allows for the measurement of the material's optical response in the presence of a magnetic field. The ultimate goal of my research is to gain a deeper understanding of the topological properties and phase transitions in $(Cd_{1-x}Zn_x)_3As_2$.

I begin by measuring the magneto-reflectivity of samples with varying Zn content, ranging from 1 to 22%. The magneto-reflectivity measurements allow me to identify various features in the material's optical response that are related to its electronic properties. One important feature that I observe in the magneto-reflectivity spectra is cyclotron resonance. Another feature that I observe is plasma edge splitting. This feature is also sensitive to the material's electronic properties and can provide insights into its topological properties. Finally, I investigate the evolution of the material's band-gap as the Zn content is varied. My study shows that the band-gap of $(Cd_{1-x}Zn_x)_3As_2$ changes systematically with the Zn content, which is consistent with the expected behavior of a topological quantum phase transition.

It appears that I have successfully probed the band structure on either side of the topological phase transition, albeit confirmation is still pending.

Furthermore, in the future research, studying general solution for Bodnar model in magnetic field could provide, a more comprehensive understanding of the magneto-optical behavior of $(Cd_{1-x}Zn_x)_3As_2$.

6 Magneto-reflectivity of Weyl semimetal $Nb_{1-x}Ta_xAs$

Contents

6.1 Introduction 85
6.2 Transition-metal monopnictides as examples of Weyl type-I semimetals 87
6.3 Modelling the band structure in the vicinity of Weyl 1 cones . 90
6.4 Sample description 94
6.5 Experimental details and results 94
6.6 Modelled response of magneto-reflectivity 95
6.7 Summary 97

The findings presented in this chapter have been prepared as a manuscript titled 'Tunable Weyl Cone Distribution and Unusual Down-Dispersing Lines in NbAs and $Nb_{1-x}Ta_xAs$ Investigated by Magneto-Optics' and are currently undergoing the publication process.

6.1 Introduction

NbAs and TaAs are some of the leading representatives of Weyl semimetal group and have been extensively studied for their Weyl semimetal behavior.

In my study I'm turning towards ternary compound $Nb_{1-x}Ta_xAs$ to investigate whether it also exhibits Weyl semimetal properties.

Weyl nodes, of Weyls semimetals, act as monopoles of Berry curvature in momentum space and can only be present in pairs of opposite chirality [125]. These Weyl points are responsible for a variety of unusual electronic phenomena, such as chiral anomaly and topological surface states. The band structure in their closest vicinity can be effectively described using the Weyl equation, which predicted the existence of massless fermions with a definite chirality (handedness) [126]. The existence of Weyl nodes in the close proximity of E_F gives rise to the Fermi arcs on the surface and chiral anomaly inside the bulk structure [127–129]. The experimental discovery of Weyl fermions has re-awaken the interest of the physical society in Weyl fermions which were previously only discovered in experiments of high-energy physics [35].

First classification of the Weyl semimetals can be obtained through the respect to the symmetry which they posses. When the time reversal symmetry is broken, then the minimal number of Weyl nodes is two [130]. When the inversion symmetry is preserved, it ensures that the Weyl nodes can be found at $\pm\mathbf{k}$ at the same energy, which assures the same vicinity to the Fermi level of the both cones. In a situation when the space inversion symmetry is broken four Weyl nodes emerge, as a consequence of the time reversal symmetry preservation. In this case each Weyl cone at $\mathbf{k}$ is directly transformed into a Weyl cone with the same chirality at -$\mathbf{k}$. This system is at least fourfold degenerated so the total chirality of the Weyl cones has to be equal to zero [131]. In a situation when both time reversal and inversion symmetry is broken the Weyl cones are expected to appear at different energies, with the preservation of the topological properties of Weyl semimetals.

Further classification occurs for the Weyl semimetals with the broken space inversion symmetry with respect to the tilt of the Weyl cones. In this case we divide Weyl semimetals into two types: type-I and type-II (as presented in fig. 6.1) based on the tilt conditions of the conical dispersion[132]. Type-I contains

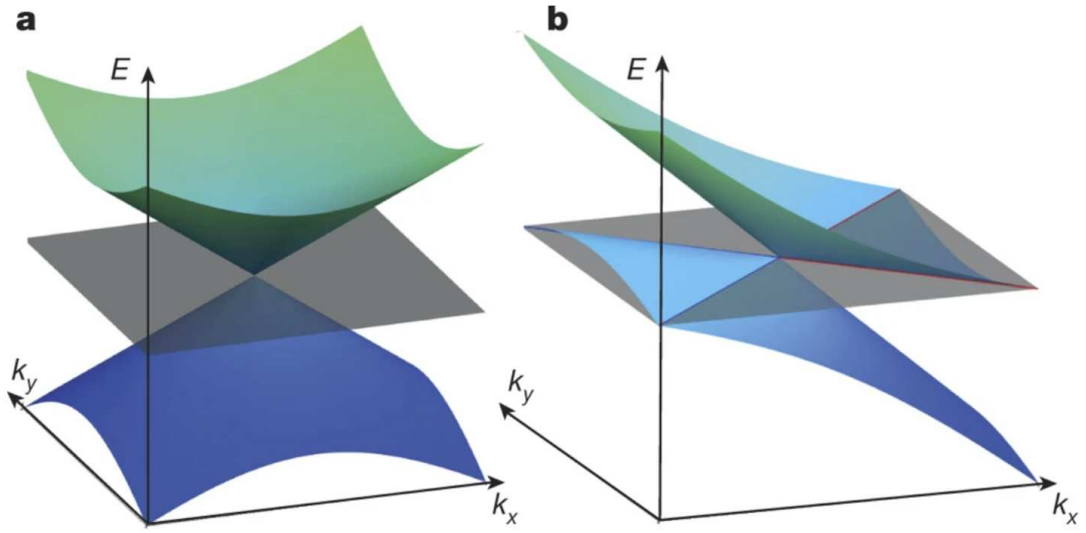


Figure 6.1: (a) Type I Weyl semimetal. (b) Type II Weyl semimetal. The gray surface presents the position of Fermi level. Adapted from: [132], with the permission of publisher.

of Weyl semimetals where the tilt which is described by parameter w is smaller than the asymptotic velocity v [133]. In this case the Fermi surfaces of Weyl cones are closed (fig. 6.1 (a)), like for example in TaAs. In the type-II we observe over-tilted Weyl cones due to the parameter w being bigger than the parameter v. In such case the Fermi surfaces are over and we distinguish separate electron and hole parts (fig. 6.1 (b)). This situation can be observed for example in the group of transition-metal dichalcogenides which includes $MoTe_2$ [22].

6.2 Transition-metal monopnictides as examples of Weyl type-I semimetals

NbP, TaP, NbAs and TaAs are one of the most known representatives of the type-I Weyl semimetals (fig. 6.2 presents their crystal structure) [134–136]. They exhibit large transverse magneto-resistance and ultra-high mobility [137]. Here we show for the first time results obtained on the combination of the two different systems (NbAs and TaAs) - $Nb_{1-x}Ta_xAs$. According to magneto-optics, DFT and ARPES results of both systems differ from each other in the cone

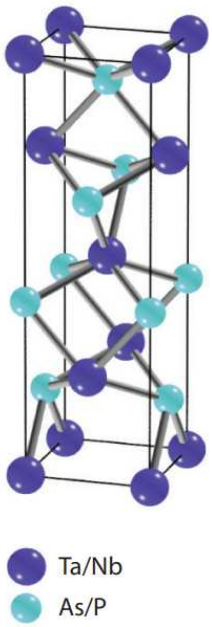


Figure 6.2: Non-centrosymmetric crystal structure. Adapted from: [24], with the permission of publisher.

distribution and energy scale [138]. Hence it is vital to explore their behavior when combined in a single sample.

In these materials we distinguish 24 Weyl cones (fig. 6.3) which can be further categorized into two groups:

1. Weyl 1 - with four pairs of Weyl 1 cones which can be found in the proximity of the high-symmetry point Σ, within the $k_z = 0$ plane. These cones exhibit nearly isotropic behavior in the k_x-k_y plane, whereas their dispersion is relatively uniform along the k_z axis.

2. Weyl 2 - with eight pairs of Weyl 2 cones which can be found in the proximity of the path between the Γ− S symmetry points, within the $k_z = \pm 0.5\,|\Gamma - Z|$ plane. These cones are nearly isotropic in the 3D reciprocal space. The separation of the cone is greater in relation to Weyl 1.

The transport measurements on Weyl semimetals supply us with crucial information about Fermi velocities and E_F but are limited to only these information. On the other hand, it is the magneto-optical measurements that

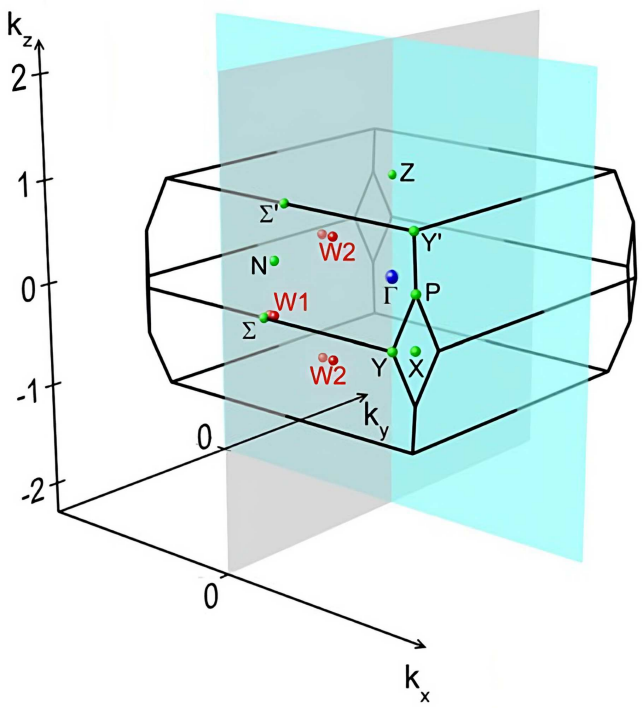


Figure 6.3: Brillouin zone with examples of pairs of Weyl points. Adapted from: [139].

can provide us with information about Landau quantization or selection rules [140]. In some cases this even leads to the revelation of new types of transitions following different selection rules $(n+2)$ than the typical dipolar ones $(n+1)$ [129, 140]. Magneto-optics is therefore a powerful tool, which can be utilized to gain insight into how this material responds to magnetic field.

6.3 Modelling the band structure in the vicinity of Weyl 1 cones

To study the bulk band structure of Weyl semimetals, we used the same approach as in Polatkan *et. al* ([141]) and J. Wyzula's thesis [142].

To describe the Landau level transitions in $Nb_{1-x}Ta_xAs$, one can utilize a model which incorporates band inversion [141]. Initially this model was proposed to explain unusual magneto-optical features which were found in TaP - one of the representative of time-reversal invariant Weyl semimetals [141]. This theoretical framework describes the impact of the band inversion on the Weyl semimetals.

The model starts with the 2x2 Hamiltonian that describes a quartet of Weyl nodes from a Weyl semimetal with time-reversal symmetry:

$$\hat{H} = \begin{pmatrix} \Delta - \frac{\hbar^2 \mathbf{q}^2}{2M} & \gamma(\mathbf{q}) \\ \gamma^*(\mathbf{q}) & -\Delta + \frac{\hbar^2 \mathbf{q}^2}{2M} \end{pmatrix}. \tag{6.1}$$

Then the preserving electron-hole symmetry energy of spectrum of this Hamiltonian:

$$E(\mathbf{q}) = \pm \sqrt{\left(\Delta - \frac{\hbar^2 \mathbf{q}^2}{2M}\right)^2 + |\gamma(\mathbf{q})|^2}. \tag{6.2}$$

Off-diagonal coupling parameter $\gamma(\mathbf{q})$ indicates the nature of the system. For $\gamma = 0$ the system is a nodal-line semimetal, when the $\gamma =$ const the system is a gapped nodal-loop semimetal and a topological insulator if the $\gamma(\mathbf{q}) = \hbar v q_x + i q_y$. To find a time-reversal invariant 3D Weyl semimetal, the coupling term must present the non-isotropic form:

$$\gamma(\mathbf{q}) = \gamma_0 - \frac{\hbar^2 q_x^2}{2m_x} - \frac{\hbar^2 q_y^2}{2m_y} + i\hbar v_z q_z. \tag{6.3}$$

For a particular type of tunable parameters of the Hamiltonian 6.1 there will appear four zero-energy points, $E(\mathbf{q}^w)$. If the masses $M, m_x, m_y > 0$ the positions of this points can be determined as the crossing points of the circle:

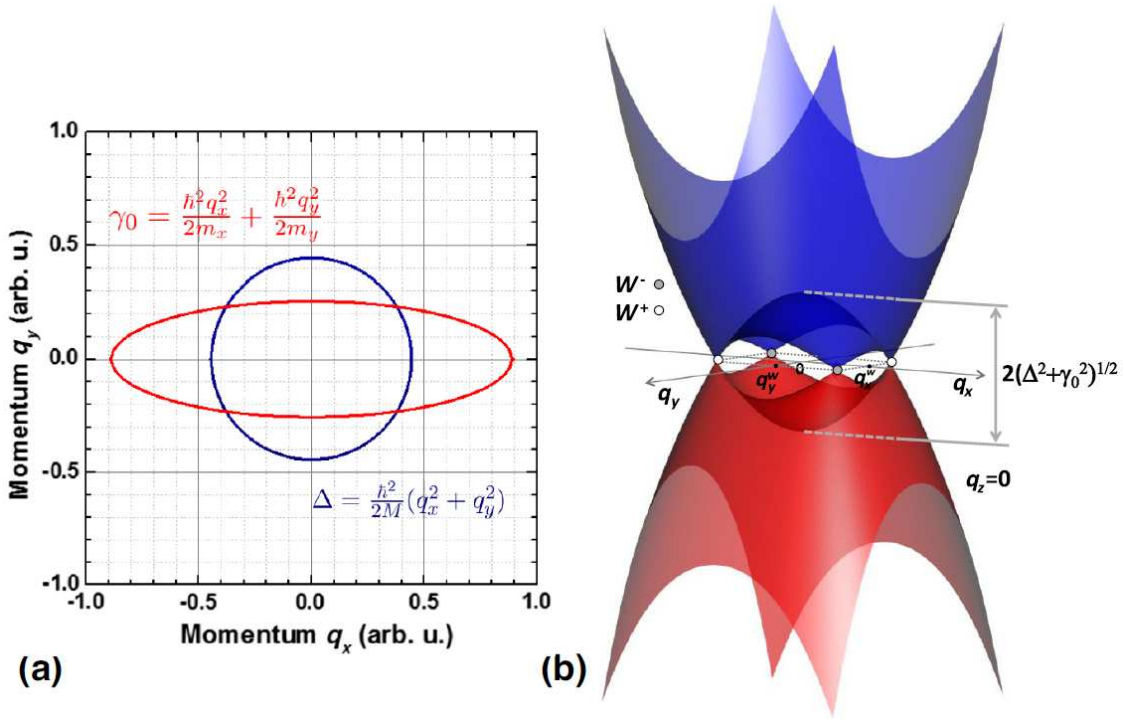


Figure 6.4: (a) Intersections of ellipse and circle are places where the Weyl cones are created. (b) Electronic band structure. Adapted from: [141], with the permission of publisher.

$$\Delta = \frac{\hbar^2(q_x^2 + q_y^2)}{2M}, \tag{6.4}$$

and an ellipse,

$$\gamma_0 = \frac{\hbar^2 q_x^2}{2m_x} + \frac{\hbar^2 q_y^2}{2m_y}, \tag{6.5}$$

which are defined by diagonal and off-diagonal terms of the 6.1, respectively. They can be seen in fig. 6.4.

For the zero energy points the conduction and valence bands cross forming four anisotropic, Weyl cones with particle-hole symmetry. As can be seen in fig. 6.4 (b), the created cones are merging at higher energies through two kinds of saddle points. In order to respect the time-reversal symmetry, a minimum of four nodes are needed for a consistent model. As the time-reversal symmetry is implying that the cones have the same chirality when they are located at $\mathbf{q}^w$ and $-\mathbf{q}^w$. While the total sum of chiralities of the Weyl cone quarter is equal to zero.

One can derive analytically the positions of Weyl points, their chirality, saddle point location as well as the strength of band inversion with the use of the described model. Then the energy of the saddle point for the component x:

$$E_x^{sp} = \frac{|M\Delta - \gamma_0 m_x|}{\sqrt{M^2 + m_x^2}}, \tag{6.6}$$

and:

$$E_y^{sp} = \frac{|M\Delta - \gamma_0 m_y|}{\sqrt{M^2 + m_y^2}}, \tag{6.7}$$

for the y component. The local extrema energies of the valence and conduction bands can be expressed as:

$$E(\mathbf{q} = 0) = \pm\sqrt{\Delta^2 + \gamma_0^2}. \tag{6.8}$$

Additionally analytic expression of the effective velocity v_{eff}, which is the spacing of Landau levels in the conical band approximation in the vicinity of the Weyl points:

$$v_{eff} = \sqrt{\frac{q_x^w q_y^w (m_x^{-1} - m_y^{-1})}{M}}. \tag{6.9}$$

In order to be able to compare the magneto-reflectivity measurements with the described model, one has to introduce the magnetic field to the Hamiltonian 6.1. With the use of the Peierls substitution the corresponding ladder operator is as follows:

$$a = \frac{l_b(q_x + iq_y)}{\sqrt{2}}. \tag{6.10}$$

The form of the Hamiltonian under Landau quantization is given by:

$$\hat{H}_B = \begin{pmatrix} \Delta - \hbar\omega_c(a^\dagger a + \frac{1}{2}) & \gamma(a, a^\dagger) \\ \gamma^*(a, a^\dagger) & -\Delta + \hbar\omega_c(a^\dagger a + \frac{1}{2}) \end{pmatrix}, \tag{6.11}$$

where:

$$\omega_c = \frac{eB}{M}, \tag{6.12}$$

and magnetic length l_B:

$$l_B = \sqrt{\frac{\hbar}{eB}}. \tag{6.13}$$

Finally the off-diagonal coupling parameter $\gamma^*(a, a^\dagger)$ reads:

$$\gamma^*(a, a^\dagger) = \gamma_0 - \frac{(a + a^\dagger)^2}{m_y l_B^2} - \frac{(a - a^\dagger)^2}{m_x l_B^2}. \tag{6.14}$$

It should be noted that, with the exception of the specific, linearly dispersing Landau level at $n = 0$, the magneto-optical response is mainly influenced by states with $q_z = 0$. As a result, the Hamiltonian was confined to this particular scenario.

In order to determine the energy spectrum of the Landau-quantized Hamiltonian 6.11, it is necessary to perform a diagonalization. However, due to the form of the Hamiltonian, an analytical solution is not feasible. As a result, a numerical method must be used, in which the Hamiltonian 6.11 is truncated to the chosen number of Landau levels and then diagonalized. This involves working with a matrix of infinite size, which is truncated in order to make the calculation feasible.

6.4 Sample description

To grow the crystals, a combination of NbAs and TaAs was used in a 50/50 ratio, with each weighing around 3 grams. The growth process took place in sealed quartz ampules, measuring 20 mm in diameter and 200-250 mm in length, using a two-temperature zone furnace with temperatures of 850°C and 900°C. Iodine was used as a transport agent, and the mixture was placed in the low-temperature zone of the furnace. After 2-3 weeks, solid solution crystals were formed in the hot zone of the ampule.

6.5 Experimental details and results

All of the experiments were performed in the Faraday configuration, where wave vectors of the incident and reflected light are parallel to the applied magnetic field. The measurements results were normalized by the response at the magnetic field $B = 0$ T to further visualize the changes induced by the magnetic field. Figure 6.5 presents the relative magneto-reflectivity $\frac{R_B}{R_0}$ of $Nb_{1-x}Ta_xAs$, alongside with its first derivative.

The low energy set of 6.5 presents an unusual feature of LL transitions which decrease in energy with the increasing magnetic field. This feature was observed previously in TaP crystals and is related to band inversion [141]. Moreover an almost horizontal line can be observed around the energy value of around 36 meV. Which is also the energy starting point for the down-dispersing line. The spectrum also shows a set of LL transitions from 50 meV to 150 meV, as well as a single broad interband LL transition starting at 150 meV. All of the features were used to extract the points indicating the positions of LL-transitions.

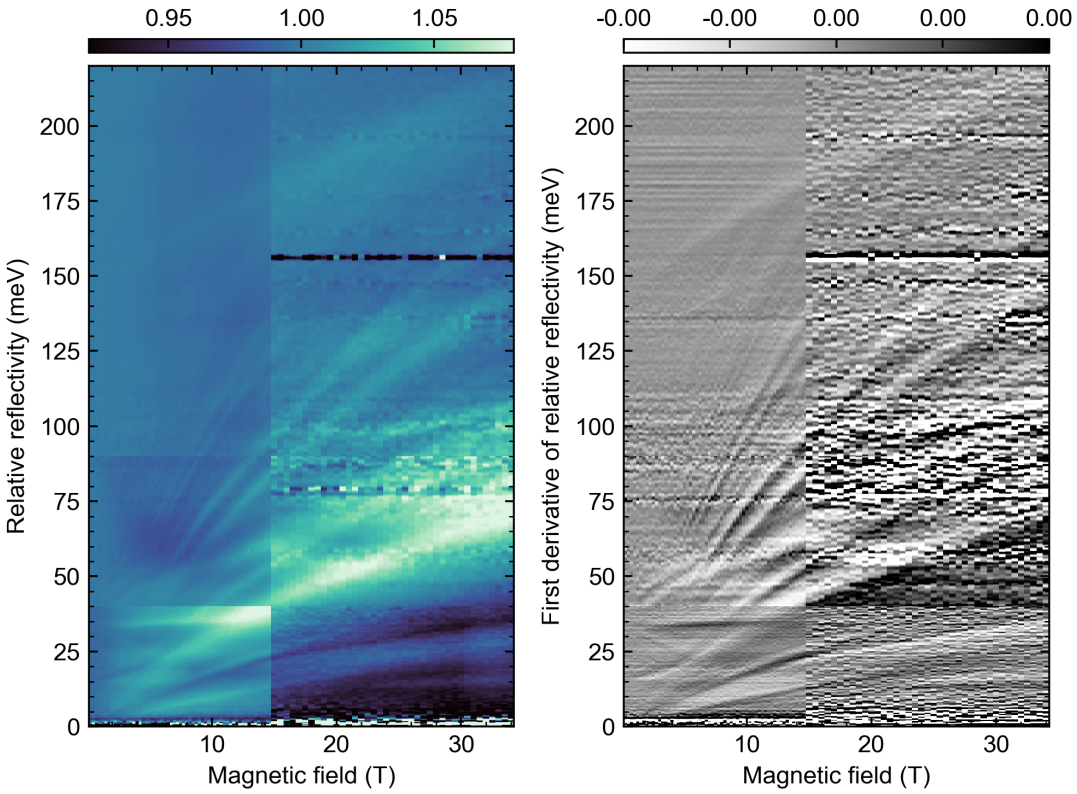


Figure 6.5: Left panel presents false color plot of relative magneto-reflectivity of S1 facet 1 and right panel its first derivative.

6.6 Modelled response of magneto-reflectivity

The aforementioned model (6.11) was used to predict the response of magneto-reflectivity of $Nb_{1-x}Ta_xAs$. Fig. 6.6 presents the obtained results of the calculations (c), for the inverted gap value of 36 meV (a) and the Landau levels (d).

In the fig. 6.6(b) one can observe the down-dispersive inter-LLs which are presented by solid green line which is extrapolating to 38 meV in the zero-field limit. Blue solid line marks the saddle point transition, while dashed orange and purple lines are representing intra- and inter-LL transitions. The magneto-reflectivity response includes sub-linear and $\sqrt{B}$ dependence which points to the presence of W1 and W2 cones, presented by orange and red dashed lines.

The Landau levels (6.6(c)) below the range of 20 meV, in the conduction band, present rich region of down-dispersing lines which origin directly from

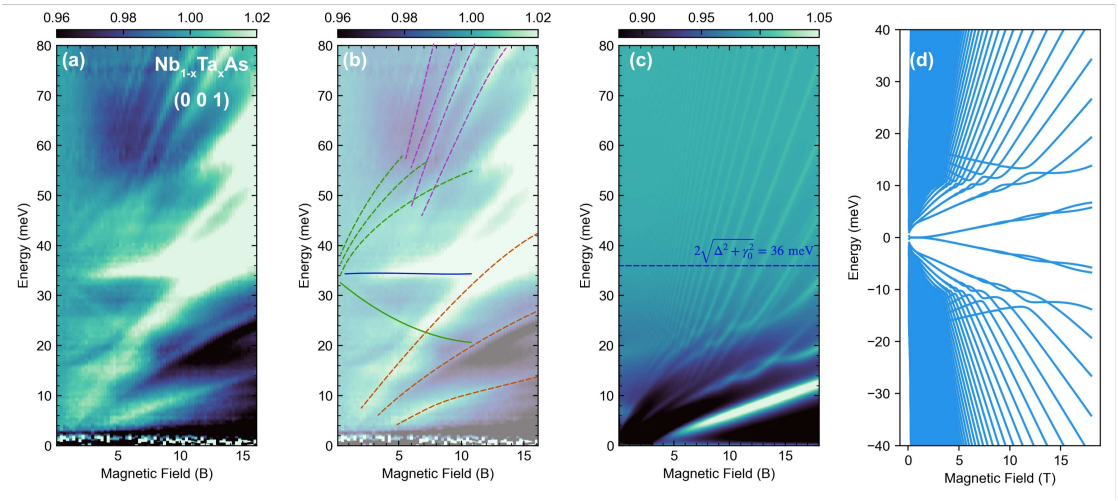


Figure 6.6: (a) Magneto-reflectivity of the $Nb_{1-x}Ta_xAs$ (001) facet plotted as $\frac{R_B}{R_0}$. (b) Magneto-reflectivity of the $Nb_{1-x}Ta_xAs$ (001) facet plotted as $\frac{R_B}{R_0}$ with extraction of the observed features. (c) Simulation of the magneto-reflectivity. The blue dotted line represents the $2\sqrt{\Delta^2+\gamma_0^2}$. (d) Calculated Landau levels.

the inverted band structure. In the limit of vanishing magnetic field they are extrapolating to the energy of the value $\sqrt{\Delta^2+\gamma_0^2}$, which is the position of a local maximum of the conduction band at the $q = 0$. Moreover the $\sqrt{B}$ dependence presented at the low energies points at the signature of massless charge carriers. In the valence band the similar situation can be seen, then the resulting transition between extrema are extrapolating to $2\sqrt{\Delta^2+\gamma_0^2}$.

On phenomenological level we obtained a good qualitative agreement between simulation and measured data, reproducing all of the key features such as: down dispersing inter-LL transitions and low energy excitations.

6.7 Summary

The chapter describes Weyl semimetals, which are materials that possess Weyl nodes acting as monopoles of Berry curvature in momentum space. The classification of Weyl semimetals can be based on the symmetry they possess and their tilt conditions. The main attention of the chapter is turned towards the experimental investigation of a ternary compound $Nb_{1-x}Ta_xAs$, a mixture of NbAs and TaAs, two well-studied representatives of Weyl semimetals group.

The motivation of this research lies in the search of the novel materials. By investigating whether NbTaAs exhibits Weyl semimetal properties, we aim at the expansion of a deeper understanding of the underlying physics of these fascinating materials. In this research we have used the means of magneto-optics to establish this experimental attempts.

The chapter also discusses the use of a model to explain the Landau level transitions in $Nb_{1-x}Ta_xAs$. This model incorporates band inversion and was originally proposed to explain unusual magneto-optical features observed in TaP, another Weyl semimetal. The successful fitting of this model to experimental data on $Nb_{1-x}Ta_xAs$ confirms the validity of the model in describing the effects of band inversion on Weyl semimetals. Additionally, the chapter notes that this ternary compound had not been previously measured, making this study a significant contribution to the field.

Moreover in the future the investigations of $Nb_{1-x}Ta_xAs$ with more concentrations ratios between Nb and Ta could help with the understanding of the mechanisms governing the material's topological behavior. As by the means of studying magneto-optics response of these samples, one can gain insight into the electronic band structure of $Nb_{1-x}Ta_xAs$ and particular its behavior as a Weyl semimetal.

7 Conclusion

Contents

7.1 Topological phase transition of $Hg_{1-x}Cd_xTe$ 99
7.2 Towards the topological phase transition of $(Cd_{1-x}Zn_x)_3As_2$ . . 100
7.3 Weyl semimetal $Nb_{1-x}Ta_xAs$ 101

My research primarily centers on the comprehensive examination of 3D materials, with a particular emphasis on adopting a relativistic approach within condensed matter physics. To delve deeper into these intriguing systems, we employ magneto-spectroscopy techniques within the THz frequency range. By leveraging this approach, we have examined the properties and behaviors of materials such as $Hg_{1-x}Cd_xTe$, $(Cd_{1-x}Zn_x)_3As_2$, and $Nb_{1-x}Ta_xAs$. These materials offer captivating platforms for exploring the intricate interplay between topology and electronic properties, with the ultimate aim of uncovering novel insights and paving the way for future technological advancements.

7.1 Topological phase transition of $Hg_{1-x}Cd_xTe$

This part of the thesis described the results and analysis of THz magneto-optical spectroscopy of $Hg_{1-x}Cd_xTe$ films under hydrostatic pressure, focusing

on samples near critical values of x for the topological phase transition from semimetal to semiconductor. The interband LLs transitions were analyzed using a simplified Kane model to extract the rest mass and velocity of the Kane fermions at various hydrostatic pressures. This allowed for the determination of the hydrostatic deformation potentials $a_c - a_v$ at 4 K without the need for band structure calculations. The measurements investigated negative and positive band gap values, corresponding to semi-metallic and semiconductor films, respectively. The deformation potential $a_c - a_v$ at low temperatures for any value of x was obtained using linear extrapolation between the obtained values and those reported in literature for CdTe at 2 K.

Better understanding of the influence of the substrate on the topological properties of $Hg_{1-x}Cd_xTe$ could be achieved by studying the samples grown on CdTe substrate. This measurements could include further magneto-optical investigations under hydrostatic pressure in the THz range.

7.2 Towards the topological phase transition of $(Cd_{1-x}Zn_x)_3As_2$

The chapter investigates the electronic properties of the material $(Cd_{1-x}Zn_x)_3As_2$ using magneto-optics to understand its topological properties and phase transitions. We measured magneto-reflectivity of samples with varying Zn content and identified cyclotron resonance and plasma edge splitting as features related to the material's electronic properties. The evolution of the material's band-gap was also investigated and what was found out is that it changes systematically with Zn content, consistent with the expected behavior of a topological quantum phase transition. The study appears to have successfully probed the band structure on either side of the topological phase transition, but confirmation is still pending.

To further understand the behavior of $(Cd_{1-x}Zn_x)_3As_2$ in magneto-optics one could employ the general solution for Bodnar model in magnetic field.

7.3 Weyl semimetal $Nb_{1-x}Ta_xAs$

This chapter focuses on the experimental investigation of $Nb_{1-x}Ta_xAs$, a ternary compound composed of NbAs and TaAs, both well-studied Weyl semimetals. The aim is to determine whether $Nb_{1-x}Ta_xAs$ exhibits Weyl semimetal properties, contributing to a deeper understanding of these materials. Magneto-optics is employed in the experimental analysis.

The chapter also discusses a model that explains Landau level transitions in $Nb1-xTaxAs$, confirming its validity in describing band inversion effects on Weyl semimetals. This study provides significant contributions as the first measurement of $Nb_{1-x}Ta_xAs$ and suggests further investigations with varying Nb and Ta concentrations to understand the material's topological behavior.

In order to understand the mechanisms behind the material's topological behavior one might want to test $Nb_{1-x}Ta_xAs$ with various contents of Nb and Ta. These investigations would be also meaningful in the search for the W1 cone separation picture, between Nb- and Ta- based compounds.

8

The results presented in this thesis have been published in the following publications:

- **M. Szoła**, Y. Ivonyak, J. Przybytek, N. Mikhailov, S. Dvoretsky, F. Teppe, and W. Knap, "Hydrostatic deformation potentials of narrow-gap HgCdTe" Phys. Rev. B 106, 195202 (2022).

Publications that were not included in the thesis are as follows:

- Gebert, S., Consejo, C., Krishtopenko, S.S., Ruffenach, S., **Szoła, M.,** et al. "Terahertz cyclotron emission from two-dimensional Dirac fermions". Nat. Photon. 17, 244–249 (2023).

- D. Yavorskiy, **M. Szoła**, T. Tarkowski, et al. Terahertz sources based on emission from a GaAs/AlGaAs heterostructure at cryogenic temperatures. Phys. Rev. Applied 16, 044001 (2021).

- P. Sai, S. O. Potashin, **M. Szoła**, D. Yavorskiy, G. Cywiński, P. Prystawko, J. Łusakowski, S. D. Ganichev, S. Rumyantsev, W. Knap, and V. Yu. Kachorovskii, "Beatings of ratchet current magneto-oscillations in GaN-based grating gate structures: Manifestation of spin-orbit band splitting", Phys. Rev. B 104, 045301 (2021).

- Yavorskiy, D., **Szoła, M.**, Karpierz, K., Bozek, R., Rudniewski, R., Karczewski, G., Wojtowicz, T., Wróbel, J., Łusakowski, J. "Grating metamaterials based on CdTe/CdMgTe quantum wells as terahertz detectors for high magnetic field applications", Applied Sciences Vol. 10 (2020).

- Yavorskiy, D., **Szoła, M.**, Karpierz, K., Rudniewski, R., Bozek, R., Karczewski, G., Wojtowicz, T., Wróbel, J., Łusakowski, J. "Polarization of magnetoplasmons in grating metamaterials based on CdTe/CdMgTe quantum wells", Materials Vol. 13 (2020).

- Yavorskiy, D., **Szola, M.**, Karpierz, K. Wlasny, I., Bozek, R., Rudniewski, R., Sniezek, D., Nowicki, P., Wrobel, J., Chusnutdinow, S., Karczewski, G., Wojtowicz, T., Lusakowski, J., "Terahertz Detectors Based on Plasmonic Excitations in Double CdTe/CdMgTe Quantum Wells", IEEE 2019 44th International Conference on Infrared, Millimeter, and Terahertz Waves (IRMMW-THz).

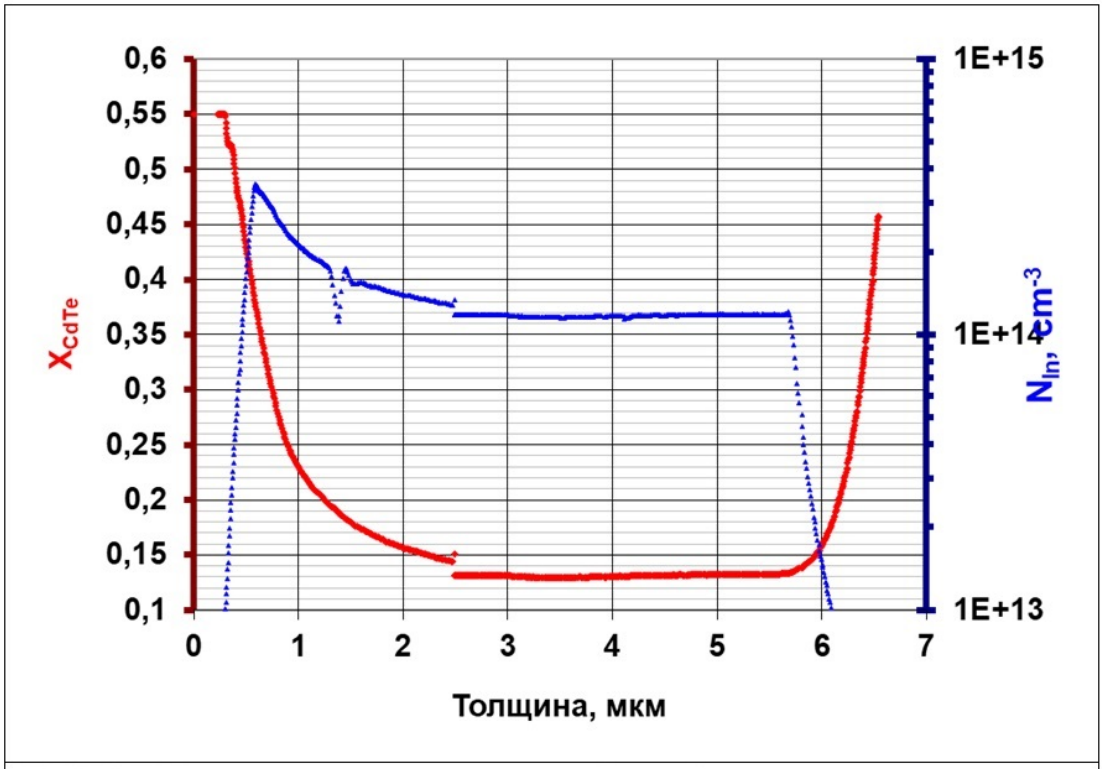
- D. Yavorskiy, **M. Szoła**, K. Karpierz, I. Własny, D. Śnieżek, P. Nowicki, J. Wróbel, S. Chusnutdinow, G. Karczewski, T. Wojtowicz and J. Łusakowski, "Terahertz Spectroscopy of Double CdTe/CdMgTe Quantum Wells", Acta Physica Polonica A Vol. 136 (2019).

- **M. Szoła**, M. Tokarczyk, G. Kowalski, J. Binder, K. Pakuła, A. Dąbrowska, A. Wysmołek and J. Łusakowski, "An Influence of X-Ray Irradiation on Mid-Bandgap Luminescence of Boron Nitride Epitaxial Layers", Acta Physica Polonica A Vol. 136 (2019).

9 Annex

Contents

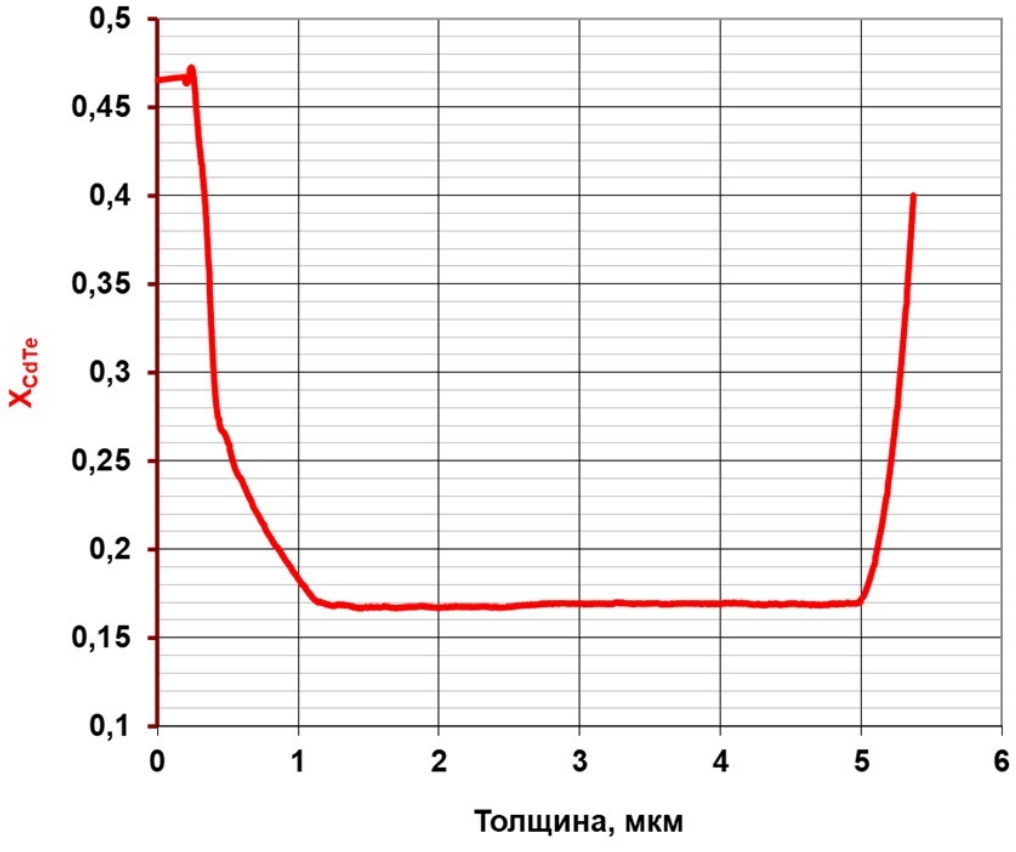
9.1 Detailed information about $Hg_{1-x}Cd_xTe$ samples 106



1MCT101007. Distribution of the composition over the sample thickness. The distribution of indium concentration is shown in blue.
X_{CdTe} = 0.15 (transmission), Hall at 77K: n = 4.3 × 10^{15} cm^{-3}, mobility = 3.48 × 10^5 cm^2 / Vc,
CdTe buffer layer thickness = 5.2 µm

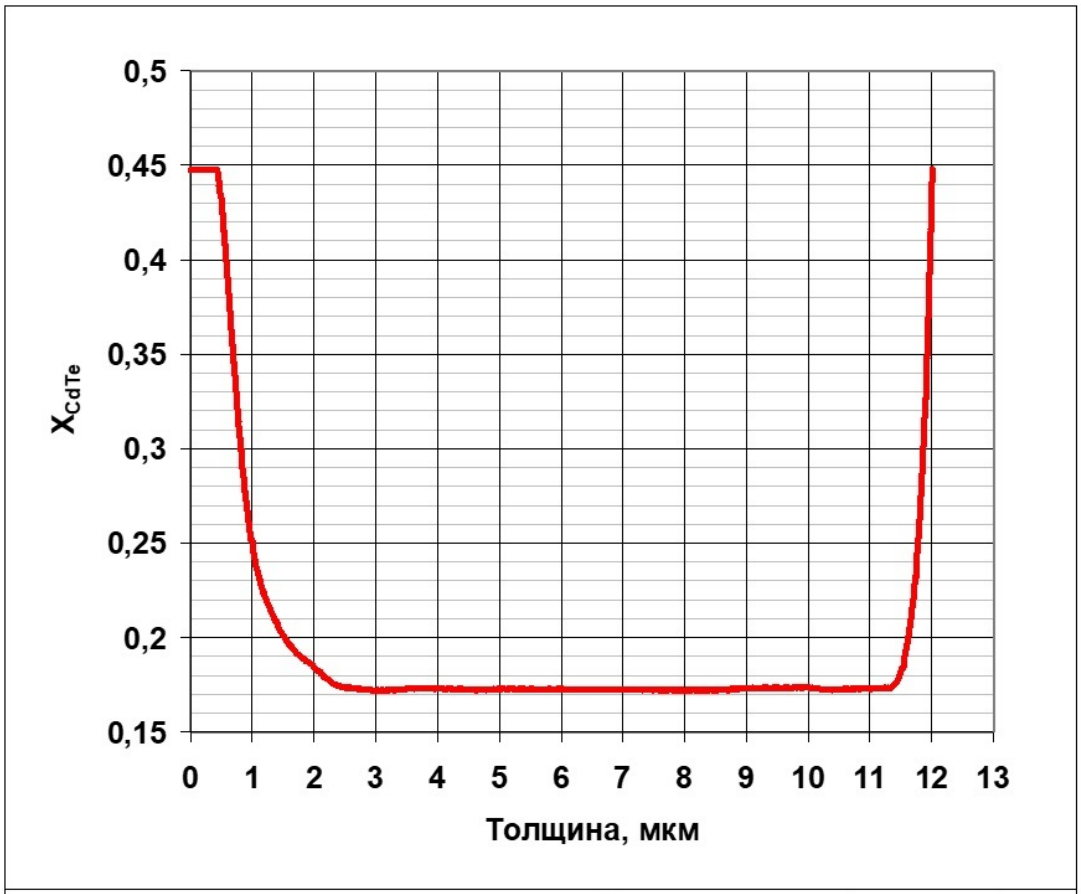
Figure 9.1: Information received from growers - sample 101007.

9.1 Detailed information about $Hg_{1-x}Cd_xTe$ samples



1MCT190404. Distribution of the composition over the sample thickness.
XCdTe = 0.169 (transmission), Hall at 77K: n = 3.5 × 10^{15} cm^{-3}, mobility = 1.8 × 10^{5} cm^{2} / Vc,
CdTe buffer layer thickness = 5.3 µm

Figure 9.2: Information received from growers - sample 190404.



1MCT130610. Distribution of the composition over the sample thickness. $X_{CdTe} = 0.1727$ (transmission), $X_{CdTe} = 0.49$ (reflection). Hall at 77K: n = 2.8×10^{15} cm^{-3}, mobility = 3.4×10^5 cm^2 / Vc, CdTe buffer layer thickness = 5.27 μm

Figure 9.3: Information received from growers - sample 130610.

References

[1] D. J. Dunstan, B. Gil, and K. P. Homewood, "Hydrostatic and uniaxial pressure coefficients of CdTe", Phys. Rev. B **38**, 7862–7865 (1988).

[2] M. Z. Hasan and C. L. Kane, "Colloquium: topological insulators", Rev. Mod. Phys. **82**, 3045–3067 (2010).

[3] M. P. Silverman, *And yet it moves* (Cambridge University Press, Cambridge, 1993).

[4] X. Chen, Z.-C. Gu, and X.-G. Wen, "Local unitary transformation, long-range quantum entanglement, wave function renormalization, and topological order", Physical Review B **82**, 155138 (2010).

[5] X.-L. Qi and S.-C. Zhang, "Topological insulators and superconductors", Rev. Mod. Phys. **83**, 1057–1110 (2011).

[6] M. Z. Hasan, S.-Y. Xu, I. Belopolski, and S.-M. Huang, "Discovery of Weyl fermion semimetals and topological Fermi arc states", Annual Review of Condensed Matter Physics **8**, 289–309 (2017).

[7] J Munkres, *Topology* (Pearson, 2018).

[8] A Hatcher, *Algebraic topology* (Cambridge University Press, 2002).

[9] A. Pressley, "The Gauss–Bonnet theorem", in *Elementary differential geometry* (Springer London, London, 2010), pp. 335–377.

[10] D. Carpentier, "Topology of bands in solids: from insulators to Dirac matter", in *Dirac matter*, edited by B. Duplantier, V. Rivasseau, and J.-N. Fuchs (Springer International Publishing, Cham, 2017), pp. 95–129.

[11] M. V. Berry, "Quantal phase factors accompanying adiabatic changes", Proceedings of the Royal Society of London. A. Mathematical and Physical Sciences **392**, 45–57 (1984).

[12] A. Shapere and F. Wilczek, "Geometric phases in physics", Reviews of Modern Physics **61**, 605 (1989).

[13] *Geometry, topology and physics*, https://www.taylorfrancis.com/books/mono/10.1201/9781315275826/geometry-topology-physics-mikio-nakahara, (Accessed on 12/13/2022).

[14] D. J. Griffiths, *Introduction to Quantum mechanics* (Cambridge University Press, 2018).

[15] *Interpolation approach to Hamiltonian-varying quantum systems and the adiabatic theorem, EPJ quantum technology*, https://epjquantumtechnology.springeropen.com/articles/10.1140/epjqt/s40507-015-0037-x, (Accessed on 02/02/2023).

[16] M. Fruchart and D. Carpentier, “An introduction to topological insulators”, Comptes Rendus Physique **14**, Topological insulators / Isolants topologiques, 779–815 (2013).

[17] D. Xiao, M.-C. Chang, and Q. Niu, “Berry phase effects on electronic properties”, Reviews of Modern Physics **82**, 1959 (2010).

[18] J. Zak, “Berry’s phase for energy bands in solids”, Phys. Rev. Lett. **62**, 2747–2750 (1989).

[19] O Viyuela, A Rivas, and M. A. Martin-Delgado, “Symmetry-protected topological phases at finite temperature”, 2D Materials **2**, 034006 (2015).

[20] D. Xiao, W. Yao, and Q. Niu, “Valley-contrasting physics in graphene: magnetic moment and topological transport”, Phys. Rev. Lett. **99**, 236809 (2007).

[21] L. Fu and C. L. Kane, “Topological insulators with inversion symmetry”, Phys. Rev. B **76**, 045302 (2007).

[22] N. P. Armitage, E. J. Mele, and A. Vishwanath, “Weyl and Dirac semimetals in three-dimensional solids”, Rev. Mod. Phys. **90**, 015001 (2018).

[23] A. A. Burkov and L. Balents, “Weyl semimetal in a topological insulator multilayer”, Phys. Rev. Lett. **107**, 127205 (2011).

[24] B. Yan and C. Felser, “Topological materials: Weyl semimetals”, Annual Review of Condensed Matter Physics **8**, 337–354 (2017).

[25] Z. Wang, Y. Sun, X.-Q. Chen, C. Franchini, G. Xu, H. Weng, X. Dai, and Z. Fang, “Dirac semimetal and topological phase transitions in A_3Bi (A = Na, K, Rb)”, Phys. Rev. B **85**, 195320 (2012).

[26] N. P. Armitage, E. J. Mele, and A. Vishwanath, “Weyl and Dirac semimetals in three-dimensional solids”, Reviews of Modern Physics **90**, 015001 (2018).

[27] A. A. Soluyanov, D. Gresch, Z. Wang, Q. Wu, M. Troyer, X. Dai, and B. A. Bernevig, “Type-ii Weyl semimetals”, Nature **527**, 495–498 (2015).

[28] K. Shanavas, “Overview of theoretical studies of Rashba effect in polar perovskite surfaces”, Journal of Electron Spectroscopy and Related Phenomena **201**, Special issue on electron spectroscopy for Rashba spin-orbit interaction, 121–126 (2015).

[29] C. Fang et al., “Topological nodal line semimetals”, Chinese Phys. B **25**, 117106 (2016).

[30] S.-Y. Yang, H. Yang, E. Derunova, S. S. P. Parkin, B. Yan, and M. N. Ali, “Symmetry demanded topological nodal-line materials”, Advances in Physics: X **3**, 1414631 (2018).

[31] Z. Wang, H. Weng, Q. Wu, X. Dai, and Z. Fang, “Three-dimensional Dirac semimetal and quantum transport in Cd3As2”, Physical Review B **88**, 125427 (2013).

[32] Z. K. Liu, B Zhou, Y Zhang, Z. J. Wang, H. M. Weng, D Prabhakaran, S. K. Mo, Z. X. Shen, Z Fang, X Dai, et al., “Discovery of a three-dimensional topological Dirac semimetal, Na3Bi”, Science **343**, 864–867 (2014).

[33] H. B. Nielsen and M Ninomiya, “The Adler-Bell-Jackiw anomaly and Weyl fermions in a crystal”, Physics Letters B **130**, 389–396 (1983).

[34] O. Vafek and A. Vishwanath, "Dirac fermions in solids: from high-tc cuprates and graphene to topological insulators and weyl semimetals", Annual Review of Condensed Matter Physics **5**, 83–112 (2014).

[35] J. Gooth, G. Schierning, C. Felser, and K. Nielsch, "Quantum materials for thermoelectricity", MRS Bulletin **43**, 187–192 (2018).

[36] Y. Ando, "Topological insulator materials", Journal of the Physical Society of Japan **82**, 102001 (2013).

[37] X.-L. Qi and S.-C. Zhang, "Topological insulators and superconductors", Reviews of Modern Physics **83**, 1057–1110 (2011).

[38] Y Tanaka, Z. Ren, T Sato, K Nakayama, S Souma, T Takahashi, K. Segawa, and Y. Ando, "Experimental realization of a topological crystalline insulator in SnTe", Nature Physics **8**, 800–803 (2012).

[39] A. T. Stewart and M. A. H. Vozmediano, "The theory of optical response of topological insulators", in *Topological insulators*, edited by M. Franz and L. W. Molenkamp (2013), pp. 297–323.

[40] M. S. Dresselhaus, G. Dresselhaus, A. Jorio, and A. G. Souza Filho, *Group theory: application to the physics of condensed matter* ().

[41] B. L. Smith, "Relation of the dielectric constant and the refractive index to thermodynamic properties", in *Experimental thermodynamics volume ii: experimental thermodynamics of non-reacting fluids*, edited by B. Le Neindre and B. Vodar (Springer US, Boston, MA, 1968), pp. 579–606.

[42] M. Orlita and M. Potemski, "Dirac electronic states in graphene systems: optical spectroscopy studies", Semiconductor Science and Technology **25**, 063001 (2010).

[43] "Front matter", edited by C. Lamberti and G. Agostini, iii (2013).

[44] *Modeling graphene in high-frequency electromagnetics | comsol blog*, https://www.comsol.fr/blogs/modeling-graphene-in-high-frequency-electromagnetics/, (Accessed on 03/07/2023).

[45] P. Drude, "Zur elektronentheorie der metalle", Annalen der Physik **306**, 566–613 (1900).

[46] *A simplified derivation of the Kubo-Greenwood formula: american journal of physics: vol 46, no 6*, https://aapt.scitation.org/doi/10.1119/1.11229, (Accessed on 01/18/2023).

[47] M. Orlita, B. A. Piot, G. Martinez, N. K. S. Kumar, C. Faugeras, M. Potemski, C. Michel, E. M. Hankiewicz, T. Braunerar, familyi=v., given= Č., giveni=i. c. v., „ S. Schreyeck, S. Grauer, K. Brunner, C. Gould, C. Brüne, and L. W. Molenkamp, "Magneto-optics of massive dirac fermions in bulk Bi_2Se_3", Phys. Rev. Lett. **114**, 186401 (2015).

[48] L. V. Keldysh, "Diagram technique for nonequilibrium processes", Journal of Experimental and Theoretical Physics **47**, 1515–1527 (1965).

[49] J. Zak and W. Zawadzki, "Effective-mass approximation for electrons in crossed electric and magnetic fields", Phys. Rev. **145**, 536–542 (1966).

[50] W. Zawadzki and B. Lax, "Two-band model for bloch electrons in crossed electric and magnetic fields", Phys. Rev. Lett. **16**, 1001–1003 (1966).

[51] W. Zawadzki, S. Klahn, and U. Merkt, "Semirelativistic behavior of electrons in insb in crossed magnetic and electric fields", Phys. Rev. Lett. **55**, 983–986 (1985).

[52] P. Pfeffer and W. Zawadzki, "Five-level k·p model for the conduction and valence bands of gaas and inp", Phys. Rev. B **53**, 12813–12828 (1996).

[53] W. Zawadzki, S. Klahn, and U. Merkt, "Inversion electrons on narrow-band-gap semiconductors in crossed electric and magnetic fields", Phys. Rev. B **33**, 6916–6928 (1986).

[54] J. Wyzula, X. Lu, D. Santos-Cottin, D. K. Mukherjee, I. Mohelský, F. Le Mardelé, J. Novák, M. Novak, R. Sankar, Y. Krupko, B. A. Piot, W.-L. Lee, A. Akrap, M. Potemski, M. O. Goerbig, and M. Orlita, "Lorentz-boost-driven magneto-optics in a dirac nodal-line semimetal", Advanced Science **9**, 2105720 (2022).

[55] E. Kane, "Zener tunneling in semiconductors", Journal of Physics and Chemistry of Solids **12**, 181–188 (1960).

[56] E. O. Kane, "Band structure of indium antimonide", Journal of Physics and Chemistry of Solids **1**, 249–261 (1957).

[57] E. O. Kane, "The influence of exchange on the effective mass formalism", Journal of Physics and Chemistry of Solids **6**, 236–241 (1958).

[58] M. Orlita, D. Basko, M. Zholudev, and et al., "Observation of three-dimensional massless kane fermions in a zinc-blende crystal", Nature Phys **10**, 233–238 (2014).

[59] D. B. But, M. Mittendorff, C. Consejo, F. Teppe, N. N. Mikhailov, S. A. Dvoretskii, C. Faugeras, S. Winnerl, M. Helm, W. Knap, M. Potemski, and M. Orlita, "Suppressed Auger scattering and tunable light emission of Landau-quantized massless Kane electrons", Nature Photonics, – (2019).

[60] W. Minkina, "How infrared radiation was discovered—range of this discovery and detailed, unknown information", Applied Sciences **11**, 10.3390/app11219824 (2021).

[61] *Bridge for the terahertz gap*, https://www.nature.com/articles/417132b, (Accessed on 01/18/2023).

[62] S. D. Ganichev and W. Prettl, "1INTRODUCTION", in *Intense Terahertz Excitation of Semiconductors* (Oxford University Press, Dec. 2005).

[63] R. A. Lewis, "A review of terahertz sources", Journal of Physics D: Applied Physics **47**, 374001 (2014).

[64] *Fourier transform infrared spectrometry, 2nd edition, Wiley*, https://www.wiley.com/en-br/Fourier+Transform+Infrared+Spectrometry,+2nd+Edition-p-9780471194040, (Accessed on 01/18/2023).

[65] A. A. Michelson, "XXVIII. visibility of interference-fringes in the focus of a telescope", The London, Edinburgh, and Dublin Philosophical Magazine and Journal of Science **31**, 256–259 (1891).

[66] A Rogalski, "HgCdTe infrared detector material: history, status and outlook", Rep. Prog. Phys. **68**, 2267–2336 (2005).

[67] V. S. Varavin, S. A. Dvoretskii, N. N. Mikhailov, V. G. Remesnik, I. V. Sabinina, Y. G. Sidorov, V. A. Shvets, M. V. Yakushev, and A. V. Latyshev, "Molecular beam epitaxy of CdHgTe: current state and horizons.", Optoelectron. Instrument. Proc. **56**, 456–469 (2020).

[68] A. M. Kadykov, J. Torres, S. S. Krishtopenko, C. Consejo, S. Ruffenach, M. Marcinkiewicz, D. But, W. Knap, S. V. Morozov, V. I. Gavrilenko, N. N. Mikhailov, S. A. Dvoretsky, and F. Teppe, "Terahertz imaging of Landau levels in HgTe-based topological insulators", Appl. Phys. Lett. **108**, 262102 (2016).

[69] S. Ruffenach, A. Kadykov, V. V. Rumyantsev, J. Torres, D. Coquillat, D. But, S. S. Krishtopenko, C. Consejo, W. Knap, S. Winnerl, M. Helm, M. A. Fadeev, N. N. Mikhailov, S. A. Dvoretskii, V. I. Gavrilenko, S. V. Morozov, and F. Teppe, "HgCdTe-based heterostructures for terahertz photonics", APL Mater. **5**, 035503 (2017).

[70] S. V. Morozov, V. V. Rumyantsev, M. A. Fadeev, M. S. Zholudev, K. E. Kudryavtsev, A. V. Antonov, A. M. Kadykov, A. A. Dubinov, N. N. Mikhailov, S. A. Dvoretsky, and V. I. Gavrilenko, "Stimulated emission from (HgCdTe) quantum well heterostructures at wavelengths up to 19.5μm", Appl. Phys. Lett. **111**, 192101 (2017).

[71] K. E. Kudryavtsev, V. V. Rumyantsev, V. Y. Aleshkin, A. A. Dubinov, V. V. Utochkin, M. A. Fadeev, N. N. Mikhailov, G. Alymov, D. Svintsov, V. I. Gavrilenko, and S. V. Morozov, "Temperature limitations for stimulated emission in 3–4 μm range due to threshold and non-threshold Auger recombination in HgTe/CdHgTe quantum wells", Appl. Phys. Lett. **117**, 083103 (2020).

[72] V. V. Utochkin, K. E. Kudryavtsev, M. A. Fadeev, A. A. Razova, D. S. Bykov, V. Y. Aleshkin, A. A. Dubinov, N. N. Mikhailov, S. A. Dvoretsky, V. V. Rumyantsev, V. I. Gavrilenko, and S. V. Morozov, "Mid-IR stimulated emission in Hg(Cd)Te/CdHgTe quantum well structures up to 200 K due to suppressed Auger recombination", Laser Phys. **31**, 015801 (2020).

[73] A. Walsh, S.-H. Wei, S. Chen, and X. G. Gong, "Design of quaternary chalcogenide photovoltaic absorbers through cation mutation", in 2009 34th ieee photovoltaic specialists conference (pvsc) (2009), pp. 001875–001878.

[74] R. Piotrzkowski, S. Porowski, Z. Dziuba, J. Ginter, W. Giriat, and L. Sosnowski, "Band structure of HgTe", physica status solidi (b) **8**, K135–K139 (1965).

[75] F. Teppe, M. Marcinkiewicz, S. S. Krishtopenko, S. Ruffenach, C. Consejo, A. M. Kadykov, W. Desrat, D. But, W. Knap, J. Ludwig, S. Moon, D. Smirnov, M. Orlita, Z. Jiang, S. V. Morozov, V. Gavrilenko, N. N. Mikhailov, and S. A. Dvoretskii, "Temperature-driven massless Kane fermions in HgCdTe crystals", Nat. Commun. **7**, 12576 (2016).

[76] J. P. Laurenti, J. Camassel, A. Bouhemadou, B. Toulouse, R. Legros, and A. Lusson, "Temperature dependence of the fundamental absorption edge of mercury cadmium telluride", J. Appl. Phys. **67**, 6454–6460 (1990).

[77] C. Brüne, C. X. Liu, E. G. Novik, E. M. Hankiewicz, H. Buhmann, Y. L. Chen, X. L. Qi, Z. X. Shen, S. C. Zhang, and L. W. Molenkamp, "Quantum Hall effect from the topological surface states of strained bulk HgTe", Phys. Rev. Lett. **106**, 126803 (2011).

[78] J. Ruan, S.-K. Jian, H. Yao, H. Zhang, S.-C. Zhang, and D. Xing, "Symmetry-protected ideal Weyl semimetal in HgTe-class materials", Nat. Commun. **7**, 11136 (2016).

[79] D. M. Mahler, J.-B. Mayer, P. Leubner, L. Lunczer, D. Di Sante, G. Sangiovanni, R. Thomale, E. M. Hankiewicz, H. Buhmann, C. Gould, and L. W. Molenkamp, "Interplay of Dirac nodes and Volkov-Pankratov surface states in compressively strained HgTe", Phys. Rev. X **9**, 031034 (2019).

[80] D. A. Kozlov, Z. D. Kvon, E. B. Olshanetsky, N. N. Mikhailov, S. A. Dvoretsky, and D. Weiss, "Transport properties of a 3D topological insulator based on a strained high-mobility HgTe film", Phys. Rev. Lett. **112**, 196801 (2014).

[81] B. A. Bernevig, T. L. Hughes, and S.-C. Zhang, "Quantum spin Hall effect and topological phase transition in HgTe quantum wells", Science **314**, 1757–1761 (2006).

[82] M. König, S. Wiedmann, C. Brüne, A. Roth, H. Buhmann, L. W. Molenkamp, X.-L. Qi, and S.-C. Zhang, "Quantum spin Hall insulator state in HgTe quantum wells", Science **318**, 766–770 (2007).

[83] S. S. Krishtopenko, W. Knap, and F. Teppe, "Phase transitions in two tunnel-coupled HgTe quantum wells: bilayer graphene analogy and beyond", Sci. Rep. **6**, 30755 (2016).

[84] E. B. Olshanetsky, Z. D. Kvon, G. M. Gusev, A. D. Levin, O. E. Raichev, N. N. Mikhailov, and S. A. Dvoretsky, "Persistence of a two-dimensional topological insulator state in wide HgTe quantum wells", Phys. Rev. Lett. **114**, 126802 (2015).

[85] S. S. Krishtopenko, I. Yahniuk, D. B. But, V. I. Gavrilenko, W. Knap, and F. Teppe, "Pressure- and temperature-driven phase transitions in HgTe quantum wells", Phys. Rev. B **94**, 245402 (2016).

[86] M. Marcinkiewicz, S. Ruffenach, S. S. Krishtopenko, A. M. Kadykov, C. Consejo, D. B. But, W. Desrat, W. Knap, J. Torres, A. V. Ikonnikov, K. E. Spirin, S. V. Morozov, V. I. Gavrilenko, N. N. Mikhailov, S. A. Dvoretskii, and F. Teppe, "Temperature-driven single-valley Dirac fermions in HgTe quantum wells", Phys. Rev. B **96**, 035405 (2017).

[87] A. M. Kadykov, S. S. Krishtopenko, B. Jouault, W. Desrat, W. Knap, S. Ruffenach, C. Consejo, J. Torres, S. V. Morozov, N. N. Mikhailov, S. A. Dvoretskii, and F. Teppe, "Temperature-induced topological phase transition in HgTe quantum wells", Phys. Rev. Lett. **120**, 086401 (2018).

[88] Z. D. Kvon, D. A. Kozlov, E. B. Olshanetsky, G. M. Gusev, N. N. Mikhailov, and S. A. Dvoretsky, "Topological insulators based on HgTe", Physics-Uspekhi **63**, 629–647 (2020).

[89] G. A. Babonas, R. A. Bendoryus, and A. Y. Shileika, Sov. Phys. Semicond. **5**, 392 (1971).

[90] J. Mei and V. Lemos, "Photoluminescence on CdSe and CdTe under hydrostatic pressure", Solid State Commun. **52**, 785–788 (1984).

[91] W. Shan, S. Shen, and H. Zhu, "Pressure dependence of the absorption edge for Cd1-xMnxTe", Solid State Commun. **55**, 475–478 (1985).

[92] J. González, F. Pérez, E. Moya, and J. Chervin, "Hydrostatic pressure dependence of the energy gaps of CdTe in the zinc-blende and rocksalt phases", J. Phys. Chem. Solids **56**, 335–340 (1995).

[93] H. Cheong, J. Burnett, and W. Paul, "Photoluminescence of CdTe under hydrostatic pressure", Solid State Commun. **77**, 565–566 (1991).

[94] S. Jiang, S. C. Shen, D. Li, Y. Q. Ju, H. Zhu, and J. Schilz, "Pressure dependence of energy gap for $Cd_{0.7}Hg_{0.3}Te$", Appl. Phys. Lett. **60**, 3171–3173 (1992).

[95] C. Verié, "Sur la structure de bandes des alliages HgTe-CdTe I. mesures électriques", Phys. Stat. Sol. (b) **17**, 889–901 (1966).

[96] J. C. Gonthier, A Raymond, J. L. Robert, R Triboulet, and J. P. Faurie, "Characterisation under hydrostatic pressure of narrow-gap Hg1-xCdxTe and Hg1-xZnxTe", Semicond. Sci. Technol. **5**, S217–S220 (1990).

[97] M. Carvalho, C. Fau, and M. Averous, "First order phase transition of Hall coefficient versus magnetic field, under hydrostatic pressure due to freeze-out on acceptor state in Hg0.836Cd0.164Te", in Physics of narrow gap semiconductors, edited by E. Gornik, H. Heinrich, and L. Palmetshofer (1982), pp. 430–434.

[98] C. T. Elliott, J. Melngailis, T. C. Harman, J. A. Kafalas, and W. C. Kernan, "Pressure dependence of the carrier concentrations in p-type alloys of $Hg_{1-x}Cd_xTe$ at 4.2 and 77°K", Phys. Rev. B **5**, 2985–2997 (1972).

[99] C. Fau, J. F. Dame, M. de Carvalho, J. Calas, M. Averous, and B. A. Lombos, "Three-band model applied to narrow-gap HgCdTe", Phys. Stat. Sol. (b) **125**, 831–838 (1984).

[100] J. Stankiewicz and W. Giriat, "Galvanomagnetic properties of pure HgTe under high hydrostatic pressure", Phys. Rev. B **13**, 665–672 (1976).

[101] V. Latussek, C. R. Becker, G. Landwehr, R. Bini, and L. Ulivi, "Deformation potentials of the semimetal HgTe", Phys. Rev. B **71**, 125305 (2005).

[102] D. Yavorskiy et al. Band-gap pressure coefficient of Hg1xCdxTe epitaxial layers (submitted to PRB).

[103] Y. Sidorov, A. Anciferov, V. Varavin, S. Dvoretsky, N. Mikhailov, M. Yakushev, I. Sabinina, V. Remesnik, D. Ikusov, I. Uzhakov, G. Sidorov, V. Kuzmin, S. Rihlicky, V. Shvets, A. Mardezov, E. Spesivcev, A. Gutakovskii, and A. Latyshev, "Molecular beam epitaxy of $Cd_xHg_{1-x}Te$", edited by A. V. Latyshev, A. V. Dvurechenskii, and A. L. Aseev, 297–323 (2017).

[104] *Terahertz magnetospectroscopy of cyclotron resonances from topological surface states in thick films of CdxHg1xTe*, https://onlinelibrary.wiley.com/doi/full/10.1002/pssb.202000023, (Accessed on 01/16/2023).

[105] M. Orlita, D. M. Basko, M. S. Zholudev, F. Teppe, W. Knap, V. I. Gavrilenko, N. N. Mikhailov, S. A. Dvoretskii, P. Neugebauer, C. Faugeras, A.-L. Barra, G. Martinez, and M. Potemski, "Observation of three-dimensional massless Kane fermions in a zinc-blende crystal", Nature Phys. **10**, 233–238 (2014).

[106] M. D. Frogley, J. L. Sly, and D. J. Dunstan, "Pressure dependence of the direct band gap in tetrahedral semiconductors", Phys. Rev. B **58**, 12579–12582 (1998).

[107] E. Deligoz, K. Colakoglu, and Y. Ciftci, "Elastic, electronic, and lattice dynamical properties of CdS, CdSe, and CdTe", Physica B **373**, 124 –130 (2006).

[108] S. Adachi, *Properties of Group-IV, III-V and II-VI Semiconductors*, edited by Peter Capper, Safa Kasap, Arthur Willoughby (John Wiley & Sons Ltd., 2005).

[109] *Mercury Cadmium Telluride - Growth, Properties and Applications*, edited by Peter Capper and James Garland (John Wiley & Sons Ltd., 2011).

[110] S. Nishihaya, M. Uchida, Y. Nakazawa, M. Kriener, Y. Kozuka, Y. Taguchi, and M. Kawasaki, "Gate-tuned quantum hall states in Dirac semimetal (Cd1xZnx)3As2", Science Advances **4**, eaar5668 (2018).

[111] H. Lu, X. Zhang, and Y. e. a. Bian, *Topological phase transition in single crystals of* $(Cd_{1-x}Zn_x)_3as_2$, 2017.

[112] M. Hakl, S. Tchoumakov, I. Crassee, A. Akrap, B. A. Piot, C. Faugeras, G. Martinez, A. Nateprov, E. Arushanov, F. Teppe, R. Sankar, W. li Lee, J. Debray, O. Caha, J. Novák, M. O. Goerbig, M. Potemski, and M. Orlita, "Energy scale of Dirac electrons in Cd3As2", Physical Review B **97**, 10.1103/physrevb.97.115206 (2018).

[113] Z. Wang, H. Weng, Q. Wu, X. Dai, and Z. Fang, "Three-dimensional Dirac semimetal and quantum transport in cd_3as_2", Phys. Rev. B **88**, 125427 (2013).

[114] I. Crassee, R. Sankar, W.-L. Lee, A. Akrap, and M. Orlita, "3d Dirac semimetal Cd3As2: a review of material properties", Physical Review Materials **2**, 10.1103/physrevmaterials.2.120302 (2018).

[115] M. Neupane, S.-Y. Xu, R. Sankar, and et al., "Observation of a three-dimensional topological Dirac semimetal phase in high-mobility Cd3As2", Nature Communications **5**, 3786 (2014).

[116] J. Bodnar, Proceedings of the 3rd International Conference on the Physics of Narrow Gap Semiconductors, 1977.

[117] A. Akrap, M. Hakl, S. Tchoumakov, I. Crassee, J. Kuba, M. O. Goerbig, C. C. Homes, O. Caha, J. Novák, F. Teppe, W. Desrat, S. Koohpayeh, L. Wu, N. P. Armitage, A. Nateprov, E. Arushanov, Q. D. Gibson, R. J. Cava, D. van der Marel, B. A. Piot, C. Faugeras, G. Martinez, M. Potemski, and M. Orlita, "Magneto-optical signature of massless Kane electrons in Cd_3As_2", Phys. Rev. Lett. **117**, 136401 (2016).

[118] *Landau quantization and quasiparticle interference in the three-dimensional Dirac semimetal Cd3As2, Nature materials*, https://www.nature.com/articles/nmat4023, (Accessed on 01/25/2023).

[119] *A stable three-dimensional topological Dirac semimetal Cd3As2, Nature materials*, https://www.nature.com/articles/nmat3990, (Accessed on 01/25/2023).

[120] S. Borisenko, Q. Gibson, D. Evtushinsky, V. Zabolotnyy, B. Büchner, and R. J. Cava, "Experimental realization of a three-dimensional Dirac semimetal", Phys. Rev. Lett. **113**, 027603 (2014).

[121] E. D. Palik and J. K. Furdyna, "Infrared and microwave magnetoplasma effects in semiconductors", Reports on Progress in Physics **33**, 1193 (1970).

[122] E. Arushanov, "Crystal growth and characterization of II3V2 compounds", Progress in Crystal Growth and Characterization **3**, 211–255 (1980).

[123] I. Crassee, E. Martino, C. C. Homes, O. Caha, J. Novák, P. Tückmantel, M. Hakl, A. Nateprov, E. Arushanov, Q. D. Gibson, R. J. Cava, S. M. Koohpayeh, K. E. Arpino, T. M. McQueen, M. Orlita, and A. Akrap, "Nonuniform carrier density in Cd_3As_2 evidenced by optical spectroscopy", Phys. Rev. B **97**, 125204 (2018).

[124] J. M. Pawlikowski, J. Misiewicz, B. Sujak-Cyrul, and J. Wróbel, "Absorption edge of zn_3as_2 at 5, 80, and 300 K", physica status solidi (b) **92**, K123 (1979).

[125] S. Zhang, Y. Wang, Q. Zeng, J. Shen, X. Zheng, J. Yang, Z. Wang, C. Xi, B. Wang, M. Zhou, R. Huang, H. Wei, Y. Yao, S. Wang, S. S. P. Parkin, C. Felser, E. Liu, and B. Shen, "Scaling of berry-curvature monopole dominated large linear positive magnetoresistance", Proceedings of the National Academy of Sciences **119**, e2208505119 (2022).

[126] A. Singh and J. P. Carbotte, "Effect of the chiral anomaly on circular dichroism and Hall angle in doped and tilted Weyl semimetals", Phys. Rev. B **99**, 235134 (2019).

[127] C.-C. Lee, S.-Y. Xu, S.-M. Huang, D. S. Sanchez, I. Belopolski, G. Chang, G. Bian, N. Alidoust, H. Zheng, M. Neupane, B. Wang, A. Bansil, M. Z. Hasan, and H. Lin, "Fermi surface interconnectivity and topology in Weyl fermion semimetals TaAs, TaP, NbAs, and NbP", Phys. Rev. B **92**, 235104 (2015).

[128] S. Souma, Z. Wang, H. Kotaka, T. Sato, K. Nakayama, Y. Tanaka, H. Kimizuka, T. Takahashi, K. Yamauchi, T. Oguchi, K. Segawa, and Y. Ando, "Direct observation of nonequivalent Fermi-arc states of opposite surfaces in the noncentrosymmetric Weyl semimetal NbP", Phys. Rev. B **93**, 161112 (2016).

[129] S. Tchoumakov, M. Civelli, and M. O. Goerbig, "Magnetic-field-induced relativistic properties in type-I and type-II Weyl semimetals", Phys. Rev. Lett. **117**, 086402 (2016).

[130] B. Lv, H. Weng, B. Fu, X. Wang, H. Miao, J. Ma, P. Richard, X. Huang, L. Zhao, G. Chen, et al., "Experimental discovery of weyl semimetal taas", Physical Review X **5**, 031013 (2015).

[131] H. Weng, C. Fang, Z. Fang, B. A. Bernevig, and X. Dai, "Weyl semimetal phase in noncentrosymmetric transition-metal monophosphides", Phys. Rev. X **5**, 011029 (2015).

[132] A. A. Soluyanov, D. Gresch, Z. Wang, Q. Wu, M. Troyer, X. Dai, and B. A. Bernevig, "Type-ii Weyl semimetals", Nature **527**, 495–498 (2015).

[133] X. Wan, A. M. Turner, A. Vishwanath, and S. Y. Savrasov, "Topological semimetal and Fermi-arc surface states in the electronic structure of pyrochlore iridates", Physical Review B **83**, 205101 (2011).

[134] H. Weng, C. Fang, Z. Fang, B. A. Bernevig, and X. Dai, "Weyl semimetal phase in noncentrosymmetric transition-metal monophosphides", Phys. Rev. X **5**, 011029 (2015).

[135] X. Huang, L. Zhao, Y. Long, P. Wang, D. Chen, Z. Yang, H. Liang, M. Xue, H. Weng, Z. Fang, X. Dai, and G. Chen, "Observation of the chiral-anomaly-induced negative magnetoresistance in 3D Weyl semimetal TaAs", Phys. Rev. X **5**, 031023 (2015).

[136] P. E. C. Ashby and J. P. Carbotte, "Magneto-optical conductivity of Weyl semimetals", Phys. Rev. B **87**, 245131 (2013).

[137] Z. Wang, Y. Zheng, Z. Shen, Y. Lu, H. Fang, F. Sheng, Y. Zhou, X. Yang, Y. Li, C. Feng, et al., "Helicity-protected ultrahigh mobility Weyl fermions in NbP", Physical Review B **93**, 121112 (2016).

[138] Z. Liu, L. Yang, Y. Sun, and et al., "Evolution of the fermi surface of weyl semimetals in the transition metal pnictide family", Nature Mater **15**, 27–31 (2016).

[139] D. Grassano, O. Pulci, A. Mosca Conte, G. Profeta, F. Mauri, and A. Continenza, "Validity of weyl fermion picture for transition metals monopnictides taas, tap, nbas, and nbp from ab initio studies", Scientific Reports **8**, 3534 (2018).

[140] M. Zhao, Z. Yan, X. Xie, Y. Yang, P. Leng, M. Ozerov, D. Yan, Y. Shi, J. Yang, F. Xiu, and S. Dong, "Unconventional Landau level transitions in Weyl semimetal NbP", Phys. Rev. Materials **6**, 054204 (2022).

[141] S. Polatkan, M. O. Goerbig, J. Wyzula, R. Kemmler, L. Z. Maulana, B. A. Piot, I. Crassee, A. Akrap, C. Shekhar, C. Felser, M. Dressel, A. V. Pronin, and M. Orlita, "Magneto-optics of a Weyl semimetal beyond the conical band approximation: case study of TaP", Phys. Rev. Lett. **124**, 176402 (2020).

[142] J. Wyzula, *Magneto-optics of Weyl and Dirac semimetals*, `https://theses.hal.science/tel-03885969`, (Accessed on 04/27/2023), 2022.